The Study of the Galactic structure by using Gravitational Microlensing

(重力マイクロレンズを用いた銀河構造の研究)

Takahiro Sumi

住 貴宏

The Study of the Galactic structure by using Gravitational Microlensing

Takahiro Sumi

A Doctoral dissertation
submitted to
Department of Physics, Nagoya University

February 2002

Abstract

The use of the Gravitational Microlensing effect has been established as a new tool to study Galactic structure by detecting the massive compact objects, e.g., "Assive Compact Halo Object (MACHO)" in the halo and also stars in the Galactic bulge and disk.

We have proposed two new methods in this paper to constrain the location of gravitational microlensing objects towards the Large Magellanic Cloud (LMC) using EAGLE (Extremely Amplified Gravitational LEnsing) events. This EAGLE event is the microlensing event in which the source star is fainter than the observational limiting magnitude. We have estimated the event rate of EAGLEs and found that is the same as or higher than that of ordinary microlensing events which have been found until now. We have also found that the fraction of transit EAGLE events, in which the proper motion of the lens can be estimated, is sufficiently large to detect. It turns out to be between $4 \sim 80\%$ depending on the lens location. Then we can discriminate the lens in the halo from that in the LMC itself. We show that it is possible to determine whether lens objects are located in the Galactic heavy thick disk or in the Galactic halo, with ground-based observation. The possibility to observe the parallax effect in EAGLE events is higher than normal events, in which the "reduced" transverse velocity of the lens could be obtained. Then we can distinguish whether the lens is in the halo or the thick disk.

To check whether EAGLE events could actually be detected or not, we analyzed the data of the Galactic Bulge (GB) taken by the MOA group. The analysis of the GB data is a good demonstration, because our observation towards the GB is aimed to detect such EAGLE type events in which the probability to find the Extrasolar Planets is very high.

We analyzed the MOA GB data during the 2000 season with use of the Difference Image Analysis (DIA) method and found 28 candidates of the microlensing event in the 12 GB fields corresponding to 16 deg^2 which contain 250 million stars down to $I \sim 23$. The DIA improved the quality of photometry, and enable us to detect more events with faint source stars such as EAGLE events especially in our high frequent observations. DIA also gives us a non-biased light curve, i.e. event parameters, even in the case that the source star is blended.

We have done a Monte Carlo simulation to estimate the microlensing event detection efficiencies of our observation and analysis. We made the I-band extinction map for our 14 GB fields in order to know the real baseline magnitude in each field. From these efficiencies and the timescales of observed events, an optical depth towards the GB was obtained for events with the timescales within $0.3 < t_E < 150$ days as $\tau_{0.3}^{150} = 2.62^{+0.72}_{-0.56} \times 10^{-6}$. With

consideration of the disk-disk component, an optical depth for the bulge component was estimated to be $\tau_{bulge} = 3.40^{+0.94}_{-0.73} \times 10^{-6}[0.77/(1-f_{\rm disk})]$, assuming a 23% stellar contribution from disk stars. These observed optical depths are consistent with the previous observations by MACHO and OGLE groups. These values are higher than those predicted by existing Galactic models. We presented the timescale distribution of the observed events, and found there are no significant small mass lenses such as brown dwarfs, in spite of our high detection efficiency for short timescale events down to $t_E \sim 0.3$ days.

Furthermore, we found that more than half of all detected events are EAGLE type events as expected and 50% of all events have high magnification ($A > 10$). So if a similar observation could be carried out towards the LMC, we can constrain the location of the lensing objects towards the LMC by estimating the lens proper motion or reduced velocity.

Contents

Chapter 1

Introduction

From ancient times, it has been carried out to observe the universe with visible light which comes from a star. Observation by photons of various wavelengths (e.g., electric wave, infrared rays, visible light, ultraviolet ray, x-ray, and gamma-ray) have been developed to the present time. And in recent years, a new method, which observes the mass directly by the gravitational lens even if the candidate for observation was not giving off light, has been established.

The space could be distorted by the gravity which exists in the surroundings of mass, the light which has traveled straight on there is refracted like in Figure 1.1. Since this mass is carrying out a role just like a lens, it is called a gravitational lens effect.

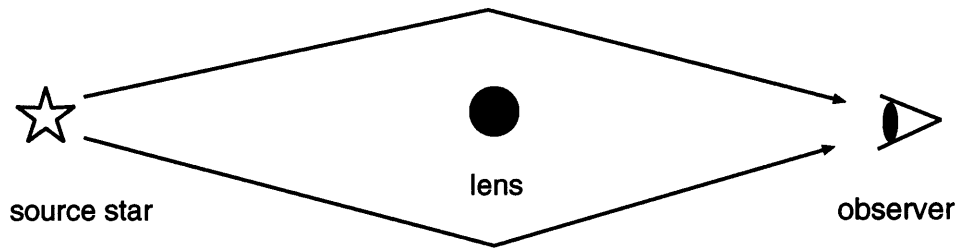

Figure 1.1: Schematic view of the Gravitational lensing.

1.1 History

At first, in 1704 Isaac Newton suggested this gravitational lens effect. A century later Soldner (1805) calculated that the classical deflection of a star's position due to deflection of light was $0.84''$ at the Sun's surface. In 1914 after the appearance of the Theory of General Relativity, Einstein proposed the value of deflection would be twice the Newtonian one, i.e., $1.75''(1+\gamma)/2$. In 1919, Dyson, Eddington, & Davidson (1920) succeeded in making the first observation of this effect during a solar eclipse, though the value was 20% different from Einstein's predicted value. Now it have been believed that this measurement didn't have the stated accuracy. However the hypothesis of Einstein has recently been

confirmed to be correct to an accuracy of 0.02% (Lebach, Shapiro & Ratner 1995). This became the good proof that the General Relativity is correct.

In 1924 Chwolson (1924) proposed that if the star is nearly aligned to another, double images of the background source star would be formed. And if stars are perfectly aligned, we could see a ring shaped image of the background star. This ring feature became well known as the "Einstein ring". After this, Einstein (1936) estimated that such a "Gravitational Lens" could highly magnify the light from the background star. He also noted that it is difficult to observe this phenomenon, because the separation were estimated far too small, as micro arcseconds. Thus this effect has been known as "gravitational microlensing". Next year, Zwicky (1937) pointed out that this feature could be seen if the lens was very massive, such as galaxies, which is referred to as "macrolensing" to compare with the above. But this phenomenon was not found for long time.

Thirty years later, Refsdal (1964) calculated the detailed formula of the magnification during the gravitational microlensing occur. At the same time, Liebes (1964) suggested that stars within globular clusters could act as a lens for each other, and stars within our Galaxy could lens stars within the Andromeda galaxy. However, the probability that the lens object would align very closely to the source stars is very small. The very large number of stars should be monitored to detect these events. So, at this time, it was thought that observing this phenomenon would be completely impractical.

At last, in 1979, Walsh, Carswell & Weyman (1979) discovered the first double quasars (Q00957+56/A, B) which separated with only a few arcseconds. These were thought to be the same quasar affected by the effect of gravitational lensing because they have the same color, redshift, and the variability of brightness confirmed by follow up observations. Until now more than 20 gravitationally lensed quasars have been found, which have multi-images (2, 3 or 4), arch shape or ring shape by optical and radio regions. The QSO 2237+0305 which has 4 images is well known as the "clover leaf" or "Einstein Cross". These are gravitational macrolensings in which distant quasars or galaxies are lensed by the intervening galaxy or the cluster of galaxies. These are useful to determine the cosmological constant by observing the time delay between each images. More discovery of such kind of events is expected by the massive sky survey observation such as Sloan Digital Sky Survey (SDSS).

Further 7 years later, Paczyński (1986) proposed that it is possible to detect the presence of the dark matter in the Galactic halo, if they are massive compact objects named as "MAssive Compact Halo Object (MACHO)", by monitoring the stars in the Magellanic Clouds for the signature of gravitational microlensing. He estimated the possibility that microlensing occur by MACHO as to be $\sim 10^{-6}$. So, for the detection of these events, a monitoring of millions stars is needed. The recent advances in CCD technology made it possible to make a large CCD camera to monitor millions of stars in the stellar dens fields.

At the beginning of 1990's, several groups (MACHO, EROS, OGLE and DUO) started the survey of microlensing events towards the stellar dense fields, such as the Large Magellanic Cloud (LMC) and Small Magellanic Cloud (SMC) and Galactic Bulge (GB), with 1 m class telescopes following the suggestion by Paczyński (1986). And in 1996, our MOA (Microlensing Observation in Astrophysics) group, which is the collaboration of Japan and

New Zealand, started the microlensing survey towards the LMC, SMC and GB in New Zealand.

In 1993, the first detection of the microlensing event was announced by MACHO collaboration which is the joint research of the United States and Australia (Alcock et al. 1993), and EROS collaboration which is from France (Aubourg et al. 1993). These events were discovered towards the LMC as the cataclysmic magnification of the brightness of the source star. Later in the same year, the first microlensing event along the line-of-sight of the GB was reported by the OGLE group which is a collaboration of Poland and the United States (Udalski et al. 1993). The event rate in the direction of the LMC is very small ($\sim 10^{-7}$), and that towards the GB is ten times higher ($\sim 10^{-6}$) because the number of stars along the line of sight towards the GB is much more.

Until now $\sim$ 20 events towards the Magellanic Clouds (Alcock et al. 1997b, 2000b; Afonso et al. 1998, 1999; Alcock et al. 1999a) have been reported. These results indicate that MACHOs are likely to be white dwarfs if these lenses are in the Galactic halo. However, the issues of where the lens objects are and what they are, are still unclear, because of a degeneracy of the lens parameters for each ordinary microlensing event. So new methods to constrain the lens location of the microlensing events are needed. On the other hand, to date, hundreds of events have been reported towards the GB (Udalski et al. 1994; Alcock et al. 1997a, 2000a). Now it became to be well understood that the observations of microlensing events are useful for studying the dynamics and kinematics of the Galaxy as these events are related to the masses and velocities of the sources and lens objects.

The use of gravitational microlensing is a new tool to detect extrasolar planets. Radio pulsar timing achieved the first detection of a planetary mass beyond our solar system in 1992 (Wolszczan & Frail 1992). The discovery of the first extra-solar planet surrounding a main-sequence star was announced in 1995, based on very precise radial velocity (Doppler) measurements (Mayor & Queloz 1995). A total of 34 such planets were known by the end of March 2000 (Perryman 2000), and their numbers are growing steadily. These planets detected from radial velocity measurements, of which 34 were known by the end of March 2000, have masses in the range $0.2 - 11 M_J$ (Jupiter mass), orbital periods in the range $3 - 1700$ days, semi-major axes in the range $0.04 - 2.8$ AU. By this method, one can observe only massive planets orbiting small radii around the near bright stars (< 50 pc). Planets significantly less massive than Jupiter cannot be detected with current radial velocity techniques. Based on present knowledge from the radial velocity surveys, about 5% of solar-type stars may harbor massive planets, and an even higher percentage may have planets of lower mass or with larger orbital radii.

In 1998 the MOA and GMAN groups detected an evidence for a low mass ($\sim M_\oplus$ (Earth-mass)) planet orbiting a star near the center of our Galaxy (Rhie et al. 2000).

Four groups are presently trying to detect planets using microlensing, MPS, PLANET, GMAN and MOA. Of these only MPS and PLANET are searching exclusively for planets. These group took frequent follow up observations of the microlensing event alerted by MACHO and OGLE collaborations. And MOA started to issue the alerts from 2000 (Bond et al. 2001). The MACHO group have shut down at the end of 1999, and OGLE is now

stopping the alerts because of upgrading the camera. So in 2001, the MOA group is acting an important role as the only group which issued the alerts of microlensing events to the world.

1.2 Thesis Outline

In this thesis, at first, we present the properties of the gravitational microlensing, the status of the experiments and problems in Chapter 2. The main problem is that we couldn't know where the lens objects of microlensing events towards the LMC are.

Then, we present two new methods to constrain the location of the lens object of microlensing events towards the LMC by using the finite source effect (section 3.1) and the parallax effect (section 3.2) in EAGLE events in Chapter 3. This EAGLE (Extremely Amplified Gravitational LEnsing) event is the microlensing event in which the source star is fainter than the observational limiting magnitude.

Next, the results of the analysis of the data towards the GB taken by MOA in the 2000 season with DIA are presented in the following Chapters. This analysis is aimed to check how efficiently we can detect the EAGLE type high magnification events, and to estimate the optical depth towards the GB, which give us the information of the structure of the Galactic Bulge. We mainly deal with the data reduction, the event detection, the simulation to estimate the efficiency, and the optical depth estimation with data along the line of sight to the GB. In Chapter 4 we describe the details of the observation site, the wide field telescope and camera system of MOA which is used to take the data used throughout this thesis. And our observation strategy is also given. Chapter 5 is devoted to the analysis method which has recently been adopted from 2000, the data preparation, the detail of the DIA, the object detection, the photometry, the noise estimation and the calibration of the flux. The development of using the DIA which overcomes a lot of problems in photometry in the stellar dense field are shown. In Chapter 6 we describe the microlensing event selection process from the database and show the light curves of detected events. In Chapter 7 we made the I band extinction map of our GB fields due to the dust. This is very useful to estimate the extinction free magnitude in the simulation. In Chapter 8 we present about the simulation to estimate the detection efficiency of our system. And the resultant detection efficiencies are shown. By using the detection efficiency and the detected events, we estimated the microlensing optical depth towards the GB. Discussions about our results and conclusions are given in Chapter 9.

Chapter 2

Gravitational Microlensing

2.1 Theory

Here we describe the theory of the gravitational lensing and the gravitational microlensing. The gravitational microlensing effect is one of the gravitational lens effects. The gravitational lens effect is well known as the phenomenon that the image of a quasar or a galaxy would be divided into two or more images of arches, or a circle (Walsh, Carswell & Weyman 1979) due to the gravity of another intervening galaxy.

In the case that the lens is on a terrestrial scale, the separation of images would be micro arcseconds. So we couldn't resolve these images, and we can only observe the magnification of the source brightness. There are many types of variable stars in our observed database. To distinguish the rare microlensing events from these variable stars in our database, the theoretical microlensing curve would be very useful. In this section we present the characteristics of microlensing event light curves which make their identification possible.

2.1.1 Refraction of light

Now, we consider the trajectory of a light ray in a spherically symmetric gravitational field produced by the central heavy object. The appropriate solution of this in the general relativity is the Schwarzschild solution, and the light ray travels on a null geodesic.

Then we considered the null geodesic of the Schwarzschild solution first. The simplest approach is to employ the variational method. In the Schwarzschild solution, the quantity $2K$ for the null geodesic is defined as

$$2K = \left(1 - \frac{2M}{r}\right)\dot{t}^2 - \left(1 - \frac{2M}{r}\right)^{-1}\dot{r}^2 - r^2\dot{\theta}^2 - r^2\sin^2\theta\dot{\phi}^2 = 0, \tag{2.1}$$

where "$\cdot$" indicates the differentiation about the affine parameter s, M indicates the mass of the lens, r represents the distance between mass and light. The Euler-Lagrange equation about this is a formula as

$$\frac{\partial K}{\partial x^a} - \frac{d}{ds}\left(\frac{\partial K}{\partial \dot{x}^a}\right) = 0, \tag{2.2}$$

where x^a is each parameter of position r, θ and ϕ. And now θ is angle around the line of sight to the lens object from the observer. So equation about θ is not considered because we are considering the symmetric field. Solving this equation about ϕ with the approximation that $\Delta\phi$ is small, one can obtain the deflection δ of a light ray passing a mass M, at a distance r_0, which is given by

$$\delta = \frac{4GM}{c^2 r_0}, \quad r_0 >> R_s, \tag{2.3}$$

where R_s is the Schwarzschild radius ($\sim$ 3 km for the $M_\odot$) given by

$$R_s = \frac{2GM}{c^2}, \tag{2.4}$$

and c is the speed of light, and G is the gravitational constant.

2.1.2 Microlensing light curve

Here we present the theoretical light curve of the microlensing event.

First we consider a simple case that the lens object is a point mass M, and the source star can also be regarded as a point source. This seems to be a good approximation for stellar size objects at *kpc* distances. In this case, the Einstein radius in which the gravitational field affects the light effectively is in the order of $\sim$ *AU* at the deflection plane. If the line of sight separation between lens and source is small relative to the source size, the point source approximation is no more valid and the finite source size effect must be taken into account (see section 3.1). In such an event with the finite source size effect there are additional parameters, which help us to constrain the character of the lens object.

We show the schematic view of the deflection of the light ray traveling from the source S by the lens object M to the observer O in Figure 2.1. Here D_d and D_s denote the distance of lens object (deflector) and source D_s from the observer respectively. $\alpha = r/(xD_s)$ is the angular separation of the line of sight to the lens object and the apparent image, $\beta = r_0/(xD_s)$ is the angular separation of the line of sight to the lens object and the real source position, where r_0, r are the distance to the real and apparent source position from the lens object at the deflection plane, and $x = D_d/D_s$ denotes the normalized distance to the lens object. From the geometry, the relation of the angles is given by

$$D_s\beta + D_s(1-x)\delta = D_s\alpha. \tag{2.5}$$

This equation leads to the following lens equation by substituting the expression of α, β and δ.

$$r^2 - r_0 r - R_E^2 = 0, \tag{2.6}$$

where R_E is so-called the "Einstein radius" expressed by

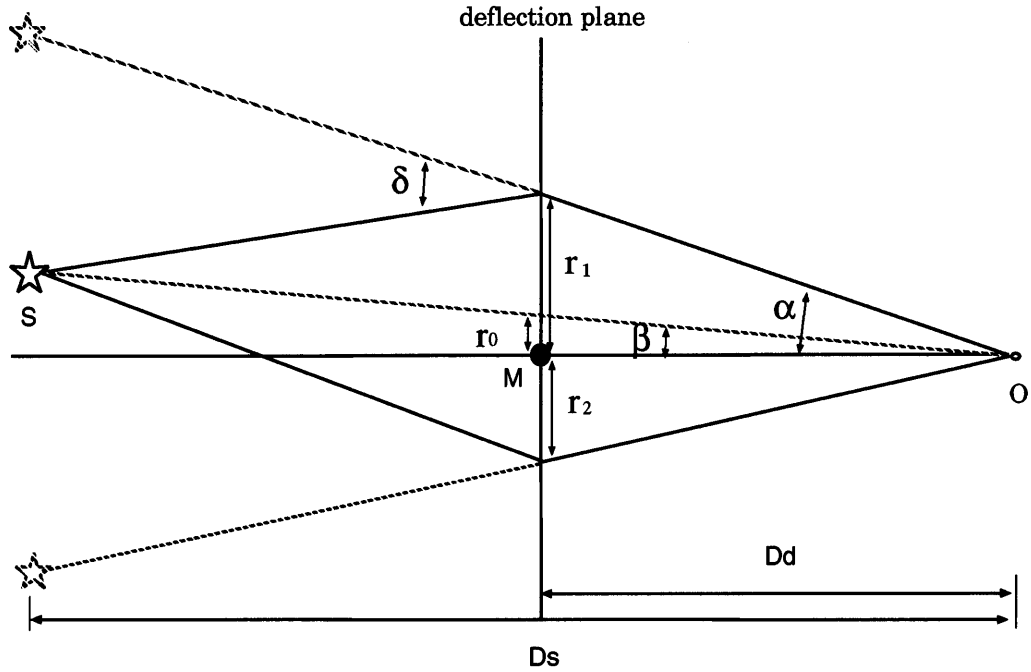

Figure 2.1: Gravitational deflection of a light ray from a source by a lens M as seen by an observer O. D_d and D_s are the distances to the lens object (deflector) and the source S from the observer O respectively. α is the angular separation of the line of sight to the lens object and the apparent image, β is the angular separation of the line of sight to the lens object and the real source position.

$$R_{\rm E}(M,x) = \sqrt{\frac{4GM}{c^2}D_{\rm S}x(1-x)} \tag{2.7}$$

$$\simeq 10{\rm AU}\left(\frac{M}{1M_\odot}\right)^{\frac{1}{2}}\left(\frac{D_{\rm S}}{50{\rm kpc}}\right)^{\frac{1}{2}}\left(\frac{x(1-x)}{1/4}\right)^{\frac{1}{2}}. \tag{2.8}$$

This Einstein radius is the radius of the circle image formed in the case that the lens and the source are perfectly aligned. The solution of this lens equation (equation (2.6)) $r_{1,2}$ is given by

$$r_{1,2} = \frac{r_0 \pm \sqrt{r_0^2 + 4R_E^2}}{2}. \tag{2.9}$$

These are the positions of the resultant two separate images of the source star on either side of the lens. These images are separated by the order of micro-arcseconds (μas) when the lens is of stellar size. So this is called as "microlensing".

The deflection of the light changes the cross section of the light bundle. In this case the solid angle of the bundle is increased, but the surface brightness remains constant from the Liouvilles theorem. The brightness of these images is determined by the size of a geometric

area of the image, i.e., the product of the surface brightness and the solid angle of the image. So the amplification μ of an image is estimated by the ratio of the solid angle of the real source which is not deflected, to that of the deflected images. This is given by the determinant of the Jacobian matrix of the lens equation (equation (2.6)) as follows

$$\mu = \left| det \frac{\partial r_0}{\partial r} \right|^{-1} = \left| \frac{r dr}{r_0 dr_0} \right|. \tag{2.10}$$

And this for each image is given by

$$\mu_{1,2} = \left| \frac{r_{1,2} dr_{1,2}}{r_0 dr_0} \right| = \left| \frac{r_{1,2}^4}{r_{1,2}^4 - R_E^4} \right| = \frac{1}{4} \left(\frac{u}{\sqrt{u+4}} + \frac{\sqrt{u+4}}{u} \pm 2 \right). \tag{2.11}$$

In the microlensing, we can only observe the combination of these amplifications given by

$$A = \mu_1 + \mu_2 = \frac{u^2 + 2}{u\sqrt{u^2+4}} \tag{2.12}$$

where $u = r_0/R_E$ is the impact parameter normalized by R_E. Usually the source and lens are moving, so this u depends on time as follows

$$u(t) = \sqrt{u_{min}^2 + \left(\frac{t - t_0}{t_E} \right)^2}, \tag{2.13}$$

$$t_E = \frac{R_E}{v_t}, \tag{2.14}$$

where u_{min} is the minimum impact parameter, i.e., the closest approach of the lens to the line of sight to the source at the time t_0. t_E is the Einstein radius crossing time named as "event time scale", and v_t is the relative transverse velocity of the lens-source system assuming the relative inertial motion. (Note this event timescale t_E is proportional to $M^{1/2}$). Therefore, by substituting $u(t)$ into equation (2.12), we can get the characteristic amplification as a function of time $A(t) = A(u(t))$. We show this amplification curve as a function of time t in Figure 2.2 with the various minimum impact parameters $u_{min} = 0.1, 0.2, ...1.0$ from top down. Usually the microlensing event is defined as an event with $u_{min} \leq 1$ which corresponds to $A \geq 1.34$.

Actually the value we can observe is the the microlensed flux of source star as follow

$$F(t) = F_0 A(t) + F_b, \tag{2.15}$$

where F_0 is the unamplified source flux, and F_b is the total background flux.

These theoretical amplification curves are useful to distinguish microlensing events from a number of various variable stars in the data base. By fitting the data points to the theoretical microlensing curve (equation (2.12)), one can obtain the values of the microlensing parameters such as t_0, t_E, u_{min} and F_0. However the lens mass M, the distance D_d and the

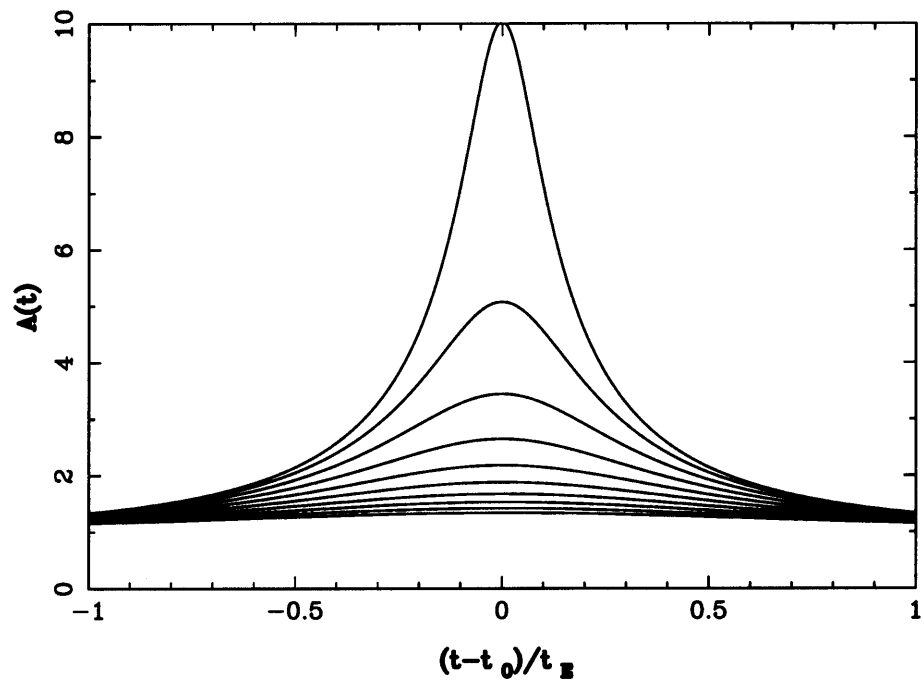

Figure 2.2: Theoretical amplification curve of microlensing as a function of time t normalized by the event timescale t_E. The lines are for the various minimum impact parameters $u_{min} = 0.1, 0.2, ...1.0$ from top down.

transverse velocity v_t are degenerate in t_E, and hence we couldn't get these values directly in the light curve fitting.

As shown in these equations and the figure there are some unique characteristics in the microlensing events relative to known variable stars as follows

- The microlensing event is achromatic, because amplitude in equation (2.12) is independent on the wavelength of the light.
- As shown in Figure 2.2 the microlensing light curve is symmetric with time.
- And a microlensing event does not repeat. The probability of the microlensing is very small ($\sim 10^{-7}$), so it should not repeat to the same source stars within millions of years. Usually most variable stars change their brightness repeatedly.

These are general properties of normal microlensing. There are some exceptions for rare exotic microlensing events such as a binary event, a finite source event and a parallax event. In these exotic events we can sometimes obtain not only t_E but also other information about the lens.

2.1.3 Microlensing optical depth

The microlensing optical depth estimated by observation is a useful quantity for probing Galactic structure. The optical depth of microlensing is defined as the probability that

any given source star is microlensed with an impact parameter $u \leq 1$ at any given time. This is equal to the fraction of the surface covered by the Einstein rings for a given line of sight. So, the optical depth τ could be estimated by summing the the area where the Einstein ring covers πR_E^2 for each lens along the line of sight to the the source. This is also the same as the number of the compact objects in the "microlensing tube" which is the region within the Einstein radius $R_E(x, M)$ from the line of sight towards the source star as shown in Figure 2.3.

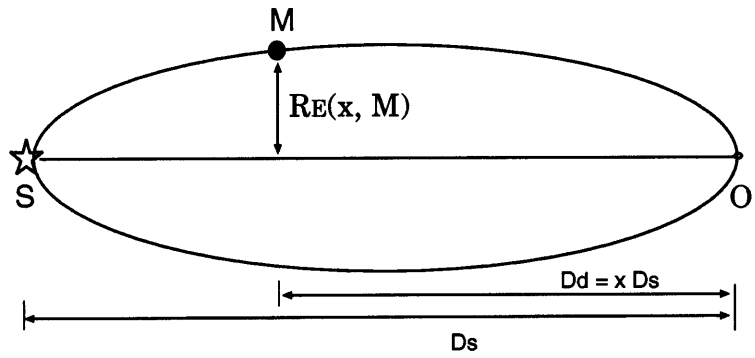

Figure 2.3: The microlensing tube which is the region within the Einstein radius $R_E(x, M)$ from the line of sight towards the source star. The optical depth is same as the number of compact objects in this tube.

So, the optical depth τ is given by integrating the number density $n(x)$ of lens objects in this tube as follow

$$\tau = \int_0^1 n(x, M)\pi R_E^2(x, M)dx. \tag{2.16}$$

By substituting equation (2.7), this is reformed as

$$\tau = \int_0^1 \frac{4\pi G D_s x(1-x)}{c^2}\rho(x)dx, \tag{2.17}$$

where $\rho(x)$ is the mass density of lenses at the location x. Thus the the optical depth τ is independent on the lens mass M, and only depends on the mass density distribution of lenses $\rho(x)$. In this way the optical depth is a measure of the total mass of the compact object whose event timescale is within the sensitive range of the experiment along the line of sight. So the optical depth is a very useful quantity for comparing with predictions for Galactic density models without any detailed knowledge or assumption about the mass function and the velocity distribution of the lens objects.

However, if a Galactic model is consistent with the microlensing results, both the optical depth and the timescale distribution of observed events should be consistent with each other. These timescale distributions provide us an opportunity to check of the velocity distribution of a model. If we could get a sufficient number of events, we can also estimate

the optical depth as a function of the location. This would provide us with good information in order to constrain the galactic model.

In practice, only t_E is the observable value about the lens object, in which the mass M, the distance x, and the velocity v_t are degenerate. The experimental optical depth could be estimated with this t_E. From the definition, the observed optical depth is the ratio of the sum of the event timescale to the sum of the product of the number of the observed stars N_s and observation time T_o as follow

$$\tau_{obs} = \frac{\pi}{N_s T_o} \sum_i \frac{t_{E,i}}{\varepsilon(t_{E,i})}, \tag{2.18}$$

where $\varepsilon(t_{E,i})$ represents the event detection efficiency of our system as a function of the event timescale $t_{E,i}$ of ith event. The sum is over each event detected with respect to its efficiency. Therefore, determining the detection efficiency is very important to estimate the optical depth, though this is complex since all data reduction and detection processes should be simulated. We have simulated it for our observation and analysis in order to estimate the optical depth towards the GB in Chapter 8.

2.2 MACHO

The main aim of the microlensing search towards the Magellanic Clouds is to find the Massive compact halo objects (MACHO) in the halo of the Galaxy as suggested by Paczyński (1986). MACHO is a candidate of the baryonic dark matter lying in the galactic halo. MACHO, which is the one of the main targets for the observation of our MOA group, is explained here.

2.2.1 Dark matter

The existence of the substance which dose not emit light, the so-called dark matter, is known in various classes of the universe. The mass densities which were analyzed by perpendicular movement of the stars around the solar system (Oort limit) is about 1.5 times larger than the total observed mass of stars and interstellar gases (Oort 1960).

The relation between the distance from the center of the Galaxy and the rotation speed (rotation curve) has been observed in various spiral galaxies including our Galaxy, which indicate the mass of these galaxies must have $10 \sim 20$ times bigger mass than the total mass observed emitting light from these galaxies (Rubin et al. 1980, 1982, 1985). This fact is considered as a strong proof of the existence of dark matter in the halo of galaxies. Furthermore, the observational distribution of the movement speed of galaxies in a cluster of galaxies shows that each galaxy must be bound to a mass dozens of times bigger than the total mass of all the galaxies. And such large masses between galaxies are observed through X-rays.

It has been considered that there are two components in the dark matter, a baryon-dark matter, and a non-baryon-dark matter. A non-baryon-dark matter is a theoretical elemen-

tary particle candidate, which has the mass, called WIMPs (Weakly Interacting Massive Particles). It is the elementary particle which cannot be observed since the interaction is very weak. As this candidate, a neutrino with heavy mass, an axion, or a SUSY particle etc. can be considered. It is thought that a baryon-dark matter is an astronomical candidate, which has the massive body but emits little radiation. As this candidate, a brown dwarf, red dwarf, a white dwarf, a neutron star, and a black hole etc. have been considered.

Since the contribution of a baryon to the density parameter is restricted to $0.01 < \Omega_b < 0.06$, from the theory of the nucleosynthesis in early stages of the universe, it is impossible to explain that the dark matter of the whole universe consist only of the baryon-dark matter. However, since this restriction is not applicable on the level of the galaxies, it is fully possible to think that these compact objects called as MACHOs are the dark matter which accompanies the galaxies. And in fact it is important to know the fraction of the baryon-dark matter in the Galaxy.

2.2.2 MACHO

As described in the previous section, MACHO is one of the dark matter candidates which accompany the Galaxy. These are considered to be brown dwarfs in which nuclear fusion reactions do not occur due to their low mass ($M < 0.08 M_\odot$), red dwarfs in which nuclear fusion reactions are not so much, and stellar remnants such as white dwarfs, neutron stars, and black holes. Primordial black holes made in the early stages of the universe are also candidates (Ioka, Tanaka & Nakamura 2000). These are considered to exist in the halo of the Galaxy as in Figure 2.4.

The schematic view of the Galaxy shown in Figure 2.4, clearly presents the anticipation that a great portion of the mass exists in the bulge which shines very brightly. The evidence that dark matter must exist in the Galactic halo is coming from a relation of $M_L < M_{total}$, where M_L is the mass estimated from the luminosity of the stars and gases, and M_{total} is the mass estimated from dynamical motion of those objects. In this case that $M_{total} = M_L$ the expected rotation speed should become so small at larger galactic radii according to Keplerian movement. However this is far from the observed rotation curves (Rubin et al. 1980, 1982, 1985), which are almost flat to the outer part of the galaxies.

M_{total} can be found by the dynamical motion of objects as follows. In the case of a spiral galaxy, the centrifugal force by rotation v of each star (mass m) and the gravity by mass $M(r)$ contained inside the radius r should balance. This is explained by the following formulas, assuming the mass distribution of the galaxy is symmetric for simplicity.

$$\begin{aligned} m\frac{v^2}{r} &= \frac{GmM(r)}{r^2}, \\ M(r) &= \frac{rv^2}{G}, \end{aligned} \tag{2.19}$$

where $M(r)$ is the total mass contained inside the radius r.

The rotation curve of the Milky Way Galaxy also seems to be flat (Fich 1989), although outside of the solar system ($R_0 = 8.5$ kpc), it has very large uncertainty in the case of our

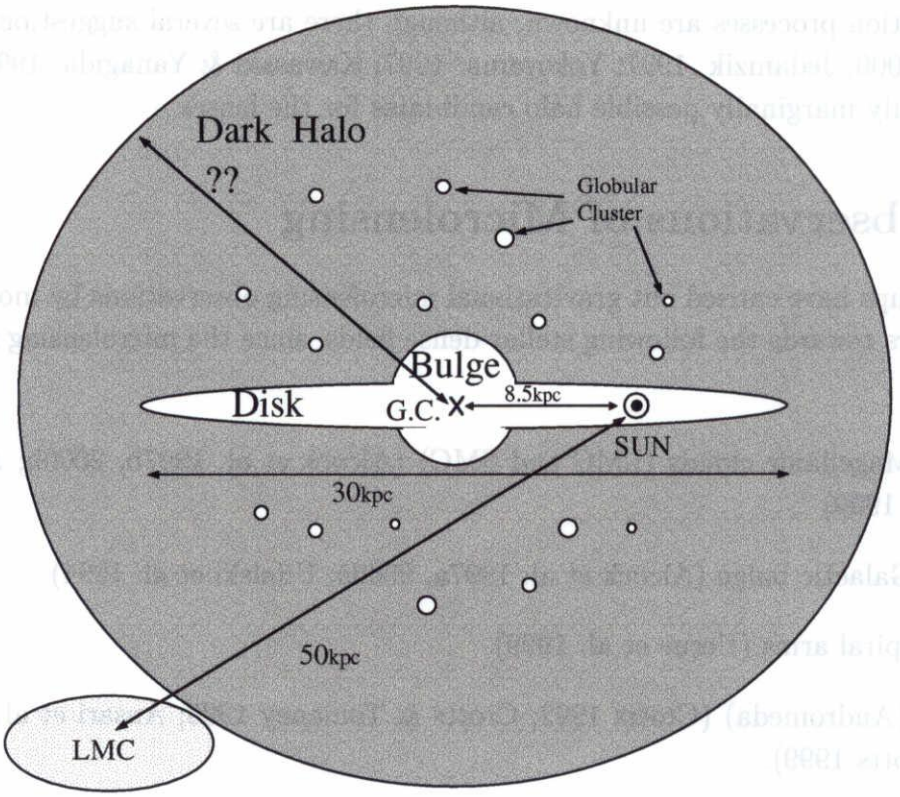

Figure 2.4: Schematic view of the Galaxy surrounded by dark halo. Most of stars can be seen in the central part (bulge) and disk.

Galaxy. From comparison with other galaxies, it is presumed that the rotation speed is almost flat (However, recently, Honma & Sofue (1996) asserted that the rotation curve of the Galaxy is declining beyond $> 2R_0$ according to Keplerian movement ($v \propto r^{-\frac{1}{2}}$)). In the case that the rotation curve is flat, i.e. $v = const.$, the mass distribution of the Galactic halo is given by

$$M(r) \propto r. \tag{2.20}$$

From this, the total mass M_{total} must increase in proportion to the radius r. This difference $M_{total} - M_L$ represents the existence of the dark matter, and some fraction of this is considered to exist as MACHOs. As shown in Figure 2.4 if the MACHOs exist in the galactic halo, we can detect these as the lens objects of the microlensing events towards the LMC and SMC.

About the nature of the MACHO, it is still not clear. For white dwarf MACHOs, the consistency with the Galactic chemical evolution is the most serious problem (Charlot & Silk 1995; Gibson & Mould 1997), although it was reported recently that old white dwarf candidates were discovered in a proper motion survey with the *Hubble Space Telescope (HST)* (Ibata et al. 2000). Old brown dwarfs and primordial black holes do not suffer from this problem (Fujita et al. 1998), so they are attractive from this point of view, but

clear formation processes are unknown, although there are several suggestions (Uehara & Inutsuka 2000; Jedamzik 1997; Yokoyama 1997; Kawasaki & Yanagida 1999). In short, there are only marginally possible halo candidates for the lenses.

2.3 Observations of Microlensing

Several groups have carried out gravitational microlensing observations by monitoring millions of stars towards the following stellar dense fields, since the microlensing event is very rare.

- The Magellanic clouds (LMC and SMC) (Alcock et al. 1997b, 2000b; Afonso et al. 1998, 1999)
- The Galactic bulge (Alcock et al. 1997a, 2000a; Udalski et al. 1994)
- The spiral arms (Uerue et al. 1999)
- M31 (Andromeda) (Crotts 1992; Crotts & Tomaney 1996; Ansari et al. 1997; Gyuk & Crotts 1999).

2.3.1 Towards the Magellanic Clouds

The aim of the microlensing search towards the Magellanic Clouds is to find the Massive compact halo objects (MACHO) in the halo of the Galaxy as described in the section 2.2.2.

Several groups have carried out gravitational microlensing observations towards the Large Magellanic Cloud (LMC) and the Small Magellanic Cloud (SMC) in order to search for MAssive Compact Halo Objects (MACHOs) in the Galactic halo. Until now, 13-17 candidates have been found towards the LMC (Alcock et al. 2000b), and 2 candidates have been found towards the SMC (Afonso et al. 1998, 1999; Albrow et al. 1999; Alcock et al. 1999a). The estimated mass of a typical lens object depends somewhat on the adopted Galactic kinematic model. The possible range is about $0.01 - 1M_{\odot}$ (Alcock et al. 1997b, 2000b; Honma & Kan-ya 1998).

According to the recent results, the observed optical depth form the events with $1 < t_E < 200$ days towards the LMC is $\tau_1^{200} = 1.2^{+0.4}_{-0.3} \times 10^{-7}$, the most likely MACHO mass is between $0.15M_{\odot}$ and $0.9M_{\odot}$ depending on the halo model, and the fraction of the total mass of MACHO to that of the dark Galactic halo is $20^{+30}_{-20}\%$ in 95% confidence level. And the total mass of MACHO out to 50 kpc is $9^{+4}_{-3} \times 10^{10}M_{\odot}$ independent of the halo model (Alcock et al. 2000b). We have learned that there are substantial lens objects along the line of sight towards the LMC, more than one would expect from lensing by the known populations of stars ($\tau \sim 0.5 \times 10^{-7}$).

However, the issues where the lens objects are and what they are, are still unclear, because of a degeneracy that occurs in ordinary microlensing events. The light curve of a microlensing event is determined by the amplification factor A, which depends only on the

relative lens-source displacement u projected on to the lens plane in units of the Einstein radius $R_{\rm E}$ (see equations (2.7), (2.12) and (2.14)) (Paczyński 1986). The light curve of microlensing is given by $A(u(t))$ in equation (2.12). From a light curve one can determine the value of u_{min}, t_0 and t_E. Unfortunately, however, one cannot uniquely determine the value of M, x or $v_{\rm t}$ from these quantities, only the ratio $t_E = R_E(M,x)/v_{\rm t}$ is determined. This three-fold degeneracy is the essential difficulty in determining the nature of the lens objects.

From the statistics of the events the MACHO collaboration reported that the microlensing optical depth $\tau_1^{200} = 1.2^{+0.4}_{-0.3} \times 10^{-7}$ as mentioned above. This implies the column density of lenses along the line of sight to the LMC is roughly $15 M_\odot {\rm pc}^{-2}$ if the lenses are in the Galactic halo (Nakamura, Kan-ya & Nishi 1996). The nature of such lens objects is, however, still unclear because there are only marginally possible candidates, viz. old white dwarfs (e.g. Alcock et al. 1997b, 2000b; Hansen 1998), old brown dwarfs (e.g. Honma & Kan-ya 1998) and primordial black holes (e.g. Ioka, Tanaka & Nakamura 2000). There are, however, still no coherent pictures for these candidates.

Possibilities for non-halo lensing objects have also been discussed. For example, dark objects in the LMC itself (e.g., Aubourg et al. 1999; Gyuk, Dalal & Griest 2000). And one cannot rule out the possibilities that the microlensing events are not caused by MACHOs in the halo of the Galaxy but by unknown populations lying between the Galaxy and the Clouds (e.g., Zaritsky & Lin 1997; Zhao 1998). Evans et al. (1998) suggest that the lenses are disk stars in the Milky Way's warped flared disk. There is also a possibility that the lenses are dark objects in the Galactic thick disk. While the microlensing optical depth τ by known populations of stars in the Galactic thin disk and thick disk is in the order of 10^{-9} (e.g. Alcock et al. 2000b), a maximal heavy thick disk, which may be surrounded by an extended dark halo composed of particles, is also a possible Galactic component for the reservoir of lenses (Gates et al. 1996; Gates, et al. 1998). Such a thick disk can have $\tau \simeq 7 \times 10^{-8}$ (Gould 1994b; Gould, Miralda-Escude & Bahcall 1994), so the summed optical depth including the contribution from the Galactic thin disk ($\sim 2 \times 10^{-8}$) and the LMC itself ($\sim 1 \times 10^{-8}$, Sahu 1994) can be close to the observed value.

The discussion on the nature of the lenses is now in a complicated situation called ("the MACHO Mystery"). New kinds of observational tests which can resolve the three-fold degeneracy of M, $D_{\rm d}$ and v_t are needed.

It has already been noted that the three-fold degeneracy can be resolved in some kinds of exotic microlensing events. For example, binary events in which the lens distance and the transverse velocity are constrained (Albrow et al. 1999; Alcock et al. 1999a; Honma 1999; Afonso et al. 2000). Another example is the finite source transit event in which one can obtain the proper motion of the lens $\mu = v_t/D_d$ (Gould 1992, 1994a; Nemiroff & Wickramasinghe 1994; Witt & Mao 1994; Peng 1997). Sumi & Honma (2000) pointed out that an extensive search for this type of event would make it possible to discriminate between the lenses in the Galactic halo and in the LMC (see section 3.1).

A third example is an event with a parallax effect. The spatial shift of an observer due to the Earth's motion around the Sun during the event leads to an asymmetry of the light

curve (e.g. Miyamoto & Yoshii 1995; Alcock et al. 1995; Bond et al. 2001; Soszyński et al. 2001). However, such events are rare. This parallax effect generally requires $t_E > 100 \sim 200$ days, while $t_E \sim 40$ days for typical events. By observing an event from both a solar-orbit satellite and the Earth, we could utilize the parallax effect in almost every event, while it is difficult from two distant observatories on the Earth (Refsdal 1966; Gould 1992, 1994b, 1995b; Holz & Wald 1996). In this case, we could measure the relative difference of the peak amplifications and the time at the peak amplifications between both. Then we could determine, the "reduced transverse velocity" $\tilde{v} = v_t/(1-x)$. If both the finite source size effect and the parallax effect could be measured at the same time, three-fold degeneracy can be resolved completely.

Gould (1997) showed that towards the Galactic bulge the finite source size effect and the parallax effect could be measured in EME's (Extreme Microlensing Events, $A > 200$) from the ground. In this case the microlensing degeneracy is completely broken and we are able to obtain the mass, the distance and the transverse-speed of the lensing object separately. However he just made a crude estimation about the observation of EME towards the LMC, and concluded that it is not feasible. After that, Nakamura & Nishi (1998) showed that it is feasible to detect EAGLE (Extremely Amplified Gravitational LEnsing) events towards the LMC after more careful estimation than the former one. EAGLE is similar to the so-called "Pixel lensing" events (Gould 1996) but more simply defined as the events in which the source star is dimmer than the observational limiting magnitude (ex. $V_{obs} = 21 \sim 22$), but is not concerned with whether the source star is resolved or not. Some of the EAGLEs would be EME's. So, we refer to the term EAGLE in this paper. However Nakamura & Nishi (1998) did not consider the possibility to detect the finite source effect and the parallax effect in EAGLE events. This kind of event could be efficiently detected with the new CCD photometry method DIA (see section 2.4 and Chapter 5).

In section 3.1 we have made the estimation of the rate of finite source effect measurable EAGLE events towards the LMC. And it was found that it is feasible to distinguish whether the lens is in the halo or the LMC by using DIA (Sumi & Honma 2000). And in section 3.2, we have made a more accurate estimation of the rate of parallax-measurable EAGLE events towards the LMC from two ground-based observational sites than former studies did. We have found that this is useful to distinguish whether the lensing objects are in the halo or the thick disk with DIA. Combining these result with section 3.1 (Sumi & Honma 2000), we are able to discriminate where the location of lenses are, in the LMC, in the halo, or in the thick disk.

To test that such EAGLE events could actually be detected, it is useful to analyze our data of frequent observations towards the Galactic bulge by using DIA. As a result we found that such EAGLE events could actually be detected in our observation and analysis in this thesis.

2.3.2 Towards the Galactic Bulge

At the beginning of 1990's several groups started microlensing event survey experiments towards the Magellanic Clouds following the suggestion of Paczyński (1986). However it was thought that this task is certainly difficult, as there was no guarantee that the dark halo is made of MACHOs rather than WIMPs. Paczyński (1991) noted, to have any confidence that a negative result is correct, one should have the confidence that the experiment (hardware and software) would in fact be able to identify the rare microlensing events.

And then he and Griest et al. (1991) proposed a gravitational microlensing survey towards the Galactic Bulge (GB), as seen in Baade's window, would provide a promising target to do this test, where the probability of the microlensing, i.e. the optical depth τ, towards the GB is very high ($4 \sim 8 \times 10^{-7}$) in comparison with the LMC, and the number of stars is much more than that of the LMC.

They also proposed that this test would also be sensitive to the presence of the Galactic disk brown dwarfs and the very low mass end of the stellar mass function, which is difficult to measure directly. If they make a large contribution to the disk mass density, these would be detected as short timescale events, because the duration of the microlensing event is related to the mass of the lensing object. And this observation can also test for controversial "disk dark matter" (Bahcall 1986; Kuijken & Gilmore 1989) in addition to a possible signal from halo dark matter, where the optical depth in the direction of Baade's window due to halo objects of any kind is only $\sim 0.13 \times 10^{-6}$ (Griest et al. 1991). These contribution may potentially be separated by observations of fields at different Galactic latitude and longitude, and also by comparing the mean timescale of events.

Now it became to be well understood that the observations of microlensing events are useful for studying the dynamics and kinematics of the Galaxy as these events are related to the masses and velocities of the sources and lens objects. Unlike most types of observation, the presence of lensing objects can be detected independently of their luminosity. Microlensing is sensitive to the mass distribution rather than the light, and this makes microlensing a powerful way of investigating the the mass density within our Galaxy.

Surveying the entire Galaxy is needed to determine the global parameters of the Galaxy. However, it is difficult because the microlensing phenomenon is very rare. Therefore, the microlensing searches have been focussed on events towards the GB and spiral arms in addition to the Magellanic Clouds. By good fortune, the GB is located $\sim 12^{\rm h}$ away from the LMC in right ascension, and hence it is well placed for observing when the LMC is at low altitude. Then MACHO, EROS and OGLE groups started to observe the GB once a day. Meanwhile MOA started the observation towards the GB several times a day from 1999.

The Galaxy is thought to be a SAB(rs)bc or SAB(r)bc type spiral galaxy with four spiral arms (Vallee 1995; Fux 1997). But the mass distribution of various components of our Galaxy (Bulge, Spheroid, Disk and Halo) is not well known. The determination of the structure such as mass, scale length, scale hight and rotation curve are still complicated by

the dust lying within the Galactic disk. This dust causes the degree of extinction to vary along different lines of sight through the Galaxy and heavily obscures much of the Galaxy at optical wavelengths.

Microlensing allow us to probe the distribution for compact objects in the range $M \sim 10^{-6}M_{\odot}$ to $M \sim 10^{2}M_{\odot}$. From the distribution of the timescale of these events, we can obtain information about the mass function of the Galaxy from very luminous stars ($10^{2}M_{\odot}$) to very faint ones below the hydrogen burning limit ($< 0.08M_{\odot}$) without being metallicity dependent. From these event rates, we can also get an information about the mass density distribution of these objects.

To constrain these distributions sufficiently, a large number of events is required (Han & Gould 1995b;Mao & Paczyński 1996). And a small number of exotic events ($< 10\%$), in which the masses, velocities, and locations of the lensing objects can be determined, are also very useful in differentiating between various possibilities of the assumptions. The microlensing observations towards the GB are also useful to know what is the mass and the inclination of the bar.

Until now, hundreds of microlensing events have been detected towards the GB by OGLE (Udalski et al. 1994) and MACHO collaborations (Alcock et al. 1997a, 2000a). And they estimated the microlensing optical depth towards the Galactic bulge to be $3.3 \pm 1.2 \times 10^{-6}$ from 9 events by DoPHOT analysis, $3.9^{+1.8}_{-1.2} \times 10^{-6}$ from 13 events in a clump giant subsample from DoPHOT and $3.23^{-0.50}_{+0.52} \times 10^{-6}$ from 99 events from DIA respectively. These values were greater than twice that expected from models based on the observed stellar density and gas kinematics, which is somewhere around $0.5 \sim 1.0 \times 10^{-6}$ (Paczyński 1991; Griest et al. 1991; Kiraga & Paczyński 1994). This suggested that the standard models of the Galaxy needed to be revised. In fact, one possible explanation of the large optical depth towards the bulge is that the mass of the Galactic disk and bulge in ordinary stars is large enough to account for almost all of the mass interior to the Sun. If it is true, this would imply that the Galactic halo must have a large core radius or perhaps a rather small total mass. Thus, microlensing towards the GB seems likely to reveal information about the properties of the Galaxy that are important for determining the properties of the Galactic dark halo.

From these results, it has also been suggested that this could be explained by the presence of a bar oriented along our line of sight to the GB (Paczyński et al. 1994; Zhao, Spergel & Rich 1995). The density profile of the proposed bar as a function of distance D from the Sun is given by (Alcock et al. 2000a)

$$\rho_b(w) = \frac{M}{20.65abc} exp\left(-\frac{w^2}{2}\right), \tag{2.21}$$

where w is defined as

$$w^4 = \left[\frac{x'^2}{a} + \frac{y'^2}{b}\right]^2 + \frac{z^4}{c}. \tag{2.22}$$

Here the coordinates (x', y') are measured along the longest axis and another axis of the

bar in the Galactic plane. The x'-axis is aligned at an angle θ from the line of sight to the Galactic center from the Sun, with the near side of the bar in the positive-l quadrant. The z-axis is as usual the height above the Galactic plane. These Galactocentric coordinates (x', y', z) are given by

$$x' = R_0 \cos\theta - D \cos b \cos(l + \theta), \tag{2.23}$$
$$y' = R_0 \sin\theta - D \cos b \sin(l + \theta), \tag{2.24}$$
$$z = D \sin b, \tag{2.25}$$

where R_0 is the distance to the Galactic center taken to 8.5 kpc from the Sun. The terms a, b and c define the bar scale lengths, and $M = 1.8 \times 10^{10} M_\odot$ is the total bar mass.

The idea that our Galaxy has a bar at the center is not a new one, first having been suggested by de Vaucouleurs (1964) because of the similarity of the gas dynamics observed in our Galaxy to other barred galaxies. Roughly half of all disk galaxies contain bars (Binney & Tremaine 1987). Binney, Gerhard & Spergel (1991) provided further evidence for a bar from star counts. The DIRBE results of Dwek et al. (1995) were also found to be consistent with this prediction.

To explain the high optical depth, a number of authors have adopted a bar in their Galactic models, and have adopted various values of the bar orientation and mass (Paczyński et al. 1994; Peale 1998; Zhao & Mao 1996). And Evans et al. (1998) proposed that the large optical depth contributions could come from the disk component. Mera et al. (1998), Hansen (1998) and Zhao & Mao (1996) used the Galactic stellar mass function to explain this.

We will compare these values to our results in Chapter 9.

2.3.3 Towards the M31

The microlensing survey towards the M31 is useful for constraining the shape of the dark halo of the Galaxy because of its different line of sight. The AGAPE group (Ansari et al. 1997) and the Columbia group (Crotts 1992; Crotts & Tomaney 1996) have been carrying out microlensing surveys towards M31.

The observation towards M31 is very difficult because in M31 the stellar density is much higher than the LMC and the Point Spread Function (PSF) photometry could not be applied any more. So the AGAPE group use the pixel analysis (Ansari et al. 1997) in which they binned each image into 7×7 pixel bins called super-pixels and measure the flux in each super-pixel. The Columbia group applied the DIA which is sometimes referred to as "image subtraction", which is the origin of the method we applied in this paper. The seeing and sky variation are matched to the reference image and subtracted. Then only variable objects could be detected.

Until now, no definite microlensing events were detected by these groups (Gould & Depoy 1998; Gyuk & Crotts 1999) though hundreds of events per year were expected

(Crotts 1992). Three microlensing candidates were reported in 1996 (Crotts & Tomaney 1996) , but they have been identified as long period variables (Uglesich et al. 1999).

2.3.4 Towards the Spiral Arms

The observation towards the spiral arms is useful to know the structure of the Galactic disk and mass function of the the disk stars. And it is useful to know the disk contribution to the optical depth towards the GB. Many authors estimated the optical depth due to the disk stars. Fux (1997) estimated the spiral arms may contribute 0.5×10^{-6}. A truncated disk would contributed $0.37 - 0.47 \times 10^{-6}$ (Paczyński 1991). A full disk would contribute $0.63 - 0.87 \times 10^{-6}$ (Zhao, Spergel & Rich 1995).

The observation towards the spiral arms has been carried out only by the EROS group (Derue et al. 1999). The results of EROSII presented the optical depth towards the galactic spiral arms of $0.38^{+0.58}_{-0.15} \times 10^{-6}$ (Derue et al. 1999), which is consistent with the predictions, though this is based on just three microlensing events.

2.3.5 Towards the Globular Clusters

Globular clusters are placed towards many lines of sight through the Galactic halo, and therefore these should be useful to determine the structure of the Galactic halo. However the event rate of such observations is small because globular clusters usually have 0.1 millions of stars which is much fewer than the LMC. Furthermore the photometry is very difficult because most of the stars are concentrated in the core with high density. So there is no microlensing program to observe the globular clusters.

Recently, another new approach of the microlensing survey towards the globular clusters has been done by using the HST (Sahu al. 2001). In this case they observed the GB stars as source through the core of the globular cluster M22 as lens objects, where the distance to the lens and the source are well known. They observed the center of M22 every 3 nights for 4 months with HST, and found 7 microlensing events. If these are really microlensing events, they imply that a non-negligible fraction of the cluster mass resides in the form of free-floating planetary mass objects.

2.4 Basic Formulae for EAGLE events

An EAGLE (Extremely Amplified Gravitational LEnsing) event is a microlensing event in which a source star is fainter than the observational limiting magnitude. This faint source would be highly amplified ($u \ll 1$) and then detected as a new star. Nakamura & Nishi (1998) showed that the EAGLE event rate is expected to be fairly high towards the LMC. However an EAGLE search has not been involved in most of the microlensing observation programs based on a DoPHOT-type PSF fitting photometric analysis which measure only stars already detected in the catalogue.

A new CCD photometry method called "the image subtraction method" or "the Difference Image Analysis (DIA)", in which an exposure frame is directly compared with a reference frame, has been developed (Alard & Lupton 1998; Alard 2000; Alcock et al. 1999b, 2000a; Woźniak 2000; Bond et al. 2001). This method enables much more accurate photometry at any place where any star isn't identified on the reference and hence is more powerful for detecting EAGLE events than the current monitoring of visible stars. It is expected that plenty of EAGLE events will be detected with this method in the near future. For example, the MOA collaboration has already started this kind of analysis to find out EAGLE events.

2.4.1 Detection threshold

In an EAGLE event, an invisible star with magnitude V is amplified beyond the observational limiting magnitude V_{obs}. More precisely, to identify an EAGLE event, the source must become brighter than the EAGLE detection threshold $V_{\rm th}$, which is slightly brighter than the observational detection limit V_{obs}. Thus, for an EAGLE event, the amplification A must be larger than the threshold amplitude $A_{\rm th}$, which is written as

$$A_{\rm th} = 10^{0.4(V-V_{\rm th})}. \tag{2.26}$$

We define the threshold impact parameter u_T as the largest impact parameter for an EAGLE event for the source star with magnitude V. The value of u_T is determined so that $A(u_T) = A_{\rm th}(V, V_{\rm th})$. In case of a point source and small impact parameter, one can approximate that $A \approx 1/u$, and then the threshold impact parameter can be written as (Nakamura & Nishi 1998),

$$u_T = 10^{-0.4(V-V_{\rm th})}. \tag{2.27}$$

If the impact parameter would be smaller than u_T, such events could be identified as an EAGLE event. All EAGLE events should have high magnification because of it's nature. These high magnification events have very good opportunity to detect exotic events, such as a finite source event, a parallax event and an extrasolar planet.

2.5 Extrasolar Planet

Gravitational microlensing is a new tool to detect the Extra Solar Planets.

From the first detection of the planetary mass in 1992 (Wolszczan & Frail 1992) and first detection of an extrasolar planet surrounding a main-sequence star (Mayor & Queloz 1995), a total of 34 planets were detected by very precise radial velocity (Doppler) measurements until the end of March 2000 (Perryman (2000)). These recent discoveries have led to a boost in the search for planets by a number of techniques including microlensing, as follows

- Pulsar timing methods: The first detection in 1992 was based on pulsar timing methods; this method measured the deviation of the pulsar timing due to the companion planet.

- Radial velocity measurement: The motion of a planet in a circular orbit around a star causes the star to undergo a reflex circular motion about the star-planet gravitational center. This results in the periodic perturbation in radial velocity. This radial velocity could be estimated by measuring the Doppler shift in the spectrum of the host star.

- Photometry of eclipsing: Another method is measuring the photometric signature of the eclipse of the star by a planet. The first detection of a planet by this method was made by Charbonneau et al. (2000). The principal disadvantage of the method is that it requires configurations in which the viewing direction (to the Earth) lies in the orbital plane of the planet.

- Imaging: Imaging of the brown dwarf is now possible by using latest generation of large (8 – 10 m) telescopes with adaptive optics. However, the imaging low mass extrasolar planet should wait for the future Next Generation Space Telescope (NGST, Mather et al. 1997) and infrared space interferometer etc.

- Astrometric position: Detection of the astrometric movement of stars due to a planet is in $\mu arcsec$. So this would also be possible in the near future with space astrometric satellites such as SIM (Boden et al. 1997) and GAIA (Gilmore et al. 2000).

- Gravitational microlensing: The small perturbation in the photometric light curve could be observed due to the gravity of a small companion planet. These deviations typically last only for a few hours, and hence to detect them well-sampled follow up observation of the events are needed. This method is sensitive to lower mass than the Earth mass with relatively large orbit radii around the distant star ($\sim$ kpc).

The most successful and widely used method to date has been radial velocity measurement. However, it is very difficult to detect planets with Earth-like masses or large orbital radii with radial velocity measurements since they couldn't perturb the motion of a host star enough to measure. To know the nature of Earth-like planets is interesting, and this could be done only with the microlensing technique at the present time.

Rhie et al. (2000) and Bond et al. (2002) detected the first signal of planet in the high magnification microlensing event MACHO 98-BLG-35 shown in the upper panel of Figure 2.5 with the best single lens fit curve. The residual from the best single lens fit is also shown in the lower panel. The deviation from the best single lens fit due to the planet in the light curve near the peak can clearly be seen. The planet model fit light curves are shown in Figure 2.6, and the position of the planet and the caustic, which is the locus of points where a point source would be infinitely magnified by the lens system of this planet model, is shown in Figure 2.7. The best planetary model for this event has a planet of mass $\sim (0.4 - 1.5) M_{\oplus}$ at a projected radius of either ~ 1.5 or ~ 2.3 AU.

Mao & Paczyński (1991) and Gould & Loeb (1992) investigated that in microlensing events in which one or more planets orbit the primary lens, the detectable fine structure in the photometric signature occurs relatively frequently, even for low-mass planets. Gould & Loeb (1992) found that the probability of detecting such fine structure is about 17% for

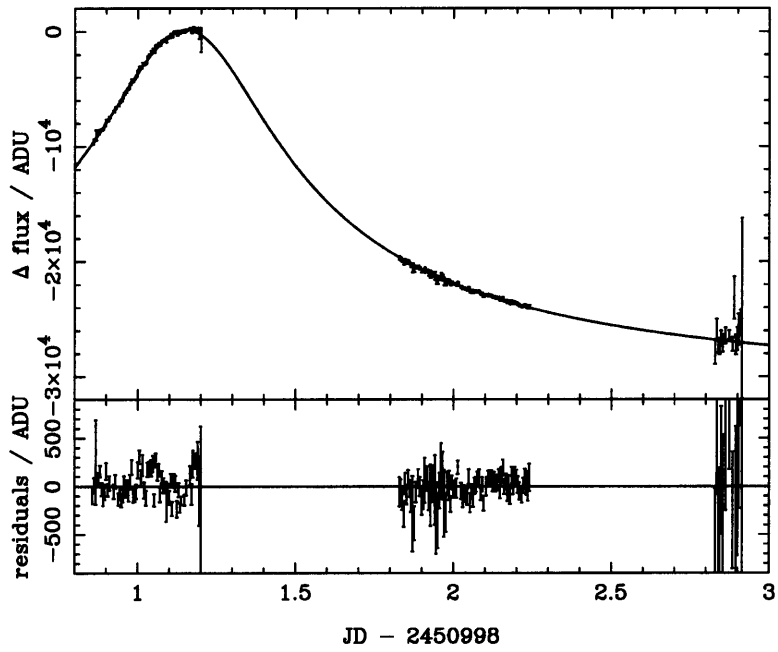

Figure 2.5: The light curve for event MACHO 98-GLG-35 obtained by the MOA group in the red passband using subtraction photometry (Bond et al. 2002) in the upper panel. The best single lens fit to the data is also shown. The deviation from the best single lens fit in the light curve near the peak can clearly be seen in residual plots in the lower panel.

a Jupiter-like planet (i.e. at about 5 AU from the central star), and 3% for a Saturn-like system. These relatively high probabilities occur specifically when the planet lies in the "lensing zone" between about $0.6-1.6$ AU (Wambsganss 1997). The calculations of Bennet & Rhie (1996) indicate that 2% of the $M_{\oplus}$ (Earth mass) planets and 10% of the $10M_{\oplus}$ planets in the lensing zone ($1-4$ AU) can be detected via microlensing. Bolatto & Falco (1994) noted that 40% of events could yield Jupiter-mass planets.

Griest & Safizadeh (1998) presented that for high magnification events ($u_{min} < 0.1$), the detection probability could be close to 100%. From this suggestion, the PLANET and GMAN groups are performing frequent follow-up observations for high magnification microlensing events which are alerted by MACHO, OGLE and MOA (in 2001, only MOA was issuing alerts).

So, especially, MOA is aiming to detect EAGLE-type events which must be high magnification events towards the GB. Hence we are observing the GB very frequently ($5 \sim 6$ times a night) and analyzing with DIA in real-time. It is important to know how efficiently our observation could detect EAGLE-type high magnification events. We estimate our detection efficiency for such events in Chapter 8.

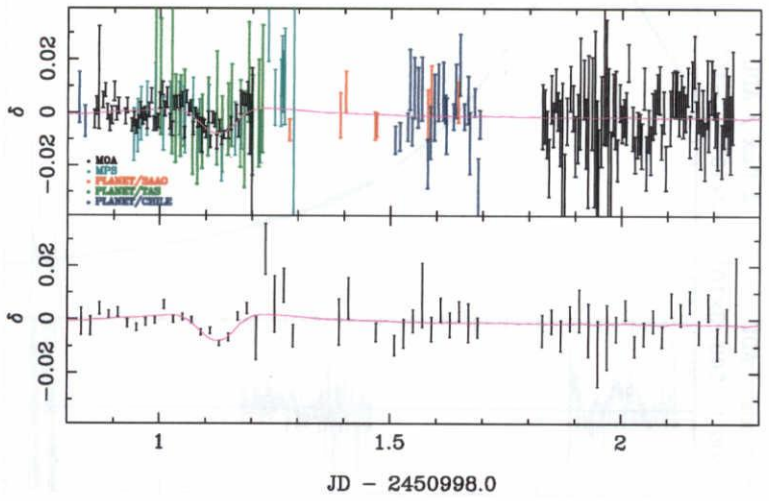

Figure 2.6: The residual light curve of event MACHO 98-GLG-35 with the data of MOA, MPS and PLANET groups (Bond et al. 2002) with the planet model fit light curve. The top figure shows all the data while the lower figure shows the data binned and weight averaged on a 0.02-day interval.

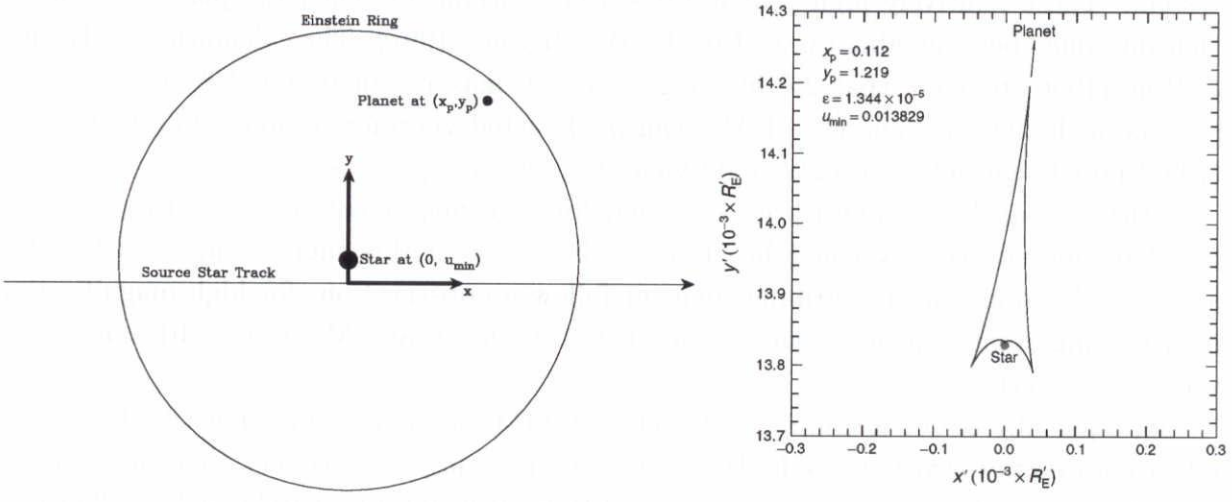

Figure 2.7: The schematic view of the position of the host lens star and planet (left panel). Right panel show the caustic which is the locus of points where a point source would be infinitely magnified by the lens system of this planet model. The source star moves horizontally left-to-right through the origin.

Chapter 3

New Methods for Constraining the Lens Location

3.1 Constraining the Location of Microlensing Objects by using the Finite Source Effect in EAGLE events

We propose a new method to constrain the location of microlensing objects using EAGLE events. We have estimated the rate of EAGLE events by taking the finite source effect into account. We found that the EAGLE event rate when using a 1-m class telescope whose limiting magnitude is $V \sim 21$ is the same as or higher than that of the ordinary microlensing events which have been found to date. We have also found that the fraction of transit EAGLE events is large enough to detect: between $4 \sim 80\%$ depending on the lens location. Since the lens proper motion can be measured for a transit event, one can distinguish whether the lens is a MACHO in our halo or one of the known stars in the Large Magellanic Cloud (LMC) from the proper motion measurement for each transit EAGLE event. Moreover, we show that the fraction of transit EAGLEs in all EAGLE events significantly depends on the lensing locations: the transit EAGLE fraction for the self-lensing case is $2 \sim 15$ times larger than that for halo MACHOs. Thus, one can constrain the location of lens objects by the statistics of the transit events fraction. We show that we can reasonably expect $0 \sim 6$ transit events out of 21 EAGLE events in 3 years. We can also constrain the lens population properties at a greater than 99% confidence level, depending on the number of transit events detected. We also present the duration of EAGLE events, and show how an hourly observational mode is more suitable for an EAGLE event search program.

3.1.1 Finite Source Effect

The microlensing light curve informs us only of the event timescale t_E, in which the mass, velocity and distance of the lensing object are degenerate, and thus it is difficult to deter-

mine the mass or the distance of the lensing object for each microlensing event. Therefore, the nature of MACHOs in the Galactic halo still remains unclear, and one cannot rule out the possibility that the microlensing events are not caused by MACHOs in the Galaxy's halo but by unknown populations lying between the Galaxy and the Clouds (e.g., Zaritsky & Lin 1997; Zhao 1998), or by normal stars in the Clouds themselves (e.g., Sahu 1994).

In order to understand the nature of lensing objects, some additional information that partially or fully breaks the three-fold degeneracy is required. Over the past years several investigations have been made to extract additional information from special types of microlensing events, examples of which are binary events and parallax events, for which the lens proper motion and lens distance can be constrained (e.g., Schneider & Weiss 1986; Alcock et al. 1995; Miyamoto & Yoshii 1995). A transit event, in which the lens transits the extended surface of the source star, is another example of such types of microlensing events (Gould 1992, 1994a; Nemiroff & Wickramasinghe 1994; Witt & Mao 1994; Peng 1997). When the lens passes over the surface of the source star, the point source approximation fails and the peak of the light curve deviates from that for a point source. From such a light curve, one can derive the radius of the source star scaled by the Einstein ring radius projected onto the source plane. Since the radius of the source star can be estimated from its spectrum, one can obtain the proper motion of the lens for transit events. The proper motion of the lens will be of great use in investigating the lens location, as the expected proper motion distribution of objects in the Galaxy's halo differs significantly from that in the Clouds. Unfortunately however, the probability for transit events is expected to be extremely small ($\sim 0.1\%$) for normal microlensing events (Gould 1994a).

The probability of transit events is relatively high for EAGLE events, in which an invisible star is amplified above the detection limit, because EAGLE events are guaranteed to have a small impact parameter (Wang & Turner 1996; Gould 1997; Nakamura & Nishi 1998). Since there are many more faint stars below the detection limit than visible stars that are usually used for a microlensing search, the EAGLE event rate is expected to be fairly high (Nakamura & Nishi 1998). However EAGLE events have rarely been seen in the current observation programs in which the brightness of visible stars is measured based on a DoPHOT-type analysis. However, DIA is much more powerful for detecting EAGLE events than DoPHOT, and one can expect that plenty of EAGLE events will be detected with this method in the near future. If many EAGLE events are detected, one may be able to find several transit events because EAGLE events have small impact parameters. Therefore, a search for EAGLE events will possibly provide a new opportunity to measure the lens proper motion in transit events, and thereby to constrain strongly the lens location. Furthermore, statistics of transit EAGLE events alone may be useful for studying the nature of lensing objects. The fraction of transit events depends on the ratio of the physical radius of the source star R_* to the Einstein radius r_E in the source plane, i.e. R_*/r_E. In the case where the lenses are the stars in the LMC itself (self-lensing), the Einstein radius r_E in the source plane is much smaller than in the case where the lenses are MACHOs in the Galactic halo. Thus the fraction of transit EAGLE events out of all EAGLE events for self-lensing in the LMC will be much larger than that for lensing due

to MACHOs in the halo. Therefore the fraction of transit EAGLE events may be used to constrain the location and the nature of the lens.

EAGLE events will thus become one of the most powerful tools for investigating the nature of lensing objects.

3.1.2 Basic equations for EAGLE with the finite source effect

Basic equations for EAGLE events are given in section 2.4.1 using the point source approximation. However, in most of the cases we are interested in, the effect of a finite source is not negligible, and this approximation is not applicable. We thus calculate the threshold impact parameter u_T by taking the finite-source effect into account.

When the source size is finite, the amplification A cannot be given by equation (2.12), but approximated by the following expression (Gould 1994a),

$$A_{\rm fin}(u, u_*) = A(u)B(z), \quad z \equiv \frac{u}{u_*}, \quad u_* \equiv \frac{D_d}{D_s}\frac{R_*}{R_E} = \frac{R_*}{r_E}. \tag{3.1}$$

Here u_* is the source radius scaled by r_E (R_* is the physical radius of the source), and z is the impact parameter in the source plane scaled by the radius of the source star R_*. The function $B(z)$ describes the ratio of the amplification of a finite source to the amplification of a point source, which is written as

$$B(z) = \frac{z^2}{\pi}\int_0^{2\pi} d\theta \int_0^{1/z} dq\; q(1+q^2+2q\cos\theta)^{-1/2}. \tag{3.2}$$

We show the relation of the amplification and other parameters in Figure 3.1.

To compute the amplification using equations (3.1) and (3.2), one has to know the physical size of the source star that has a magnitude of V. In this section, we approximate the relation between R_* and V for a main sequence star (Allen 1973; Blaauw 1963) as follows,

$$\begin{aligned} R_*(V) &= 10^{-0.053V+1.22}, \qquad (21 \le V \le 31) & (3.3)\\ &= 10^{-0.125V+2.78}, \qquad (15 \le V \le 21). & (3.4) \end{aligned}$$

Using equations (3.1), (3.2), (3.3) and (3.4), one can derive the threshold impact parameter u_T from the condition that $A_{\rm th} = A_{\rm fin}(u_T, u_*)$.

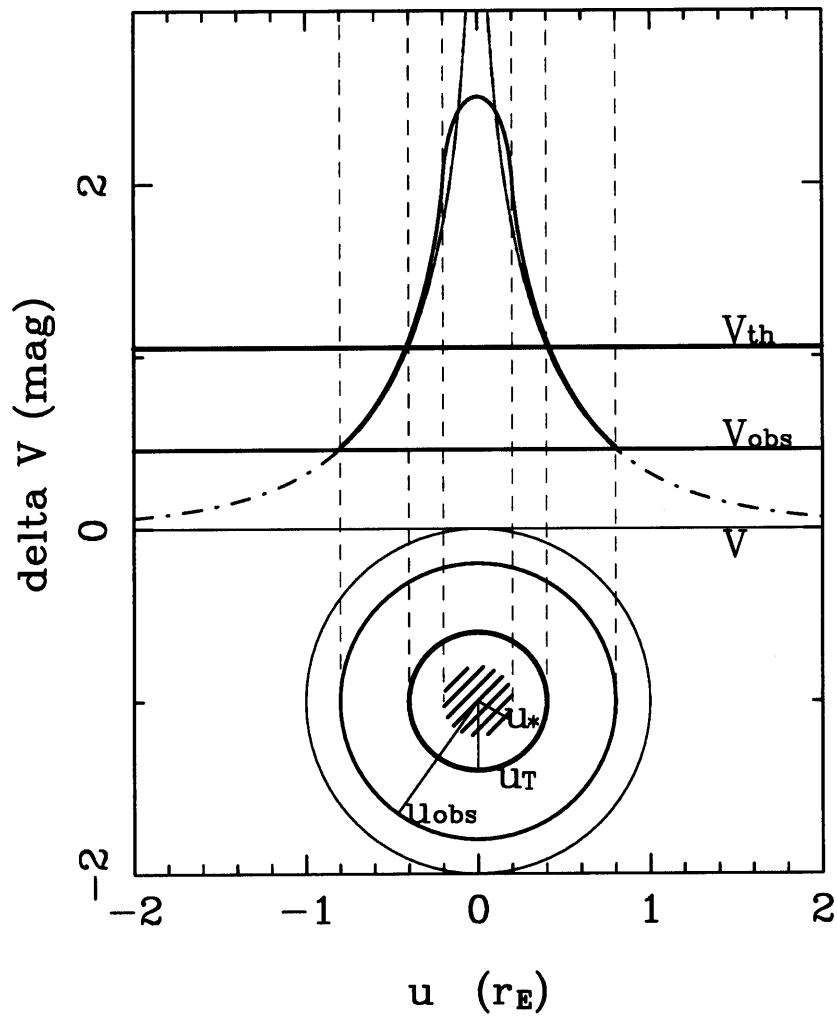

Figure 3.1: A schematic view of the parameters for an EAGLE event with and without the finite source effect. The thin and dot-dashed lines are the visible and invisible light curves for a point source. The thick curve is the visible light curve from a finite source. The outer thin circle is the Einstein radius, and the other impact parameters defined in section 2.4.1 and 3.1.2 are also shown. When u becomes smaller than u_{obs}, the star becomes visible, and when u becomes smaller that u_T, the event is identified as an EAGLE event.

3.1.3 Mass and luminosity function of source stars

The EAGLE event rate depends heavily on the mass function and the luminosity function of source stars in the LMC and the SMC. Following Nakamura & Nishi (1998), we assume that a stellar initial mass function is in the power law form with index α, that the star formation rates in the LMC have been constant for 5 Gyr and was zero before 5 Gyr ago. Assuming that the lifetime of the Sun is 10 Gyr, we obtain the present day mass function as

$$\begin{aligned} \phi(M) &= CM^{-\alpha}, & (M_l < M < 1.4M_\odot) & \quad (3.5) \\ &= 2(\frac{M}{M_\odot})^{-2}CM^{-\alpha}, & (1.4M_\odot < M < M_u) & \quad (3.6) \end{aligned}$$

where M_l and M_u are the lower and the upper mass limit of the stars, respectively. The initial mass function of the stars in the LMC is not so different from the Salpeter IMF with $\alpha = 2.35$ (Holz & Wald 1996). However for field stars the slope may be as steep as $\alpha \sim 5.0$ (Westerlund 1997). In the following analysis we use the two extreme values of α, 2.35 and 5.0. We note that the results in the following sections do not depend strongly on the shape of the mass function beyond $M = 1.4M_\odot$ because the contribution of low mass stars is much more significant than that of massive stars.

The mass-luminosity relation of the main sequence stars is expressed by (Kippenhahn & Weigert 1990)

$$L(M) = L_\odot(\frac{M}{M_\odot})^3 \quad (3.7)$$

The Bolometric Correction ($B.C.$) can be approximated as (Schild et al. 1971; Davis & Webb 1970; Johnson 1964)

$$\begin{aligned} B.C. &= 0.6V - 11.6, & (13 \leq V \leq 19) & \quad (3.8) \\ &= 0, & (19 \leq V \leq 24) & \quad (3.9) \\ &= -0.37V + 8.9. & (24 \leq V \leq 31) & \quad (3.10) \end{aligned}$$

Then we can drive the V band luminosity function of stars in the LMC using equations (3.5) to (3.10).

$$\begin{aligned} \phi_L(V) &= C'10^{-(\alpha+2)(V+B.C.)/(-7.5)}, & (15 < V < 21) & \quad (3.11) \\ &= C''10^{-\alpha(V+B.C.)/(-7.5)}. & (21 < V < 31) & \quad (3.12) \end{aligned}$$

In this section we will use these mass and luminosity functions.

3.1.4 EAGLE Event Rate

In this section we estimate the EAGLE event rate. Instead of the absolute event rate, we estimate the relative event rate normalized with the rate for normal microlensing events. When a lens object passes the line of sight with a normalized impact parameter $u = d/R_E$,

the source star is amplified according to equation (2.12), where d is the distance from the lens to the source in the lens plane. A microlensing event is defined as a phenomenon where the source star is amplified more than the given threshold amplification $A_{\rm th}$. This occurs whenever a lens enters the microlensing "tube" whose radius is $u_{th}R_E$, where u_{th} is the detection threshold impact parameter corresponding to $A(u = u_{th}) = A_{\rm th}$ (Griest 1991). This means that all detected microlensing events have to satisfy $d \leq u_{th}R_E$. The probability that a lens passes this region is proportional to the length of this radius $u_{th}R_E$. For a normal microlensing event u_{th} is set to be unity corresponding to $A_{\rm th} = 1.34$, and for an EAGLE event we use u_T defined in section 3.1.2 as u_{th}. Hence the event rate is proportional to $u_{th}R_E = R_E$ for a normal microlensing event and $u_{th}R_E = u_TR_E$ for an EAGLE event, i.e., these event rates are proportional to the radius of each appropriate circle in Figure 3.1 and Einstein radius R_E.

The event rate is proportional to the density distribution of the lens $n_s(M, D_d)$ (Griest 1991). The event rate is also proportional to the number of source stars which is expressed as the luminosity function of source stars $\phi_L(V)$ in the LMC. Moreover, the event rate should be averaged over the probability distribution of the mass of the lenses using the mass function $\phi(M)$. Thus, the differential form of the event rate averaged over the source stars for normal microlensing events is written as

$$d\Gamma_N \propto R_E\phi_L(V)\phi(M)n_s(M, D_d)dD_ddD_sdVdM. \tag{3.13}$$

Note that the integration with respect to V means averaging over the source stars. Similarly, the differential form of the rate for EAGLE events can be expressed as

$$d\Gamma_E \propto u_TR_E\phi_L(V)\phi(M)n_s(M, D_d)dD_ddD_sdVdM. \tag{3.14}$$

Note that the threshold impact parameter u_T appears in the case of EAGLE events, since the event rate for EAGLE events is proportional to u_TR_E instead of R_E. To calculate the normal and the EAGLE event rates, we must integrate them over the possible ranges of the parameters.

The normal event rate Γ_N can be estimated as

$$\Gamma_N = C\int_V\int_M\int_{D_s}\int_{D_d} d\Gamma_N, \tag{3.15}$$

where the integration is performed over the following ranges.

$$D_{d,min} \leq D_d \leq D_s, \tag{3.16}$$
$$D_{s,min} \leq D_s \leq D_{s,max}, \tag{3.17}$$
$$M_l \leq M \leq M_u, \tag{3.18}$$
$$V_l \leq V \leq V_{obs}. \tag{3.19}$$

Here M_l and M_u denote the lower and the upper mass limit for the mass function, and V_l denotes the luminous end of the luminosity function $\Phi_L(V)$. Similarly, the EAGLE event rate Γ_E can be estimated as

$$\Gamma_E = C\int_V\int_M\int_{D_s}\int_{D_d} d\Gamma_E. \tag{3.20}$$

Note that the integral ranges for D_d, D_s and M are the same as for Γ_N, but V is in the range:

$$V_{obs} \leq V \leq V_u. \tag{3.21}$$

Note that V_u denotes the faint end of the luminosity function.

Since the constant C is equal in both equations, one can easily obtain the ratio Γ_E/Γ_N by integrating the above equations numerically. As for the integral ranges for the luminosity in the LMC stars, we assume that $V_l = 15$ and $V_u = 31$. We note that the results are not affected strongly by stars outside this magnitude range. We also assume $V_{obs} = 21$, which is a typical observational limit for current microlensing programs. We consider two different values for the threshold magnitude; $V_{th} = 19$ and 20 .

We calculate these integrals in the case where the lenses are stars in the LMC itself (self-lensing) and in the case where the lenses are MACHOs in the halo. For these two cases, there are the following differences which arise in the integral ranges of (M, D_s and D_d) and the functions of ($n_s(M, D_d)$ and $\phi(M)$).

i) In the case where the lenses are known stars in the LMC itself, for simplicity, we assume a constant spatial density distribution of the lens $n_s(M, D_d)$ with depth $d_{max} = D_{s,max} - D_{s,min}$. For the depth of the LMC d_{max}, one finds that the bar can be as thin as the disk itself (Binney & Tremaine 1987), and the thickness of the LMC disk is about 300pc (Westerlund 1991). Since there is not any more accurate information, we adopt two values, 300 pc and 1 kpc. We also assume that the distance to the LMC is 50 kpc, and also assume $M_l = 0.1M_\odot$, $M_u = 50M_\odot$ for the lens mass distribution expressed by equations (3.5) and (3.6) in the case of self-lensing.

ii) In the case where the lenses are MACHOs in the halo, we fix $D_s = 50$ kpc and integrate with D_d from $D_{s,min} = 0$ to $D_s = 50$ kpc. We also adopt the standard halo model for the spatial distribution of the lens $n_s(M, D_d)$ as follows (Griest 1991):

$$n_s(M, D_d) = \frac{\rho}{M} = \frac{\rho_0}{M}\frac{a^2 + r_0^2}{a^2 + r^2} \tag{3.22}$$

where $\rho_0 = 0.0079\ M_\odot \mathrm{pc}^{-3}$ is the local mass density, r is the Galactocentric radius, $r_0 = 8.5$ kpc is the Galactocentric distance of the Sun, and $a = 5$ kpc is the core radius. We also assume a delta function mass distribution for MACHOs, and we take two values of M; $M = 0.1M_\odot$ and $1.0M_\odot$.

The results for $V_{\rm th} = 19$ and 20 are listed in Table 3.1, and the probability distribution of EAGLE events as a function of the source magnitude V is shown in Figure 3.2. From these results we conclude the following:

1) From the results in Table 3.1 we can expect the EAGLE event rate is of the same order (~ 7 events/yr) as the rate for normal events when $\alpha = 2.35$, and much larger ($70 \sim 170$ events/yr) when $\alpha = 5.0$. Here we assume the normal event rate $\Gamma_N = 4$ events/yr (Alcock et al. 1997b). Thus, the event rate for EAGLEs is high enough to allow the events to be detected.

2) The event rate for EAGLEs for $\alpha = 5.0$ is $8 \sim 25$ times higher than that for $\alpha = 2.35$. This strong dependence of the EAGLE event rate on α indicates that we can obtain some information on the power index α of the mass function of stars in the LMC from the EAGLE event rate.

3) When $\alpha = 5.0$, the EAGLE event rate for halo MACHOs is 3 times higher than that for the self-lensing case. So if $\alpha = 5.0$, it is possible to determine whether the lens masses are MACHOs in the halo or known stars in the LMC itself from the event rate of EAGLEs.

4) In Figure 3.2, we can see the EAGLE event probability decreases for large V, though the number of stars increases with increasing V. The reasons are that u_T is small for large V and the source can not be amplified enough to be observed due to the finite-source effect. Also, if $\alpha = 5.0$, the distribution of the source star magnitudes may be useful for determining whether the lens masses are MACHOs in the halo or are stars in the LMC, because this distribution is significantly different in each case (see Figure 3.2).

Table 3.1: The ratio of event rate of EAGLEs to normal events

V_{th} (mag)	α	halo ($M = 0.1M_\odot$)	halo ($M = 1M_\odot$)	self ($d_{max} = 300pc$)	self ($d_{max} = 1kpc$)
19	2.35	0.72	0.73	0.60	0.65
19	5.0	15.7	17.9	4.71	6.46
20	2.35	1.83	1.83	1.67	1.73
20	5.0	44.5	45.0	18.6	23.2

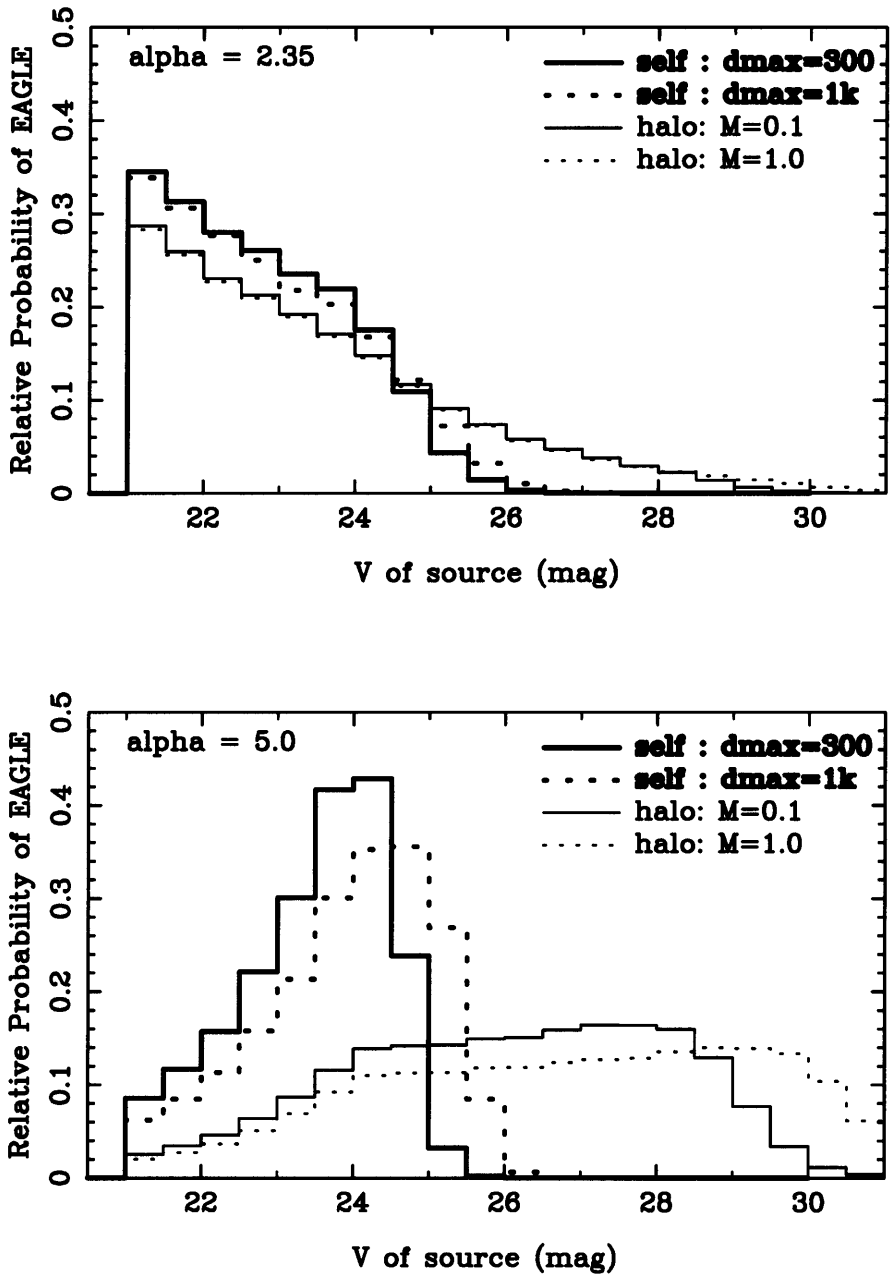

Figure 3.2: The probability of an EAGLE event as a function of the source magnitude V for $V_{th} = 19$. The upper and lower panels are for $\alpha = 2.35$ and 5.0 respectively. The bold solid and dashed lines correspond to self-lensing for $d_{max} = 300$ pc and 1 kpc respectively. The thin solid and dashed lines correspond to halo MACHOs with masses of $M = 0.1M_{\odot}, 1.0M_{\odot}$ respectively. Although the number of the stars with magnitude V increases as V increases, the EAGLE event probability decreases for large V because of small u_T values and the finite source effect. When $\alpha = 5.0$, the distribution of V is significantly different for the case of self-lensing and the halo MACHOs.

3.1.5 Fraction of Finite Source Transit events

In this section, we investigate the fraction of transit EAGLE events in all EAGLE events. The finite-source effect appears when z becomes smaller than about 2 (Gould 1994a), where $z \equiv u/u_*$ is the impact parameter (in the source plane) scaled by the radius of the source star R_* (see section 3.1.2) and u_* is defined in equation (3.1) as the source star radius normalized by the Einstein radius in the source plane. However, when $1 < z < 2$, the effect is not strong and it is quite difficult to determine whether the event is a transit event or a non-transit event (Peng 1997). Therefore, here we define a transit event as an event with $z < 1$.

The event rate of EAGLEs is proportional to $u_T R_E$ (see section 3.1.4), and similarly, the probability that the lens transits the surface of the source star is proportional to $u_* R_E$. In short, these rates are proportional to the radius of the corresponding circle in Figure 3.1.

Thus, the ratio of the transit EAGLE event rate to the total EAGLE event rate is proportional to u_*/u_T. In order to estimate the mean value of the fraction of transit EAGLE events, one must integrate this ratio over all possible parameter ranges as above, in section 3.1.4. The mean value of this fraction can be estimated by evaluating the following:

$$\langle \frac{u_*}{u_T} \rangle = \frac{1}{\Gamma_E} C \int_M \int_V \int_{D_s} \int_{D_d} \frac{u_*}{u_T} \, d\Gamma_E. \tag{3.23}$$

The results for $V_{\rm th} = 19$ and 20 are shown in Table 3.2. From these results we conclude the following:

1) The fraction of transit events in all EAGLE events is much higher than that for normal events ($\sim 0.1\%$) (Gould 1994). So we can expect a few transit EAGLE events per year using a 1-m class telescope depending on the lens location. If we obtain an accurate light curve and a good estimate of the radius of the source star by follow-up observations, we can get the proper motion of the lens for each event (Gould 1994a). Since the lens proper motion is useful for constraining the lensing location (and so the lens population), we can determine the location of the lens for each event.

2) Moreover, the fraction of transit events strongly depends on whether the lens is in the halo or in the LMC. The transit fraction for the self-lensing case for $\alpha = 2.35$ is $4 \sim 15$ times larger than that for the halo MACHO lensing case (for $\alpha = 5.0$, $2 \sim 5$ times larger). We can constrain the power index α using the event rate (see Table 3.1) and the distribution of the source star magnitude (see Figure 3.2). Hence, if we can measure the fraction of transit events in all EAGLE events, we will be able to constrain the lens location (and so the lens population) statistically.

So the EAGLE event search will be of great importance in investigating the location and the nature of the lensing objects. We discuss some quantitative examples about these in section 3.1.7.

Table 3.2: The fraction of transit events in all EAGLEs

V_{th} (mag)	α	halo ($M = 0.1M_\odot$)	halo ($M = 1M_\odot$)	self ($d_{max} = 300$ pc)	self ($d_{max} = 1$ kpc)
19	2.35	0.09	0.04	0.45	0.34
19	5.0	0.40	0.25	0.82	0.72
20	2.35	0.05	0.02	0.29	0.22
20	5.0	0.29	0.12	0.67	0.59

3.1.6 Event Duration

In this section, we estimate the duration, t_{EAGLE} of an EAGLE event. We define the duration of an EAGLE event t_{EAGLE} as the time when the source star becomes brighter than the observation apparent magnitude threshold V_{obs}. The critical amplification A_{obs} is written as $A_{obs} = 10^{0.4(V-Vobs)}$. If $A_{obs} > 2.5$, we use equation (3.1) to derive u_{obs}. On the other hand, when $A_{obs} \leq 2.5$, we use the standard equation (2.12), because equation (3.1) is invalid and the finite-source effect is negligible in this case. The mean value of t_{EAGLE} for the event with source magnitude V can be written as

$$\langle t_{EAGLE}(V)\rangle = 2t_E \frac{1}{u_T}\int_0^{u_T}\sqrt{u_{obs}^2 - u_{min}^2}du_{min}, \quad t_E = \frac{R_E}{v_t} \tag{3.24}$$

$$\simeq 1.94 t_E u_{obs}(V), \qquad (V_{\rm th} = 20) \tag{3.25}$$

$$\simeq 1.98 t_E u_{obs}(V), \qquad (V_{\rm th} = 19) \tag{3.26}$$

where t_E is the true event timescale of the microlensing event and v_t is the transverse velocity of the lens object relative to the observer-source line of sight. We assume $v_t = 220$ km/s for the MACHOs in the halo and $v_t = 30$ km/s for the stars in the LMC.

The mean value of $\langle t_{EAGLE}(V)\rangle$ averaged over all possible values of distance, lens mass and source magnitude is:

$$\langle t_{EAGLE}\rangle = \frac{1}{\Gamma_E} C \int_M \int_V \int_{D_s} \int_{D_d} \langle t_{EAGLE}(V)\rangle d\Gamma_E. \tag{3.27}$$

The results for $V_{\rm th} = 19$ and 20 are shown in Table 3.3, and the probability distribution of t_{EAGLE} for EAGLE events is shown in Figure 3.3. In Figure 3.3, the distributions are shifted to shorter durations for $\alpha = 5.0$ with respect to those for $\alpha = 2.35$ because the number of dim sources for EAGLEs increases. We can also see a cut-off in the probability curves at smaller t_{EAGLE} for self-lensing. This is because the event rate of EAGLEs whose impact parameter is smaller than some threshold value decreases according to the finite-source effect. From Figure 3.3, we can see that the duration of the EAGLE is usually short (1 day $\sim$ 40 days), especially when $\alpha = 5.0$. Hence, the nightly observational mode currently undertaken is not adequate for detecting EAGLE events, but an hourly observational mode is more suitable for detecting EAGLE events. If observations are made several times per night, there will be sufficient time resolution to detect the EAGLE events and to issue an alert for an occurring EAGLE event.

Table 3.3: The mean EAGLE event duration $\langle t_{EAGLE} \rangle$

V_{th} (mag)	α	halo ($M = 0.1M_{\odot}$)	halo ($M = 1M_{\odot}$)	self ($d_{max} = 300$ pc)	self ($d_{max} = 1$ kpc)
19	2.35	21.2	66.6	25.8	43.8
19	5.0	3.6	10.0	7.7	10.6
20	2.35	20.6	65.2	22.9	40.3
20	5.0	3.1	9.8	5.0	7.4

Note: The value of $\langle t_{EAGLE} \rangle$ is given in day.

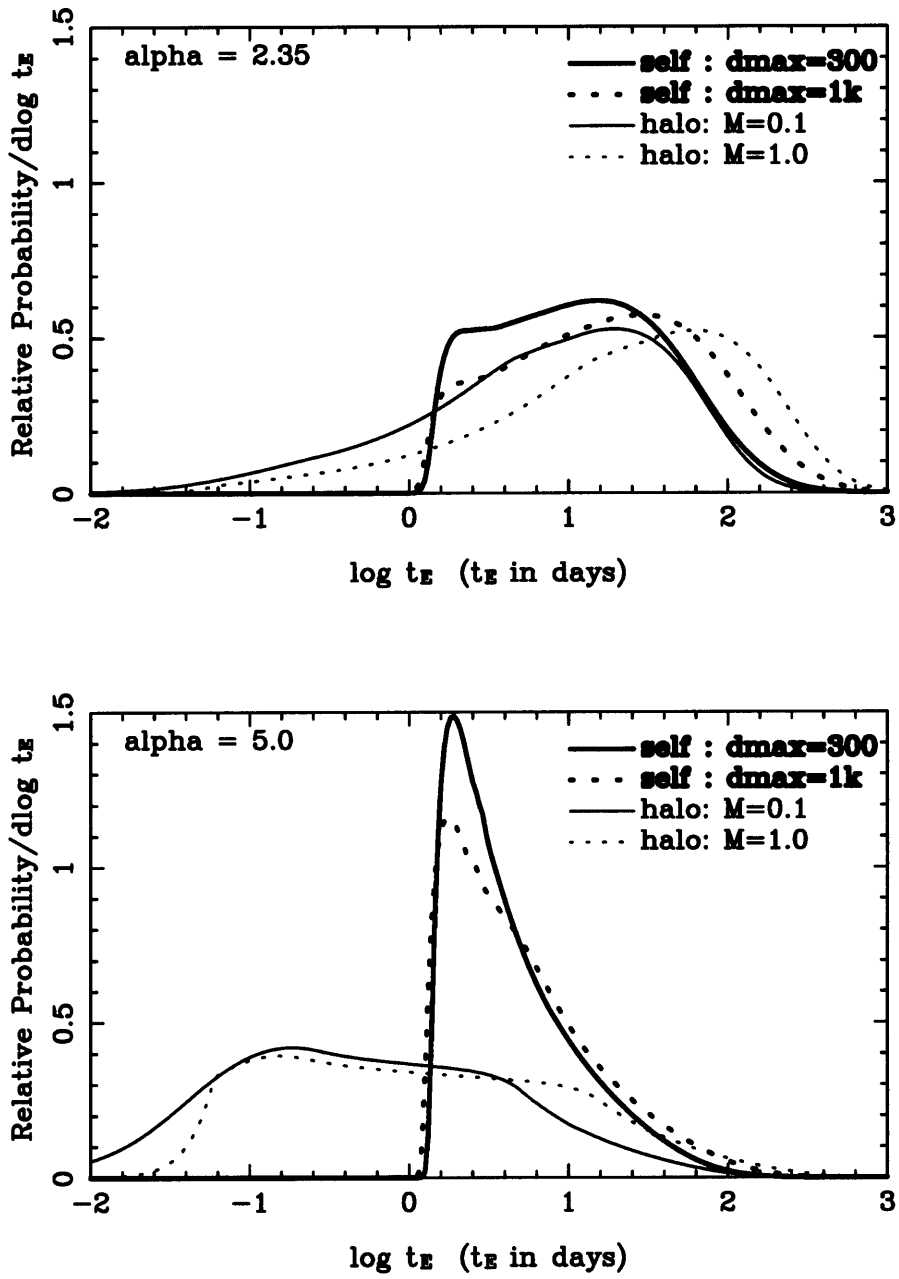

Figure 3.3: The probability distribution of the EAGLE event duration t_{EAGLE} for $V_{th} = 19$. The upper and lower panels are for $\alpha = 2.35$ and 5.0 respectively. The bold solid and dashed curves correspond to LMC self-lensing with $d_{max} = 300pc$ and $1kpc$ respectively. The thin solid and dashed curves correspond to halo MACHOs with MACHO masses of $M = 0.1M_{\odot}$ and $1.0M_{\odot}$ respectively. The distributions are shifted to smaller t_{EAGLE} values for $\alpha = 5.0$ than that for $\alpha = 2.35$ because the number of dim sources for EAGLEs increases. We can see a cut-off in the low t_{EAGLE} side of the curves in the self-lensing case. This is because the event rate of EAGLEs whose impact parameter is smaller than some threshold value decreases due to the finite-source effect.

3.1.7 Discussion on the Observation Strategy

We have seen that the EAGLE event rate is as high as that for normal events. Since the duration of an EAGLE event is usually short (1 day $\sim$ 40 days), the nightly observation program currently undertaken by most groups is not adequate. Hourly observation is necessary for finding EAGLE events. Moreover, monitoring with a 1-m class telescope is sufficient to search for EAGLEs and to make follow up observations near the peak, but not enough to follow up the wing of the light curve. This is because the source is visible only at the peak of the light curve but invisible during most of the remainder of the event. To get the overall structure of the light curve, one has to observe the event with a larger telescope for a longer period (but we do not need to observe so frequently).

Current microlensing experiments are being carried out toward very dense stellar fields. So, the determination of the absolute flux of the source has been an issue in microlensing because of source star blending. In the case of EAGLE events, the source stars are fainter than the detection limit and thus the blending of brighter stars is significant, making the problem worse. Attempts have been made to correct the blending effects for individual events by introducing an additional parameter, the blended flux, but this method suffers from very large uncertainties in the derived lensing parameters due to degeneracies among the parameters (Alard 1997; Han 1997). One solution to correct for blending problem is to use the Hubble Space Telescope (HST). The high resolving power of the HST and the color information from ground-based observations enable us uniquely to separate the lensed source star from blended stars (Han 1997). The DIA should be used to locate the centroid of the lensed flux in the ground-based event image accurately to find the lensed star in the HST image. Other high resolution telescopes like the VLT are also good candidates for performing follow-up observations. Using a large telescope is also required for spectroscopic observations of the source star, from which one can estimate the source radius. We can do this even after the event has finished.

Using the DIA has another advantage in microlensing experiments. The color change induced by the limb-darkened extended source helps the measurement of the proper motion of the lens and increases the possible number of proper motion measurement events (Witt 1995; Gould 1996). Han (2000) found the color change measurement by using the DIA enables one to obtain the same information about the lens and the source star, but with significantly reduced uncertainties due to the absence of the blending effect. So measuring the color change with differential photometry helps to derive the proper motion of the lens along with the other microlensing parameters, and at least, to inform us whether a lens transited the surface of the source or not without requiring the absolute baseline flux. This information is useful in understanding the location of the lens object which we discuss below.

In order to perform follow-up monitoring and spectroscopic observations, one has to detect an EAGLE event in real-time and issue an alert. For the real-time detection of EAGLE events, the DIA is more suitable than the DoPHOT analysis or the pixel analysis, since the DIA can detect the luminosity variation at any position of the fields, even where

no star was identified previously. Thus, the most reasonable and practical observation strategy is to observe hourly (with a 1-m telescope) and to perform the real-time analysis with the DIA. An alert can then be issued to observers around the world, enabling frequent observations around the event peak. After that, high resolution observations with larger telescopes should be carried out to determine the baseline flux of the source.

As seen in section 3.1.5, a large fraction of EAGLE events is likely to be transit EAGLE events. If we can issue an alert for such an EAGLE event, observations with the global network will allow us to obtain a precise light curve near the maximum amplification. Because the transit time is $\approx$ 13 hours for self-lensing and $\approx$ 2 hours for halo MACHOs, it is possible to measure precisely the light curve in the transit region. Since the overall structure of the light curve can be determined by follow-up observations with larger telescopes, one can obtain the source radius scaled by Einstein radius u_* from the full light curve and from the color change measurements due to a limb-darkened extended source (Han 2000). If one can obtain u_* and also the radius of the source star R_* from the color of the source star, one can obtain the Einstein radius r_E projected onto the source plane. Since the event duration t_E can also be determined from the full light curve, one can measure the proper motion of the lens object for a transit EAGLE event (Gould 1994a). The proper motion of the lens object is of great use in determining the lens location. Since the proper motion of objects in the halo is 30 $\sim$ 40 times larger than that of stars in the LMC, one can know whether the lensing object exists in the halo or not from the proper motion of transit EAGLE events. Even if we cannot derive an accurate proper motion of lens, the fraction of transit events can be used to constrain the lens location, because that ratio for the self-lensing case is 2 $\sim$ 15 times larger than that for the halo MACHOs case.

To demonstrate how we can constrain the nature of microlensing objects, we show in Figure 3.4 the probability distribution of the transit events for both the halo lensing case and the LMC self-lensing case. For the typical parameters $\alpha = 2.35$, $V_{th} = 20$ and a detection efficiency of 50%, one can expect to find $\sim$ 21 EAGLE events after a 3 year observation period of 11 square degrees of the LMC central region (as the MACHO collaboration does). In these 21 EAGLE events, we can expect 1.1 (0.4) and 6.1 (4.6) transit events for halo MACHOs whose mass is 0.1 $M_\odot$ (1.0 $M_\odot$) and for self-lensing with $d_{max} = 300$ pc (1 kpc), respectively. So if we do not detect any transit events in 3 years, we can reject the possibility of self-lensing at more than the 99% confidence level, according to Poisson statistics. In Table 3.4, we show some other results on how strongly we can discriminate between the two possible locations of the lensing objects based on Poisson statistics. It is possible that we may be able to constrain strongly the lens location based on the 3-year statistics of transit EAGLE events.

In conclusion, the study of EAGLE events is very effective for constraining the nature of lens objects. If an EAGLE search is made for a few years, we can form strong constraints on lens objects in microlensing events.

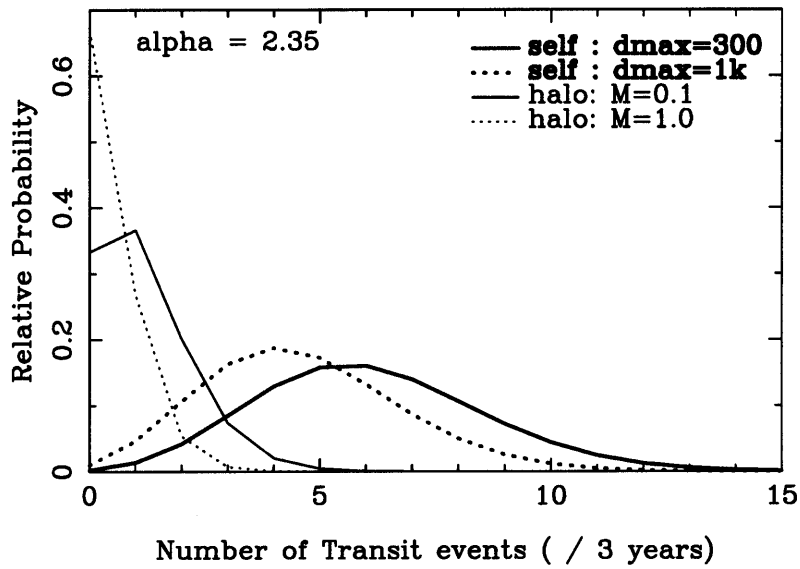

Figure 3.4: The probability distribution of the number of transit EAGLE events out of 21 EAGLE events in 3 years according to Poisson statistics for $\alpha = 2.35$, $V_{th} = 20$ and a detection efficiency of 50%. The bold solid and dashed curves correspond to self-lensing for $d_{max} = 300$ pc and 1 kpc respectively. The thin solid and dashed curves correspond to halo MACHOs with MACHO masses $M = 0.1M_{\odot}$ and $1.0M_{\odot}$ respectively. One can distinguish the lens population using the number of transit events.

Table 3.4: Confidence levels of rejecting each case

transit event (number)	halo ($M = 0.1M_{\odot}$)	halo ($M = 1M_{\odot}$)	self ($d_{max} = 300$ pc)	self ($d_{max} = 1$ kpc)
0	—	—	99.8	99.0
1	—	—	98.4	94.4
4	97.4	99.92	—	—
5	99.5	99.994	—	—
6	99.92	99.9996	—	—

Note: The values of confidence level of rejection are in % for each number of transit events detected in 3 years in case of $\alpha = 2.35$, $V_{th} = 20$ and a detection efficiency of 50%.

3.2 Constraining the Location of Microlensing Objects towards the LMC through Parallax Measurement in EAGLE Observations

We show that it is possible to determine whether microlensing objects towards the Large Magellanic Cloud (LMC) are in a dark Galactic heavy thick disk as several authors have suggested, or in the Galactic halo, with ground-based observations. Our method makes use of EAGLE events with parallax effect in which we are able to obtain the projected ("reduced") transverse velocity of the lens. If lens objects are in a dark Galactic heavy thick disk, it is easier to measure the parallax than in the halo because of their geometry. Furthermore, in EAGLE events, it is easier to observe the parallax than in normal microlensing events because of the high magnification. We first estimate the rate of EAGLE events. We find that the rate is comparable with or higher than that of normal microlensing events, even if events are caused by dark stars in the Galactic thick disk. We explore the possibility of measuring the parallax effect in EAGLE events towards the LMC by using two 2.5-m telescopes in two different continents. We show that the parallax effect can be measured in $40\% \sim 45\%$ of all EAGLE events if most lenses are stars in the Galactic thick disk, while $7\% \sim 9\%$ can be measured if most lenses are halo MACHOs. We conclude that the fraction of parallax-measurable EAGLE events amongst all EAGLE events is useful to discriminate between these two possibilities. An observational strategy for achieving this is discussed. In combination with the method suggested by Sumi & Honma (2000) to distinguish whether lenses are halo objects (MACHOs) or stars in the LMC, we are able to impose strong constraints on the location of lens objects and on the nature of the lenses.

3.2.1 Adopted Galactic Model and Relative Event Rate

In this section we give the adopted model of the Galaxy and the source stars, and discuss the relative event rate or the ratio of the EAGLE event rate to the normal event rate. Since only the relative event rate is discussed, common constant factors such as C, f, and the normalization of the luminosity function are not essential.

When we consider microlensing by lens objects in the maximal disk (these we call 'disk events'), we adopt an exponential disk as the mass density distribution for the Galactic thin and thick disk. Since the line of sight to the LMC is almost tangential to the azimuthal direction in the Galaxy, the mass density at the region efficient to microlensing is not strongly dependent on the Galactocentric radius r but only on the height from the disk plane z, as long as the disk scale height is much smaller than $r \simeq 8.5$ kpc. So we assume the disk density distribution only depends on z as

$$\rho(z) = \frac{\Sigma}{2h} \exp\left(-\frac{z}{h}\right), \tag{3.28}$$

where Σ is the local disk column density and h is the scale height of the disk. For the thin and thick disk we set $h_{\rm thin} = 350$ pc and $h_{\rm thick} = 1400$ pc respectively. A certain

acceptable value is $\Sigma_{\rm thin} \simeq 50 M_\odot {\rm pc}^{-2}$ (cf. Kuijken & Gilmore 1989). If we adopt this value, due to the maximal disk limit of $\sim 100 M_\odot {\rm pc}^{-2}$ estimated from the rotation speed of the Galaxy (Binney & Tremaine 1987) $\Sigma_{\rm thick} \simeq 50 M_\odot {\rm pc}^{-2}$ (Gilmore & Reid 1983; Gould 1994a; Gould, Miralda-Escude & Bahcall 1994). However, the value of the local column density for each disk is still controversial (cf. Kuijken & Gilmore 1989; Bahcall, Flynn & Gould 1992). So we take Σ as a model parameter assuming that the combined mass of the thin and thick disks does not exceed the maximal disk limit. We change the fraction of each component within this limit, i.e., $\Sigma_{\rm thin}(\Sigma_{\rm thick}) = 30(70), 50(50)$ and $70(30) M_\odot {\rm pc}^{-2}$.

For the disk events we assume the power-law mass function $\phi(M)$ of lens objects defined by equation (3.5) and (3.6) in section 3.1. And we use the number density of lens objects with the mass between M and $M + dM$ as $n_{\rm s}(M, x) dM = f \rho(\boldsymbol{r}(x)) \phi(M) dM/M$, where f is the mass fraction of the lens objects to the total mass and is assumed to be constant. We take the upper limit of mass $M_{\rm u} = 50 M_\odot$ and treat the lower limit $M_{\rm l}$ and the power-law index $\alpha_{\rm d}$ as model parameters as $M_{\rm l} = 0.1$ or $0.01 M_\odot$ and $\alpha_{\rm d} = 2.35$ or 5, i.e. we assume both the ordinary population of stars (Salpeter IMF) and darker population of stars as a constituent of the maximal disk. This $\alpha_{\rm d} = 5$ is the extreme case to be compared. As a result, our main results don't depend on this index much (see section 3.2.3). For the luminosity function of the source stars in the LMC $\phi_L(V)$, we follow equations (3.12) and (3.12) in section 3.1 with the IMF index $\alpha = \alpha_{\rm S} = 2.35$, which is consistent with the luminosity function of the LMC recently observed by using HST (Holtzman 1997).

When we discuss the lenses as halo MACHOs ('halo events'), we adopt the spherical 'standard' halo model following Alcock et al. (2000b) as given by equation (3.22). We also adopt the delta-function mass functions with $M = 0.1 M_\odot$ and $0.5 M_\odot$ because our knowledge about the lens mass function is very poor.

For the observational parameters we assume $V_{\rm obs} = 21$, which is a typical observational limit for current microlensing programs. We consider two different values for the threshold magnitude; $V_{\rm th} = 19$ and 20, where $V_{\rm th} = 20$ is more reasonable than the other.

Here we estimate the event rate of EAGLEs for disk events. We applied the formula for the event rate for normal microlensing events $\Gamma_{\rm N}$ and for EAGLE events $\Gamma_{\rm E}$ of equations (3.15) and (3.20) in section 3.1 respectively after fixing $D_s = 50$ kpc. We calculated the relative EAGLE event rate $\Gamma_{\rm E}/\Gamma_{\rm N}$ for disk events. In this calculation the finite source effect is also included following Sumi & Honma (2000). The results for $V_{\rm th} = 19$ and 20 are listed in Table 3.5. One can see that $\Gamma_{\rm E}/\Gamma_{\rm N}$ does not strongly depend on the disk structure parameters (Σ, h) and the mass function $\alpha_{\rm d}, M_{\rm l}$. This ratio depends on the luminosity function of source stars. We checked this ratio in the conservative case of gentler-slope $\alpha_{\rm S} = 2.0$ and $V_{\rm th} = 20$, and found this decreased the ratio to 1.35. This is still sufficiently high.

As a result the decrease of the EAGLE event rate due to finite source effects is negligible. Only in the most extreme case that $V_{\rm th} = 19$ and $\alpha_{\rm d} = 5.0$, this ratio is slightly decreased due to finite source effects. In the more reasonable case that $V_{\rm th} = 20$ and $\alpha_{\rm d} = 2.35$, we found that the finite source effect is not negligible only when $M_{\rm l} < 10^{-4}$. For halo events, the events affected by finite source effects is only several percent out of all EAGLE events

(Sumi & Honma 2000). So hereafter we neglect the finite source effect.

Table 3.5: The ratio of EAGLE event rate to normal event rate for disk events .

$V_{\rm th}$	$\alpha_{\rm d}$	the thin disk		the thick disk	
		$M_{\rm l} = 0.1M_\odot$	$M_{\rm l} = 0.01M_\odot$	$M_{\rm l} = 0.1M_\odot$	$M_{\rm l} = 0.01M_\odot$
19	2.35	0.73	0.72	0.73	0.73
19	5.0	0.73	0.72	0.73	0.73
20	2.35	1.83	1.83	1.83	1.83
20	5.0	1.83	1.83	1.83	1.83

3.2.2 Microlensing events with Parallax Effect

The fraction of parallax-measurable microlensing events depends on the position of the lens. If lens objects are in the thin or thick disk, the Einstein radius projected onto the observer plane from the source star, or "the reduced Einstein radius",

$$\tilde{R}_{\rm E}(M,x) \equiv \frac{R_{\rm E}(M,x)}{1-x} \propto \sqrt{\frac{x}{1-x}}, \tag{3.29}$$

is much smaller than that for halo events. Hence the light curve is more sensitive to the small displacement of the observer position in disk events. Therefore the fraction of parallax-measurable EAGLE events out of all EAGLE events for the disk events will be much larger than for halo events. This fraction is useful to discriminate statistically whether the lens objects are mainly in the thick disk or not.

We consider parallax measurements with two separate telescopes on the Earth. To be concrete we suppose the situation that the real-time detection and the alert for an microlensing event (both normal and EAGLE) is issued by a 1 m-class alert telescope and follow-up observations are performed by two 2.5 m-class telescopes, which are located on different continents. We can get two different light curves due to the displacement between the follow-up telescopes. In Figure 3.5 we show a schematic view of the geometry on the observer plane and the difference in the light curve. From the measurements of parallax between them we can extract additional information on the lens object, namely the "reduced transverse velocity" given as follows (Refsdal 1966; Gould 1992, 1994b, 1995b; Holz & Wald 1996)

$$\tilde{v} \equiv \frac{v_{\rm t}}{1-x}. \tag{3.30}$$

The reduced transverse velocity represents the projected relative transverse velocity between the source star and the lensing object and will be of great use in investigating the lens location because this value for each component (halo, thick disk, and thin disk) is different (about 240 $\rm kms^{-1}$, 50 $\rm kms^{-1}$ and 30 $\rm kms^{-1}$, respectively) and hence for disk events $\tilde{v}$ is ~ 8 times smaller than that for halo events.

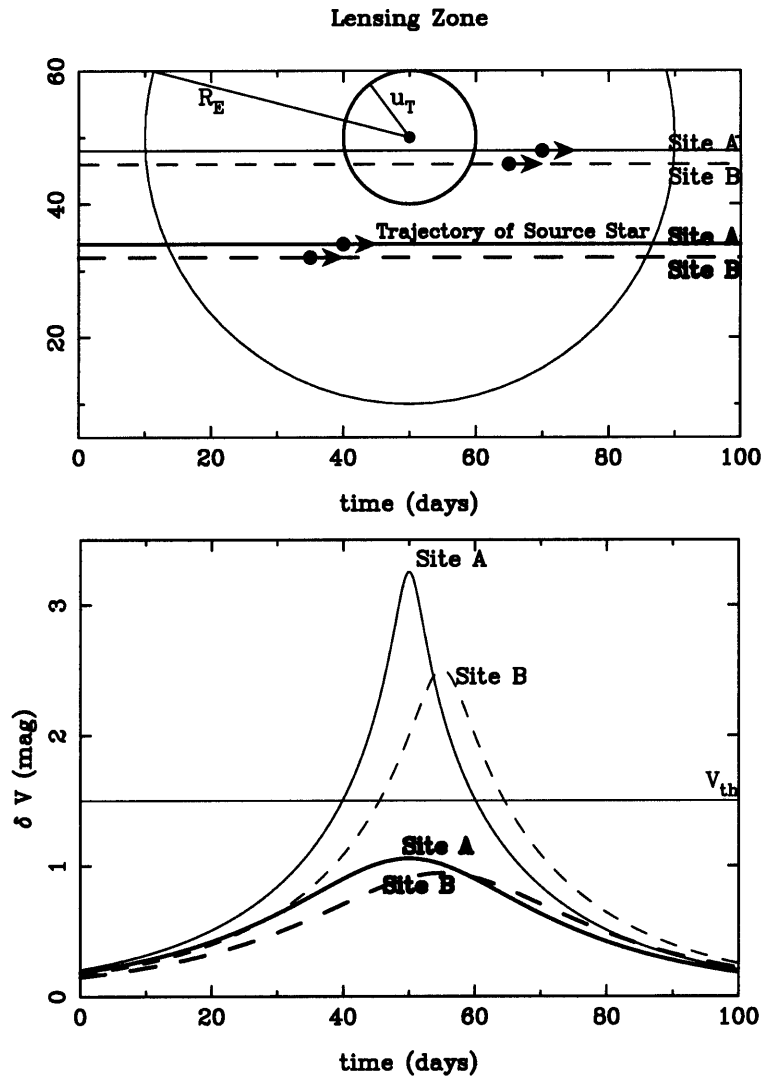

Figure 3.5: Top panel: A schematic view of the trajectory of a source star relative to the lens object of two microlensing events seen in two distant sites A and B. The source star is dim and invisible without magnification by microlensing. The outer thin circle and inner thick circle are the Einstein radius and the circle with $u = u_{\rm T} = 0.25$, respectively. An event is identified as an EAGLE event when the trajectory of the source goes along the thin straight lines such that u becomes smaller than $u_{\rm T}$, like the event represented by thin lines. The solid and dashed thin lines correspond to $\beta = 0.05$ and 0.1, respectively. If the trajectories are along bold lines, where the solid and the dashed lines are with $\beta = 0.4$ and 0.45, respectively, the event is not observed as an EAGLE event. Bottom panel: The corresponding light curves of EAGLE events seen in both sites. t_0 is observed as 50 and 55 days for sites A and B, respectively. The horizontal line denotes an example of the EAGLE detection threshold $V_{\rm th}$. In this example the event represented by the thin lines, which have $\beta < u_{\rm T}$, is magnified over $V_{\rm th}$ and is identified as an EAGLE event. The difference of peak magnification between two sites is much larger when the magnification is high (the thin lines) compared with the event with low magnification (the thick lines).

We list some basic formulae on parallax measurement following Holz & Wald (1996). In this section, β indicates the minimum impact parameter u_{min} for a convenience. We denote the difference of t_0 and β as δt_0 and $\delta\beta$, respectively, which are obtained by comparing light curves observed at both sites. These quantities are expressed by the transverse distance of two telescopes D and the angle θ between the direction of $\tilde{v}$ and the line joining the two telescopes on the lens plane as

$$\delta t_0 = \frac{D\cos\theta}{\tilde{v}}, \tag{3.31}$$

$$\delta\beta = \frac{D\sin\theta}{\tilde{R}_{\rm E}}. \tag{3.32}$$

Eliminating θ from equations (3.31) and (3.32), we obtain the reduced velocity of the lens object as follows

$$\tilde{v}^2 = \frac{D^2}{t_E^2\delta\beta^2 + \delta t_0^2}, \tag{3.33}$$

where we used $\tilde{R}_{\rm E}/\tilde{v} = R_{\rm E}/v_{\rm t} = t_E$. Since the quantities in the right-hand side of equation (3.33) are all observable, we can in principle determine $\tilde{v}$ of each event from observations. To be exact, the four-fold degeneracy in the determination of $\tilde{v}$ remains in parallax measurements with only two telescopes (Gould 1994b), although the degeneracy does not affect the main conclusion of this Chapter discussed in section 3.2.3 and 3.2.4, because of the short baseline D.

3.2.3 Fraction of Parallax-measurable events

In this section we calculate the fraction of parallax-measurable events in all events including normal and EAGLE events. It will be shown that the contribution to the fraction from EAGLE events is important to detect the parallax effect and to discriminate whether the location of the lens objects is in the Galactic disk or not. As the density model of the Galaxy we adopt the same model as introduced in section 3.2.1. The number of the parallax-measurable events depends on the photometric error as shown in Appendix A. Furthermore the estimation of the event rate requires the kinematics of lens objects. The typical (transverse) velocity of the lens objects is given in Appendix B

First we estimate the average of the ratio $\beta_{\rm crit}/u_{\rm T}$ for given V and discuss for which kind of source stars does the parallax effect tend to play a role in microlensing events. We define the differential ratio averaged over M and x as follows:

$$\frac{d\langle\beta_{\rm crit}/u_{\rm T}\rangle}{dV}(V) = \frac{1}{d\Gamma}\int_0^1 D_{\rm S}dx\int_{M_{\rm l}}^{M_{\rm u}} dM\,\frac{\beta_{\rm crit}(V,M,x,v_{\rm t}(z(x)))}{u_{\rm T}(V)}R_{\rm E}(M,x)\,n_{\rm s}(M,x), \tag{3.34}$$

where $d\Gamma$ is the integral of the weighting function;

$$d\Gamma = \int_0^1 D_{\rm S}dx\int_{M_{\rm l}}^{M_{\rm u}} dM\,R_{\rm E}(M,x)\,n_{\rm s}(M,x). \tag{3.35}$$

In Figure 3.6 we show $d\langle\beta_{\rm crit}/u_{\rm T}\rangle/dV$ as a function of V for disk events of the lens mass function with $M_{\rm l} = 0.1M_{\odot}$ and $\alpha_{\rm d}$ =2.35 or 5.0, and for halo events of the delta-function mass function with M =$0.1M_{\odot}$ and $0.5M_{\odot}$. For disk events the ratio for the thin disk and for the thick disk is separately shown. The left side of the vertical dashed line ($V = V_{\rm obs} = 21$) corresponds to normal events and the right side represents EAGLE events.

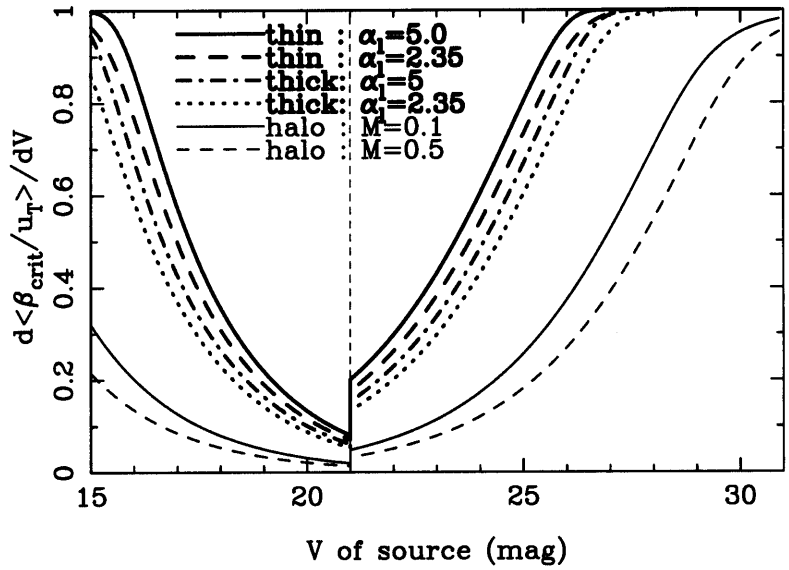

Figure 3.6: $d\langle\beta_{\rm crit}/u_{\rm T}\rangle/dV$ defined in equation (3.34) as a function of V, under the assumption described in the text. For disk events (thick lines) the slope of the lens mass function $\alpha_{\rm d}$ =2.35 and 5.0 with $M_l = 0.1M_{\odot}$, and for halo events (thin lines) the lens mass function is the delta-function with M =$0.1M_{\odot}$ and $0.5M_{\odot}$. The thick solid and dashed lines correspond to the thin disk with $\alpha_{\rm d} = 2.35, 5.0$, respectively. The bold dot-dashed and dot lines correspond to the thick disk with $\alpha_{\rm d} = 2.35, 5.0$, respectively. The thin solid and dashed lines correspond to halo events with mass of $M = 0.1M_{\odot}$ and $0.5M_{\odot}$, respectively, and with $v_t = 190\ {\rm km\,s^{-1}}$. The left side relative to the vertical dashed line represents normal microlensing events and the right side is for EAGLE events. For normal events, $\beta_{\rm crit}/u_{\rm T}$ is high for a bright source stars because of the large flux. For EAGLE events, $\beta_{\rm crit}/u_{\rm T}$ is large for faint source stars because of the high magnification. The gap at $V = 21$ is due to the difference in the detection criterion which requires $A \geq 1.34(u = 1)$ for normal events and $A \geq A_{\rm T}(V = 21) = 2.5$ for EAGLE events.

From Figure 3.6 we see that for normal events $\beta_{\rm crit}/u_{\rm T}$ is large for bright source stars because of the large flux, and gets smaller as the source stars get dimmer. For EAGLE events $\beta_{\rm crit}/u_{\rm T}$ is large for faint source stars because the magnification should be large for dark source stars. Note that the gap at $V = 21$ is due to the difference of the detection criterion, which requires $A \geq 1.34$ $(u = 1)$ for normal events and $A \geq A_{\rm th}(V = 21) = 2.5$ for EAGLE events.

Since the number of faint source stars is large, EAGLE observations have an advantage over normal microlensing observations for detecting the parallax effect. To make the dis-

cussion more accurate, we must see the relative parallax-measurable event rate weighted with the source luminosity function. The rate of microlensing events with the parallax effect is written as

$$\Gamma_{\rm P} = C \int_0^1 D_{\rm S} dx \int_{V_{\rm l}}^{\infty} \phi_{\rm S}(V)\, dV \int_{M_{\rm l}}^{M_{\rm u}} dM\, \beta_{\rm crit}(V, M, x, v_{\rm t}(z(x)))R_{\rm E}(M, x)\, n_{\rm s}(M, x). \quad (3.36)$$

where C is the dimensional constant common to the expression of $\Gamma_{\rm N}$ and $\Gamma_{\rm E}$ (Sumi & Honma 2000). $\beta_{\rm crit}$ for EAGLE events (equation (A.15)) is applied for $V > V_{\rm obs} = 21$ and one for normal events for $V < V_{\rm obs} = 21$.

In Figure 3.7 we show the relative differential event rate distribution of parallax-measurable events $d\Gamma_{\rm P}/dV$ normalized by $\Gamma_{\rm N}$ (for $V < V_{\rm obs}$) or $\Gamma_{\rm E}$ (for $V > V_{\rm obs}$) for disk and halo events, as a function of source magnitude V and for various combinations of $M_{\rm l}$ and $\alpha_{\rm d}$. The contributions from the thin and the thick disk are drawn separately for disk events. We also note that the absolute value of the vertical axis is not important because the event rate distributions shown are relative ones. These distributions are to be compared with the relative event rate distribution for all events (the bold dotted line). The left side relative to the vertical dashed line corresponds to normal microlensing events and the right side is for EAGLE events. For disk events the greater $\alpha_{\rm d}$ or the smaller $M_{\rm l}$, the higher is $d\Gamma_{\rm P}/dV$. From Figure 3.7 we see that for disk events the event rate of parallax-measurable EAGLE events ($V > 21$) is much higher than that of normal microlensing events ($V < 21$). We also see that for halo events the fraction of parallax-measurable events is quite low for both EAGLE and normal events.

We evaluated the ratio of the parallax-measurable EAGLE event rate to the parallax-measurable normal event rate $\Gamma_{\rm P}(V > V_{\rm obs})/\Gamma_{\rm P}(V < V_{\rm obs})$ in Table 3.6 for disk events and in Table 3.7 for halo events. From Table 3.6 and 3.7, it is clear that EAGLE events enlarge the opportunity of parallax measurements. The number of parallax-measurable EAGLE events is $7 \sim 9$ times larger than that of normal events for disk events. For halo events it is $13 \sim 14$ times larger than that in normal events, although the rate of parallax-measurable normal events is extremely low. From these tables we conclude that most of the parallax-measurable events are EAGLE events. We hereafter approximate the rate of parallax-measurable events as $\Gamma_{\rm P}$.

Table 3.6: The ratio of parallax-measurable EAGLE events to that in parallax-measurable normal events for disk events.

$\alpha_{\rm d}$	the thin disk		the thick disk	
	$M_{\rm l} = 0.1M_\odot$	$M_{\rm l} = 0.01M_\odot$	$M_{\rm l} = 0.1M_\odot$	$M_{\rm l} = 0.01M_\odot$
2.35	8.46	6.85	9.40	7.73
5.0	8.05	6.38	8.98	7.25

In Table 3.8 we show the fractions of parallax-measurable EAGLE events out of all EAGLE events $\Gamma_{\rm P}/\Gamma_{\rm E}$, and corresponding typical t_E values for disk events. For $\Sigma_{\rm thick}(\Sigma_{\rm thin}) =$

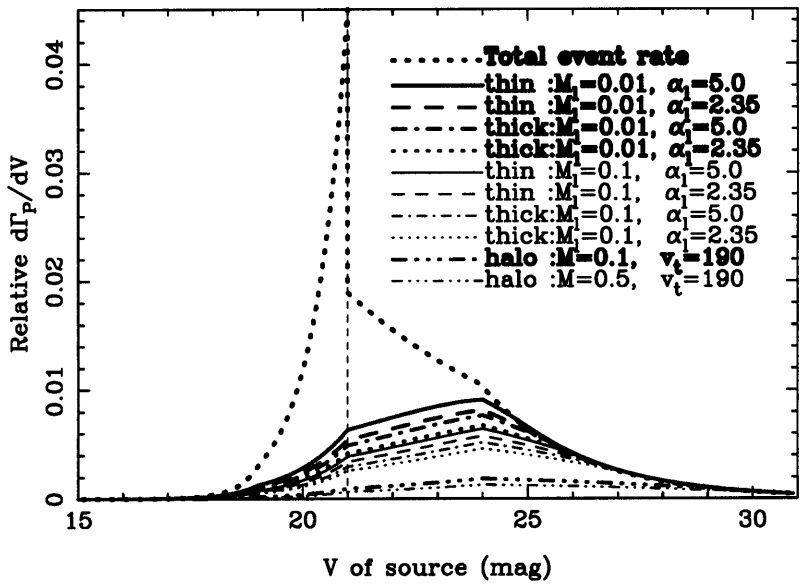

Figure 3.7: The relative differential event rate distribution of parallax-measurable events $d\Gamma_{\rm P}/dV$, normalized by $\Gamma_{\rm N}$ (for $V < V_{\rm obs}$) or $\Gamma_{\rm E}$ (for $V > V_{\rm obs}$), as a function of source magnitude V and for various combinations of $M_{\rm l}$ and $\alpha_{\rm d}$. The model parameters are the same as Figure 3.6. We note that the absolute value of the vertical axis is not important because the event rate distributions shown are relative ones. We also show the relative $d\Gamma_N/dV$ and $d\Gamma_E/dV$ by the bold dotted line. The left side of vertical dashed line is for normal microlensing events and the right side is for EAGLE events.

30(70), 50(50) and 70(30), the optical depths are 3.84(2.43), 6.41(1.74) and 8.97(1.04) in 10^{-8}, respectively, if $f = 1$, although the common factor f is not essential so long as relative the event rate is discussed, as noted in section 3.2.1. From Table 3.8, we see $\langle t_E \rangle$ be strongly affected by $M_{\rm l}$. $M_{\rm l} = 0.01 M_\odot$ looks like being consistent with the observed value $t_E \sim 40$ days (Alcock et al. 2000b) for the thick disk with $\alpha_{\rm d} = 2.35$. $\Gamma_{\rm P}/\Gamma_{\rm E}$ only weakly depends on $\Sigma_{\rm thin|thick}$ and $\alpha_{\rm d}$. We also show the fractions in the conservative case that the source star is $V < 25$ in parentheses in Table 3.8, because it might be difficult to detect the events with the dimmer ($V > 25$) source star as discussed in the following section. We conclude that parallax effect can be measured in more than 40% of EAGLE events if the lenses are stars in the thick disk.

The fractions for the thin disk are 10% larger than that for the thick disk. But the

Table 3.7: The ratio of parallax-measurable event in EAGLE events to that in normal events for halo events.

$v_{\rm t}$=190km s^{-1}		$v_{\rm t}$=220km s^{-1}	
$M = 0.1M_\odot$	$M = 0.5M_\odot$	$M = 0.1M_\odot$	$M = 0.5M_\odot$
12.6	13.7	12.8	13.9

Table 3.8: The fraction of parallax-measurable events in all EAGLE events for disk events.

α_d	Σ_{thick}	the thin disk				the thick disk			
	($M_\odot$ pc^{-2})	$M_l = 0.1M_\odot$		$M_l = 0.01M_\odot$		$M_l = 0.1M_\odot$		$M_l = 0.01M_\odot$	
		$\langle t_E \rangle$(d)	Γ_P/Γ_E	$\langle t_E \rangle$(d)	Γ_P/Γ_E	$\langle t_E \rangle$(d)	Γ_P/Γ_E	$\langle t_E \rangle$(d)	Γ_P/Γ_E
2.35	30	62.9	0.492	23.9	0.641	135.4	0.411	51.4	0.551
			(0.379)		(0.552)		(0.297)		(0.447)
2.35	50	56.5	0.478	21.4	0.626	127.1	0.401	48.2	0.540
			(0.365)		(0.534)		(0.287)		(0.434)
2.35	70	50.7	0.464	19.2	0.611	120.1	0.392	45.6	0.530
			(0.350)		(0.515)		(0.278)		(0.422)
5.0	30	42.2	0.537	13.4	0.701	90.8	0.451	28.7	0.609
5.0	50	37.9	0.521	12.0	0.686	85.3	0.440	27.0	0.598
5.0	70	34.0	0.506	10.8	0.670	80.6	0.430	25.5	0.587

Note: The fractions in the case that the source star is $V < 25$ are in parentheses. The event timescales $\langle t_E \rangle$ are given in day.

contribution of these components is small because the optical depth is about 25% relative to that of the thick disk, being consistent with previous estimations (Gould 1994a; Gould, Miralda-Escude & Bahcall 1994). M_l might be between 0.1 and 0.01 from comparing the event durations with the observed value $t_E \sim 40$ days. Anyway, the parallax effect can be measured in more than 40% of EAGLE events for the thin disk events.

For halo events, here we adopt the mass function as a delta function, a Gaussian distribution and a log-normal Gaussian distribution because our knowledge about the lens mass function is very poor. For the delta function we adopt $M = 0.1M_\odot$ and $0.5M_\odot$. For the Gaussian and log-normal Gaussian distributions we take the mean of the mass $M_{mean} = 0.1M_\odot$ and $0.5M_\odot$. The variance is $0.4M_\odot$ for the Gaussian distribution and $\log(0.4M_\odot/M_{mean})$ for the log-normal distribution. Of course the mass function is zero for negative M in the Gaussian distribution. The typical transverse velocity $v_t = 190$ km s^{-1} and 220 km s^{-1}. We estimated the fraction in the same way as above and the results are shown in Table 3.9. We also show the fractions in the case that the source star is $V < 25$ in parentheses in Table 3.9. The optical depth is 4.8×10^{-7} if $f = 1$. From Table 3.9, we see that the fraction of parallax-measurable events out of all EAGLE events is $7 \sim 9\%$.

We conclude that parallax effect can be measured by accurate photometric observations of EAGLE events and that we can statistically discriminate the location of the lens objects, whether they are in the thick disk or the halo, by estimating the relative parallax-measurable EAGLE event rate.

Table 3.9: The fraction of parallax-measurable events in all EAGLE events for halo events with various types of lens mass function.

M or $M_{\rm mean}$	$v_{\rm t} = 190$km s^{-1}		$v_{\rm t} = 220$km s^{-1}	
($M_\odot$)	$\langle t_E \rangle$(d)	$\Gamma_{\rm P}/\Gamma_{\rm E}$	$\langle t_E \rangle$(d)	$\Gamma_{\rm P}/\Gamma_{\rm E}$
the delta-function mass function with mass M				
0.1	22.4	0.190	19.4	0.180
		(0.111)		(0.104)
0.5	50.1	0.140	43.3	0.133
		(0.077)		(0.072)
the Gaussian mass function with mean mass $M_{\rm mean}$				
0.1	44.6	0.152	38.6	0.143
		(0.085)		(0.079)
0.5	52.5	0.141	45.3	0.133
		(0.078)		(0.072)
the log-normal mass function with mean mass $M_{\rm mean}$				
0.1	46.5	0.162	40.1	0.153
		(0.093)		(0.087)
0.5	51.1	0.140	44.1	0.132
		(0.077)		(0.072)

Note: The fractions in the case that the source star is $V < 25$ are in parentheses. The event timescales $\langle t_E \rangle$ are given in day.

3.2.4 Discussion on the Observation Strategy

We have seen that the EAGLE event rate is as high as that for normal events even for disk events towards the LMC. Since the period in which an EAGLE event is visible ($V < 21$) is usually short (1 day $\sim$ 40 days), the detection efficiency heavily depends on the observational frequency. The observational programs currently undertaken by most groups are not adequate. Hourly monitoring with a 1-m class dedicated telescope and the real-time detection of EAGLE events are required to issue alerts with a high detection efficiency. However, for the events in which the source star is $V > 25$ this period is less than 2 days, so some people might not believe the detection of this kind of events. So we estimated $\Gamma_{\rm E}/\Gamma_{\rm N}$ and $\Gamma_{\rm P}/\Gamma_{\rm E}$ in the case that the source star is $V < 25$. Then we found $\Gamma_{\rm E}/\Gamma_{\rm N} = 1.48$ with $V_{th} = 20$. And we showed $\Gamma_{\rm P}/\Gamma_{\rm E}$ for the disk and halo events in parentheses in Table 3.8 and 3.9 respectively. These are decreased but still sufficiently high. Of course, the larger alert telescopes make it easier and faster to issue the alerts.

Although monitoring with a 1-m class telescope is sufficient to issue alerts for EAGLE events, it does not have enough power to make accurate observations near the peak and the declining stage of the light curve below $V_{\rm th}$. Hence follow-up observations with at least two 2.5-m class telescopes must take over the observation of the event. In particular, around the

peak of the light curve highly frequent observations are necessary because $\delta t_0 \sim D/\tilde{v}$ ~50 minutes for disk events. Since for halo events δt_0 is much shorter than for disk events, δt_0 is quite hard to detect for halo events in actual observations. Inversely, the test for the existence of the shift of the peak amplification time due to the parallax effect may be just effective in constraining the location of the lens objects. Clearly, follow-up observation with a 2.5-m class telescope on the Earth and the Next Generation Space Telescope (NGST) would be a more attractive plan for the future to increase the baseline D and to improve the observation below $V_{\rm th}$ as discussed in Appendix A.

As shown in section 3.2.3, we can measure the parallax effect in a large fraction of EAGLE events. If alerts were issued for such EAGLE events, observations with a global network would allow the precise measurement of the light curve near the maximum amplification. Since $\tilde{v}$ for objects in the halo is $5 \sim 8$ times larger than that for stars in the disks, we can determine whether the lensing objects reside in the halo or disks.

The true source flux f_0 is needed to measure the precise value of β in the light curve fitting when the only light curve is only observed around the peak. However, f_0 can't be measured through DIA. Then follow-up observations by a high resolution telescope such as HST or VLTs are needed to get an accurate f_0 after the event.

In short, a reasonable and practical observational strategy would be to observe hourly with a 1-m telescope and perform real-time analysis with the DIA to issue alerts to world observatories for follow-up observation with 2.5-m class telescopes on two different continents. Then after the events follow-up observations should be made by HST or VLTs.

We estimated the fraction of parallax-measurable EAGLE events amongst all EAGLE events using two 2.5-m follow-up telescopes in different continents. We found that EAGLE events enlarge the opportunity of parallax measurements by $7 \sim 9$ times for disk events, and by $13 \sim 14$ times for halo events relative to that in normal microlensing events. We also found we can measure the parallax effect in $40 \sim 45\%$ of EAGLE events if the lenses are in thick disk, and in 7~9% if the lenses are in the halo. The fraction of parallax events whose $\tilde{v}$'s are measured with more than 50% accuracy depends on the lens location as discussed in section 3.2.3.

To demonstrate this more specifically we estimate the number of expected parallax-measurable events for two cases that these are mainly halo events or disk events. In both cases, the thin disk, which is not essential due to its small contribution, is included. For the typical parameters $\alpha_{\rm S} = \alpha_{\rm d} = 2.35$, $\Sigma_{\rm thin} = \Sigma_{\rm thick} = 50 M_\odot {\rm pc}^{-2}$, $V_{\rm th} = 20$, the detection efficiency of 50% and the source stars should be $V < 25$, one can expect to find $\simeq$13 EAGLE events after a 3-year observation period of 11 square degrees of the LMC central region (as the MACHO collaboration does). In these 13 EAGLE events, 2 events (15%) are due to the stars in the thin disk and a further 11 events are due to MACHOs or the dark stars in the thick disk. In considering these 11 events, the reasonable parameters are $M = 0.1$ or $0.5 M_\odot$ except $M = 0.1 M_\odot$ in the case of the δ-function for halo events, and $M_{\rm l} = 0.01 M_\odot$ for disk events, to be consistent with $\langle t_E \rangle \simeq$40 days (Alcock et al. 2000b). In this case, we will be able to measure $\tilde{v}$ in respectively 6 and 2 events for disk events and for halo events, which include 1 thin disk event. We conclude that we would be able to

constrain the lens location strongly based on the 3-year statistics of EAGLE events with the parallax effect.

In conclusion, an accurate photometric study of EAGLE events would be effective in elucidating the location of lens objects. One could statistically discriminate whether the typical lens locations is in a thick disk or not, even with an effective baseline $\sim$ 6000 km as shown in this section. Additionally one could distinguish whether the lenses are MACHOs or stars in the LMC itself through measurements of finite-source effects in EAGLE events (Sumi & Honma 2000). Therefore one could identify lens objects as halo MACHOs, dark stars in the Galactic thick disk, or stars in the LMC through these observations.

Chapter 4

Experiment

From this Chapter in this thesis we describe the analysis of MOA Galactic Bulge data in 2000. This analysis is aimed to check how efficiently we can detect the EAGLE-type high magnification events, and to estimate the optical depth towards the GB, which give us information of the structure of the Galactic Bulge.

In this Chapter we discuss the observing instruments, site and strategy.

4.1 Site

We are observing at Mt.John University Observatory (MJUO) in New Zealand at 170°27.9′E, 43°59.2′S, 1030 m altitude. Typical sky background values are 21.9, 22.6, 21.5, 20.9 and 19.1 magnitudes per square arc second in the U, B, V, Rc and Ic passbands, respectively at an air mass of 1.0, and 21.7, 22.1, 20.8, 20.3 and 18.6 at an an air mass of 2.7 (Gilmore, private communication, 1994). Spectroscopic hours are approximately 45%. The seeing is typically in the rage $1.0 - 2.5$ arc seconds, and the global seeing of the entire set-up is typically $1.9 - 3.5$ arc seconds.

The telescope is a standard Boller and Chivens 61-cm aperture Richey-Chretien Cassegrain reflector. The focal ratio was previously F/13.5 and changed to F/6.25 with a new spherical secondary mirror and a three-lens field corrector added to the original hyperboloid primary mirror to provide a flat diffraction limited field of 85 mm diameter (Pennycook 1996). All the data used in this thesis were obtained by the F/6.25 system. This telescope is being operated semi-automatically under the program "TELJOY" (Williams 1996).

4.2 Camera

The camera equipped on this telescope is the large mosaic CCD camera MOA-cam2 (Yanagisawa 2000). This camera has three 2048×4096 pixels SITe thinned back-illuminated CCD chips (ST-002A) which have a very high quantum efficiency (QE) (nearly 80% in the region of the wavelength 500 to 800 nm as shown in Figure 4.1) and three buttable sides. The size of each chip is 3×6 cm and each pixel size is 15μm. The combined field of view of this

camera and telescope is $0.92° \times 1.39°$ (0.81 arcsec/pixel). This camera has a liquid nitrogen tank (ND5) with $1.2L$ capacity, manufactured by Infrared Laboratories and is operated at a cold temperature ($\sim -100°C$).

We are using MFront (Mosaic CCD Front-end Electronics) for the electronics which was developed by Subaru CCD development group. We also use Messia3 (Modularized expandable system for image acquisition (Sekiguchi 1998)) as the CCD controller, data acquisition and shutter control system, which is controlled by the work station (SPARC2). We show the characteristics of the transparency of the filters in Figure 4.2. We use 2 non-standard wide passband filters (Red and Blue) which are 13 cm $\times$13 cm area and $10mm$ thick. The shutter is located between the filters. The whole system slides sideways for observation in each color via a stepping motor which is controlled by the Messia3. The specifications of the telescope and camera are summarized in Table 4.1.

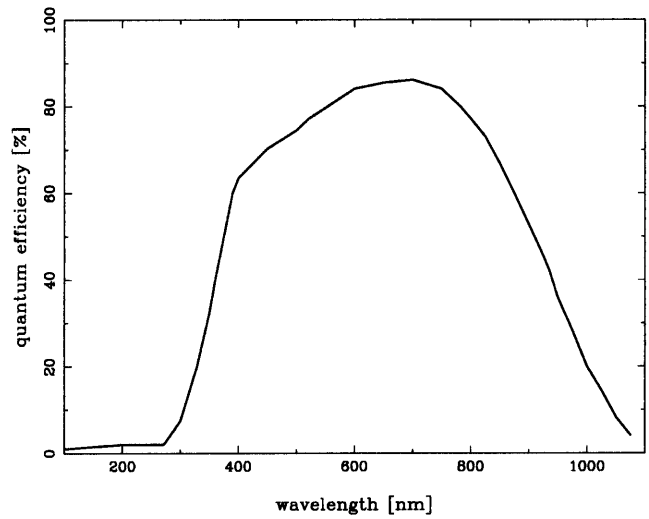

Figure 4.1: The quantum efficiency of SITe CCD

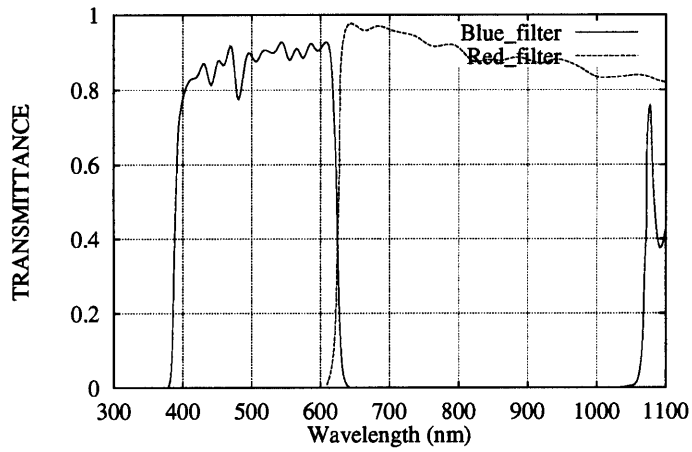

Figure 4.2: The passbands of the filters

Table 4.1: The specification of the site, telescope and camera.

Mt.John University Observatory	
place	170°27.9′E, 43°59.2′S
altitude	1030 m
seeing	1.9 – 3.5 arcsec
B & C telescope	
aperture	61 cm
focal ratio	F/6.25
MOA-cam2	
array size	1 × 3 CCDs (2048 × 4096 pixels)
pixel size	15 μm × 15 μm
effective area	61.44 mm × 92.16 mm
field of view	0.92°× 1.39° with B & C telescope
pixel scale	0.81 arcsec/pixel
LN_2 tank	Infrared Laboratories ND5 (1.2l)
LN_2 holding time	12.5 hours
operating temp	~ -100°C
weight	40 kg
filter	Red(630 – 1100 nm), Blue(400 – 630 nm)

4.3 Observation Strategy

We are observing 16 fields (20 deg^2) in the LMC a few times per day throughout the full year to search for MACHOs and to study variable stars with 2 color filters, where each field consists of three subfields corresponding to each CCD chip.

On the other hand, we observe 14 fields (18 deg^2) in the GB 5 $\sim$ 6 times per day only during the southern winter season (the GB is visible from April to November at MJUO) with the Red filter only. The main aim of the survey towards the GB is detecting the high magnification events ($A > 10$) in order to find extrasolar planets. The detection probability of extrasolar planets in the microlensing event is very low (a few %), but in high magnification events, this probability turns out to be very high (see section 2.5).

EAGLE events are usually high magnification. However the duration of EAGLEs is very short because these events are visible only during the peak of the magnification. To detect this kind of events we are sampling each field 5 $\sim$ 6 times a day with only the Red filter instead of both colors. Due to this high sampling rate, the detection efficiency for short time scale events becomes higher than the former study made by other microlensing survey groups. And it is a unique point of our observations to detect the small lens objects towards the GB. We show our 14 GB fields in Figure 4.3 and Table 4.2.

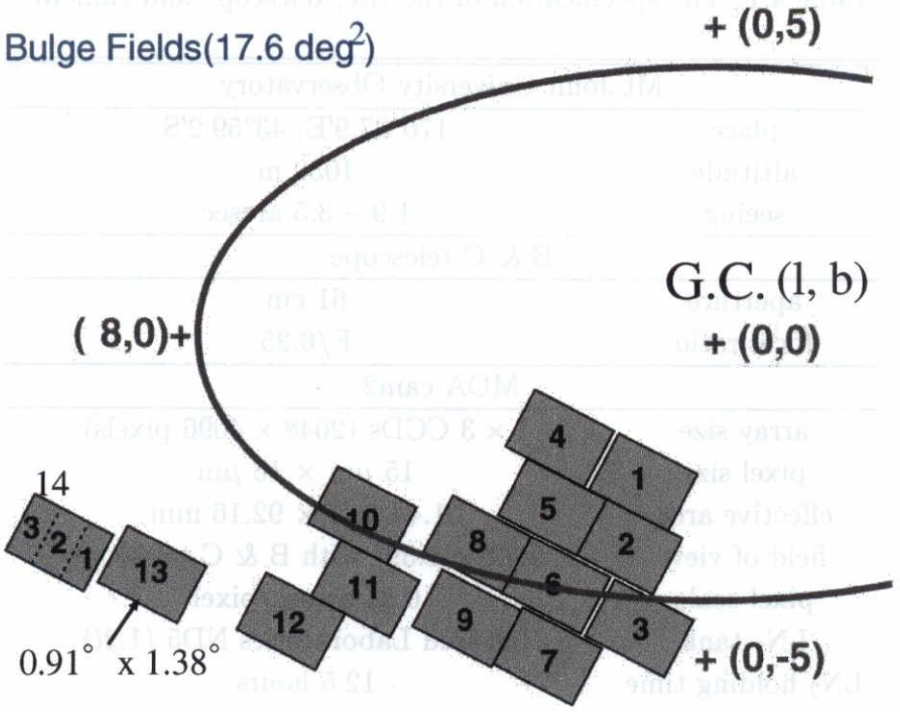

Figure 4.3: MOA Galactic Bulge fields.

Table 4.2: MOA Galactic Bulge fields. Positions are the center of the middle CCD (chip2).

field	RA (J2000)	Dec (J2000)	$l(°)$	$b(°)$
ngb1	17 56 24.4	-29 18 48	1.225443	-2.820797
ngb2	18 01 03.9	-29 48 48	1.294419	-3.948334
ngb3	18 05 35.5	-30 30 00	1.171821	-5.137455
ngb4	17 56 24.4	-27 50 00	2.507324	-2.079037
ngb5	18 01 03.9	-28 20 48	2.573193	-3.225651
ngb6	18 05 35.5	-28 59 32	2.495693	-4.407446
ngb7	18 10 23.7	-29 25 10	2.625283	-5.531947
ngb8	18 05 30.2	-27 34 18	3.731051	-3.700416
ngb9	18 10 54.8	-28 00 35	3.924187	-4.959934
ngb10	18 08 10.0	-25 50 00	5.543167	-3.377416
ngb11	18 12 34.3	-26 23 06	5.533736	-4.509716
ngb12	18 16 48.9	-25 40 59	6.606907	-5.017195
ngb13	18 18 00.0	-23 20 27	8.807236	-4.152192
ngb14	18 19 00.0	-21 50 08	10.247009	-3.646437

Chapter 5

DATA Analysis

Here we present the methods of data analysis which are used in this paper. We applied Difference Image Analysis (DIA) to Galactic bulge images taken by MOA during 2000 season (from April to November) instead of DoPHOT (Schechter, Mateo & Saha 1993) analysis. Until now a number of groups followed up the proposal of Paczyński (1986). Over the past years more than one hundred microlensing events have been discovered by the MACHO (Alcock et al. 2000b), EROS (Afonso et al. 1998, 1999), DUO (Alard & Guibert 1997) and OGLE (Udalski et al. 1994) collaborations. The standard way used in their analysis of CCD images was DoPHOT analysis, which performs the PSF fitting for each star on the image. In this analysis, the photometries are performed at the positions of stars in the catalogue which have been registered using good images. So, the events, whose baseline of source stars are dimmer than the observational threshold magnitude and not resolved on the catalogue image, could not be detected in this analysis. Furthermore this type of analysis suffers from the contamination of the flux measurements by "blending" of neighboring stars because the observational fields are usually very stellar dense fields to increase the number of source stars in microlensing experiments. This blending effect makes photometry worse and it impossible to know the real flux of the source star as discussed in section 2.3.1. The aim of changing to DIA from DoPHOT is to increase the sensitivity to the detection of gravitational microlensing events. We discuss how the DIA simplifies the process of detecting the events by detecting only objects whose flux was changed.

5.1 Data Preparation

All the data which are used in this paper are 273 sequences (numbered B273 $\sim$ B545) of 14 fields of the Galactic bulge, which contain $\sim 7,000$ images. In addition to this we took dark images every night and flat-field images every week. These data were saved to DLT tapes and brought back to Japan. At first, the cosmic ray and hot pixel in the dark and flat images are rejected by taking the median of 3 images of each night. And then this median dark image is subtracted from the raw star image of each field. The science images are made by dividing the dark subtracted star image by a normalized flat fielding image to

correct for the response of each CCD pixel.

5.2 Difference Image Analysis

Crotts (1992) and Phillips & Davis (1995) developed the "Difference Image Analysis (DIA)", or "Image subtraction method", and there have been a number of applications of DIA type techniques (Tomany & Crotts 1996; Reiss et al. 1998; Alard & Lupton 1998; Alard 2000; Alcock et al. 1999b, 2000a; Woźniak 2000; Bond et al. 2001). In brief, at first, one registers the star position, and geometrically aligns each "current" observation image to a preselected "reference" image which is recorded in good seeing, high signal-to-noise ratio (S/N) and low airmass. Next, the convolution kernel which is required to map the reference image to the current image, is calculated by using these current and reference images. The reference images are convolved to match the seeing and scale to aligned current images. The resultant, convolved images are then differentiated and variable objects are detected.

There are two different approaches in modeling and solving for the convolution kernel. One matches PSF models on the two images by solving for the kernel in Fourier space (Phillips & Davis 1995; Tomany & Crotts 1996). This approach was adopted by Alcock et al. (1999b, 2000a) in their reanalysis of a subset of the MACHO data.

The other is to directly model the kernel in real space (Alard & Lupton 1998). This method is suitable even for crowded and poor S/N images. So we developed our own implementation of this method. This includes the modification of Alard (2000) that models spatial variations of the kernel across the CCD.

Our implementation of the kernel solution method along with the subsequent image subtraction is mostly coded in C++. And we use some tasks of IRAF (Image Reduction and Analysis Facility) in this analysis.

5.2.1 Reference image

We selected the best seeing, higher S/N and low airmass images from full images taken in the 2000 season as the reference image for each field. The low airmass is required because these images must not be affected by differential refraction. The angle of refraction of light by the atmosphere depend on its wavelength. The first mention of the deleterious effects of atmospheric refraction on subtracted images was made by Tomany & Crotts (1996). They note that, for broad-band filters, the centroid position of a star is dependent upon the airmass of the observation. The phenomenon is well known in astrometry and gives an effect of increasingly elongating the PSF with airmass. For observations taken at different airmasses this leads to poor subtraction, giving a combined positive and negative profile, and systematic spurious detection. The presence of this effect is revealed by a significant residual flux remaining in the subtracted image. Alcock et al. (1999b) corrected this effect in their analysis. We found this effect is greater in our images with the Blue filter (see section 5.3). However, in our images with the Red filter, this effect is negligible when the airmass is lower than 2.0. So we didn't correct this effect because our data are mainly

taken through the Red filter, although, we required low airmass for reference images. The typical seeing of the selected reference images is $\sim 2.0''$, and the airmass is lower than 1.1.

In solving the kernel, we use a number of sub-regions, referred to as "stamp", centered on bright but not saturated stars, throughout the image. We chose about 450 stamps for each chip in the reference image. An advantage of this method of solution is that these stamps need not be centered on isolated stars with clear PSF (PSF stars). PSF stars are required in the another method using the Fourier transform. It's not easy to find enough PSF stars in our images, which are in very crowded regions and have poor seeing. So our method is suitable for our data because there can be any number of stars to any degree of crowding within a stamp. However we require that regions enclosed by the stamps, plus an additional margin given by half the kernel size, are completely free of bad pixels including dead columns and bleeding columns due to nearby saturated stars. Imposing this condition greatly improves the robustness in obtaining good quality subtracted images. The reference images are fixed over the entire time series observations of a given field, and stamps used for the kernel solution are also fixed over the time series.

The list of the positions of stars on the reference image are made, which is used in aligning the current images to the reference image. A mask image mapping the distribution of saturated stars was also formed from the reference image. If a particular star contained saturated pixels, the entire star profile (around 5 pixels centered on the saturated star) was masked out. The mask was applied to all subtracted images to obtain final images.

We made the catalogue of all stars in the reference images by using the DoPHOT program. Where all saturated stars on the reference images were masked with the corresponding mask image, and the edges of the CCD ($x < 35, x > 2042, y < 4$, and $y > 4090$ pixel) were cut in full off this analysis because of bad quality. These star catalogues are useful to select constant stars in section 5.4.1 and to calibrate the flux of our data to standard I and V band magnitudes in section 5.5. These are also used to make the extinction map of our observation fields from the Color Magnitude Diagram (CMD) in Chapter 7 and the luminosity function of MOA fields in section 8.1. Furthermore, the number of stars in each field is counted in this catalogue when we estimate the optical depth in section 8.4.

5.2.2 Image registration and alignment

Accurate registration of star position is important in DIA. The shift of star position makes significant residuals in the subtracted images. The list of the positions of 8800 bright stars on each current image is made by our original routine which is based on the IRAF task "daofind".

This routine finds the peak of the excess in the image. The small image around this peak is integrated to 1 dimension (x or y) and 1 dimensional Gaussian fitting would be performed for each x and y direction separately. From this fitting the center and height of the Gaussian are obtained. To be identified as a star, the roundness $2(h_x - h_y)/((h_x + h_y)$ is required to be between -1 and 1, where h_x and h_y are the heights of the Gaussian for each direction. We found the accuracy of this center position is enough for our analysis in

all cases.

This star list of current images is cross-referenced to that of the reference image, and the matched star list is made. To do this we divided one chip image into 8 sub frames and 100 bright stars in each sub frame were matched at first, and finally all 8800 stars are matched by using smart algorithm. A slower but very robust alternative algorithm was used as a backup if necessary. This combination of algorithms make the matching process robust for images taken in various conditions. Using this matched star list, a transformation matrix is made and the current image is aligned to the reference image by IRAF tasks "geomap" and "geotran". In this transformation the distortions of the image are not treated, because we found this effect is negligible in our images. The use of a large number of stars allowed us to determine an accurate mapping between the two images.

5.2.3 Image Subtraction method

The shape of the PSF of two images taken at different times is never exactly the same. The differences are due to the difference of the seeing, the sky level, and the extinction by the atmosphere. To match the PSF we degrade the reference image's seeing to match that of the current image. The PSF matching process is based on the fact that it is theoretically possible to match the profiles of stars observed under two different conditions, with a simple convolution of the form given by the following equation.

$$i(x,y) = r(x,y) * k(x,y) + b(x,y), \tag{5.1}$$

where r and i characterize the flux distribution of stars in the good seeing image and in the poor seeing current image respectively. The convolution kernel k encodes the seeing differences and b represents the sky background differences between the two images. Here the important point is that most of the stars on a given frame do not have large amplitude variations. Solving for the convolution kernel is the crucial step in the image subtraction. We follow the method of Alard (2000) as described previously.

Here we summarize our implementation. In principle, solving this equation is a nonlinear problem. An important consideration is that if we decompose our kernel function using some basis of functions, the problem becomes a standard linear least-squares problem. The convolution kernel function at a given location (x_0, y_0) is expressed as a linear combination of analytical "basis" functions

$$k(x_0,y_0,x,y) = a_0 f_0(x,y) + \sum_{m}^{N_{gauss}} \sum_{n}^{N_{pol}(m)} a_{mn}(x_0,y_0) f_{mn}(x,y). \tag{5.2}$$

The coefficients a in the linear combination are spatially dependent except a_0. They are also modeled as a linear combination of basis functions which takes the form of a two-dimensional polynomial written as

$$a_{mn}(x_0,y_0) = \sum_{s}^{N_{sp}} a_{mns} x_0^{p_s} y_0^{q_s}, \tag{5.3}$$

where the polynomial indices p_s and q_s depend on the function index s, which satisfy $0 \leq p_s \leq D_{sp}$ and $0 \leq p_s + q_s \leq D_{sp}$. D_{sp} is the degree of the polynomial corresponding to the spatial variation coefficients. There are a total of $N_{sp} = (D_{sp}+1)(D_{sp}+2)/2$ terms for each value of mn. The basis functions used to model the kernel take the form of a combination of two-dimensional Gaussian functions and polynomials written as

$$f_{mn}(x,y) = e^{-(x^2+y^2)/2\sigma_m^2} x^{p_n} y^{q_n}, \tag{5.4}$$

where $0 \leq p_n \leq D_m$ and $0 \leq p_n + q_n \leq D_m$. D_m is the degree of the polynomial corresponding to the Gaussian component with an index of m which is associated with σ_m. There are a total of $N_{pol}(m) = (D_m+1)(D_m+2)/2$ terms for each value of m and a total of $N_{base} = \sum_m^{N_{gauss}} N_{pol}(m)$ terms altogether.

The function $f_{mn}(x,y)$ (equation (5.4)) can be expressed in such a way as to make the integral of each zero except for the first basis function. Consequently the integral of the kernel itself is constant across the chip regardless of the spatial variations of the kernel. The coefficient of the first basis function a_0 will be the scale factor of this convolution kernel function.

The differential background $b(x,y)$ is also modeled as a linear combination of a two-dimensional polynomial written as

$$b(x,y) = \sum_i^{N_{bkg}} b_i x^{p_i} y^{q_i}, \tag{5.5}$$

where the polynomial indices p_i and q_i which satisfy $0 \leq p_i \leq D_{bkg}$ and $0 \leq p_i + q_i \leq D_{bkg}$. D_{bkg} is the degree of the polynomial corresponding to the differential background. There are a total of $N_{bkg} = (D_{bkg}+1)(D_{bkg}+2)/2$ functions.

The size of the kernel is selected as 17×17 pixels. We set the number of Gaussians $N_{gauss} = 3$. And we also set $D_{sp} = 2$ and $D_{bkg} = 2$. And we choose $\sigma_{0,1,2} = 0.7, 1.0, 1.3$ and the degrees of the polynomial are $D_{pol}(0,1,2) = 6,0,4$ respectively during the 2000 season. Then a total number of coefficients of the kernel function is $N_{kernel} = 1 + (N_{base}-1)N_{sp} + N_{bkg} = 265$. From 2001, we changed these values to $\sigma_{1,2,3} = 0.7, 1.3, 2.1$ and the degrees are $D_{1,2,3} = 6,4,2$ respectively, which corresponds to $N_{kernel} = 295$. These parameters were chosen empirically.

The solution for the coefficients a_{mns} and b_i could be found using standard linear techniques. We divided the reference and current image into eight 1k $\times$ 1k pixels sub-frames which were small enough to allow the spatial variations in the kernel and differential background to be satisfactorily modeled using smooth functions. We solve equation (5.1) by using $\sim$ 50 stamps which are enclosed by 23×23 pixels for each of the sub-frames. The corresponding subtracted image was then formed using following relation

$$\Delta i(x,y) = i(x,y) - r(x,y) * k(x,y) - b(x,y). \tag{5.6}$$

In these subtracted images, there are differences in the transmission coming from airmass, cloud coverage and dust extinction. This subtracted image $\Delta i(x,y)$ was rescaled

to match to the scale in the reference image by dividing with first coefficient a_0. By this process, all the time series of subtracted images are photometricaly calibrated without photometering the isolated high S/N stars. In this way no other correction was required for differences of the transmission with airmass. We show the real images before the subtraction (left) and after the subtraction (right) in Figure 5.1. We can see variable stars as the positive (white) and negative (black) residuals in the subtracted image. And the saturated star which can be seen at the top-left in images would be masked at the process to detect variable objects.

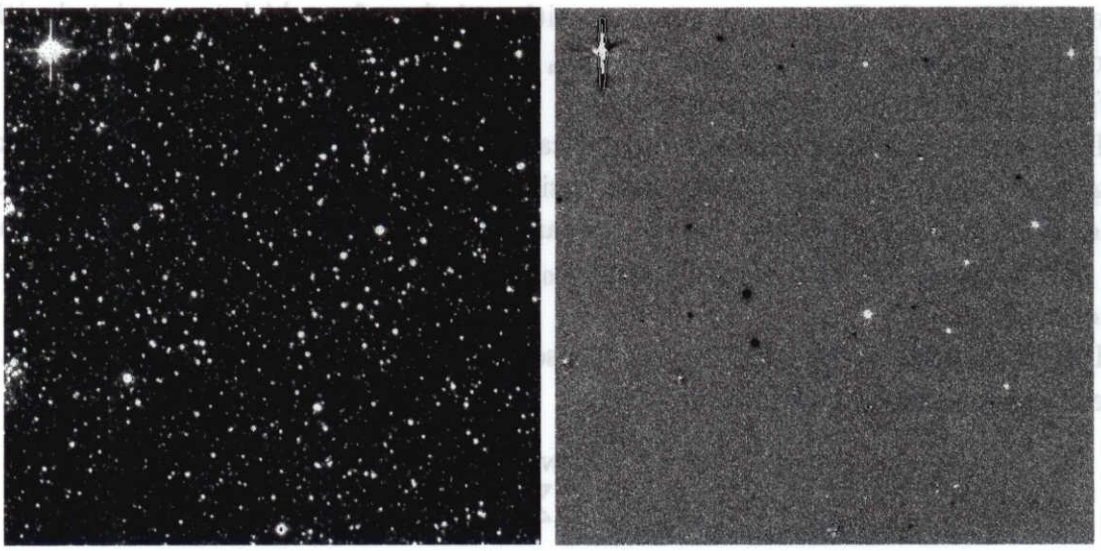

Figure 5.1: The image before the subtraction (left) and after the subtraction (right). The positive (white) and negative (black) points are variable stars in the subtracted image. The saturated star which can be seen at the top-left in images would be masked in the variable object detection process. These images are 512×512 pixels.

It is known that the PSF profiles vary across the field for large CCD images such as ours. Consequently, the possible spatial variation of the convolution kernel is an important consideration. The approach adopted by the MACHO collaboration was to divide their images into small sub-frames (500×500 pixels) and solve for the convolution kernel separately on each of these sub-frames assuming no significant variations in the kernel occurred on their length scales (Alcock et al. 1999b). However, for our images, we find small but significant spatial variations of the kernel even over small 500×500 pixels sub-frames. This prompted us to select the direct kernel modeling method which can easily model these spatial variations.

Furthermore we chose the direct kernel modeling method because the PSF matching method requires high S/N empirical PSF models on both the reference and current observation images by using a number of isolated PSF stars. This is difficult to achieve by using a small telescope such as ours at a site with only moderately good seeing. Meanwhile, the direct kernel modeling method only requires the reference images to be high S/N.

5.3 Identification of Variable objects

The fully matched images were differentiated to reveal variable objects whose flux has varied in some way between observations. At the position of variable objects on a given subtracted image, positive or negative profiles can be seen depending on whether the flux had increased or decreased relative to the reference image (see Figure 5.1). To detect these objects, we use the modified version of the star finding algorithm used in the star registration process (see section 5.2.2). With this algorithm, both positive and negative profiles could be detected simultaneously. There are also spurious profiles not associated with stellar variability, for example, cosmic ray, satellite track and the leaked electron from a too bright saturated star. Another type of spurious profile arose from the effects of a differential refraction as described in section 5.2.1. The shift of the star position caused by different airmass give a combined positive and negative profile, and a systematic spurious detection. This effect depends on the color of each star and airmass, and becomes especially serious in our Blue images. We show a Blue subtracted image which has suffered from this effect in Figure 5.2. This effect is not so serious for our Red images but can still be substantial occasionally.

Figure 5.2: The subtracted image with the effect of differential refraction. Both the positive (white) and negative (black) residuals in each star are caused by the shift of the centroid of the stars due to differential refraction. This image is 256 × 256 pixels.

To avoid detecting these spurious objects, we applied some criteria to the Analog Digital Unit (ADU) value of pixels within 4 pixels around the peak. The number of bad pixels whose ADU value is zero within 4 pixels from the peak should be less than 3. And 96% of the pixels within a 5 × 5 pixels box centered on the peak should have the same sign as the ADU value of the peak pixel. Finally the statistical significance of the flux within a 5 pixels box centered on the peak compared with the noise around this box, should be

larger than 3.0. This noise in the subtracted image comes from the various components, i.e., photon noise, readout noise and systematic noise. The photon noise is come from the source stars, the blended stars and the sky background. The systematic noise comes from poor subtraction due to the low S/N. The photon noise of the current image dominates for faint objects whereas for brighter objects the systematic noise from the image subtraction becomes important.

This routine was applied to the subtracted images to produce an initial list of variable object positions. Candidate objects which pass this selection were then checked against those obtained in previous reductions of the field. If no object is cross-referenced, these new objects were added to the database of object positions. If an object has previously been detected, this was identified as the same object and the number of detections for this object was incremented. The number of detections for each object were used in the event selection cut "cut1" (see section 6.1.1). The position was revised if the significance of the new detection would be greater than previous one. Then the list of positions of variable objects was made.

5.4 Photometry

Before performing the photometry for the objects in the list of variable objects made in the previous section, we applied the first simple event selection "cut1" (see section 6.1.1) because there are a number of spurious detections in this list.

For the objects which passed the "cut1", we perform both aperture and PSF profile fitting photometry. These positions are independent on whether the source star is isolated at this position in the reference image or not. This differs from the traditional approach which has been to follow up only stars detected in the template (reference) image by the DoPHOT type algorithm. This change gives us greater sensitivity to detect microlensing events whose source star is either too faint or too blended to be resolved in the reference image. This effectively enlarges the search area and the number of monitored source stars.

Aperture photometry and its noise are given by

$$a_{ap} = \sum_i \Delta f_i, \tag{5.7}$$

$$\sigma_{ap}^2 = \sum_i \sigma_i^2, \tag{5.8}$$

$$\sigma_i^2 = \frac{f_i G}{a_0}, \tag{5.9}$$

where Δf_i is the differential flux in pixel i, f_i is the actual flux of the pixel including the background sky and stars in the current image before subtraction of the reference image. The sum is over pixels within the 6-pixel radius from the centroid.

In estimating the noise of each pixel σ_i of the subtracted image in equation (5.9), we should take care of the gain G in ADU/e^- and the scale factor a_0 of each frame. The

scale factor a_0 is the first coefficient of the kernel function of the frame. The flux in all subtracted images are scaled to match the reference image in ADU value (see section 5.2.3). The number of photo-electrons in the current image is given by $f_i a_0/G$. So the noise associated with this pixel is $\sqrt{f_i a_0/G}$, and this was rescaled back to the reference image in ADU by multiplying by G/a_0.

For the PSF profile fitting, the high S/N empirical PSF images (23 × 23 pixels) were made for each of the 32 (500 × 500 pixels) sub-regions in the reference image by using bright and isolated stars in each sub-region. Then these PSF images are convolved by the same kernel function that is used in the image subtraction process, to match this PSF to that in each local position of each time series of frames. And the total flux of this PSF is normalized to 1.

The PSF profile photometry comes down to a two-parameter fit for the amplitude a_{psf} and base line b with

$$\chi^2 = \sum_i \frac{a_{psf} P_i + b - \Delta f_i}{\sigma_i^2}, \tag{5.10}$$

where P_i is the value of empirical PSF image in pixel i centered on the variable object. The sum is made over the 23 × 23 pixels box around the centroid. The best fit is given by

$$a_{psf} = \frac{\sum_i \frac{P_i^2}{\sigma_i^2} \sum_i \frac{\Delta f_i}{\sigma_i^2} - \sum_i \frac{P_i}{\sigma_i^2} \sum_i \frac{P_i \Delta f_i}{\sigma_i^2}}{det}, \tag{5.11}$$

$$\sigma_{psf}^2 = \frac{\sum_i \frac{P_i^2}{\sigma_i^2}}{det}, \tag{5.12}$$

where *det* is

$$det = \sum_i \frac{1}{\sigma_i^2} \sum_i \frac{P_i^2}{\sigma_i^2} - \sum_i \frac{P_i}{\sigma_i^2}^2. \tag{5.13}$$

Obviously the PSF photometry gives optimal noise and allows the meaningful renormalization for the rejected saturated and dead pixels. This photometric process is performed on all objects in the variable list in all the time series of images and the differential flux $\Delta F = a_{psf}$ light curves are stored in the database with their corresponding error and the root of χ^2 per pixel for the PSF fitting.

We found the PSF photometry is better than aperture photometry. Sperture photometry suffers from the residuals arising from the wide wings of very bright variable stars and the residual of the sky background. So we used the light curve taken by PSF photometry in this analysis.

5.4.1 Noise properties

The error in the PSF photometry σ_{psf} obtained by equation (5.12) would be optimistic, as it includes only the photon noise component. So we tested the properties of the photometry

using a sample of constant stars. We made a catalogue of all stars in the reference frames by using the DoPHOT program to select constant stars. We randomly sampled $\sim$ 1000 constant stars for each image, in which we rejected the variable objects detected in section 5.3.

Noise properties were derived from the residuals of individual measurements around the mean flux of each object. So we used $\sim 100,000$ measurements for each chip. Each residual was normalized by the error from the photon noise σ_{psf} (equation (5.12)) for the corresponding photometric point. Then stars were grouped according to their brightness on the reference image, the standard deviation normalized by σ_{psf} in the PSF fitting, i.e., the root of χ^2 per pixel (we refer to this as $Sdev_{psf}$), and each of the divided 1024×1024 pixels sub-frames. However we could not find any difference in the sub-frames, so we combined all sub-frames into the same group. We thought that the $Sdev_{psf}$ of each measurement should be a good indicator for the systematic noise which comes from the non-photon noise. All residuals coming from th elight curves of stars in a given group were merged into one distribution.

For each group we calculated the half width of the region containing 68.3% of residuals σ_{resid}, a robust estimator of the width σ of the Gaussian distribution. In Figure 5.3, we plot the estimated σ_{resid} as a function of $Sdev_{psf}$ and these are fitted with a 3-degree polynomial. Where bright stars are concerned ($R < -11$ in DoPHOT output magnitude of Red, which corresponds to $I \sim 15$) these were rejected because such bright stars have other systematic deviations as discussed below. The effect of such bright stars is small because the number of bright stars is less than 0.4% out of all possible source stars ($I < 23$), and the pixels where such stars dominate on the CCD chip is less than 1%. And we didn't use the measurements with $Sdev_{psf} > 10$ because these have little reliability. The number of this kind of measurements are $\sim 7\%$ out of all measurements. In this figure, a clear trend for these values can be seen. The fitted curve shown in Figure 5.3 can be used to rescale the error bars in order to improve the consistency of the light curves. We also show the same plot with normalized residuals with this fitted function in Figure 5.3.

To check whether this normalization is appropriate or not, we show the distribution histograms of these residuals (upper panel) and normalized residuals (lower panel) in Figure 5.4. As shown in Figure 5.3, the distribution of normalized residuals is consistent with the normal distribution. So our normalization seems to be reasonable. This trend of chip2 and 3 are very similar but slightly different from chip 1. So we estimated this function for each of the chips. This trend is very similar over the all fields of the same CCD chip. We applied this normalization to all our measurements.

We also show the σ_{resid} of residuals (filled circle) and normalized residuals (cross) as a function of brightness of constant stars in DoPHOT magnitude in Figure 5.5. As shown in Figure 5.5, as we move towards brighter stars the σ_{resid} increases due to systematic effects related to the uncertainty of the seeing and the PSF, first slowly and then faster. Alard & Lupton (1998) provide a possible explanation in terms of the atmospheric turbulence. Another possible source of this excess is the existence of some small amplitude variable stars in these bright stars. So, we didn't bother to correct this effect in this analysis. In

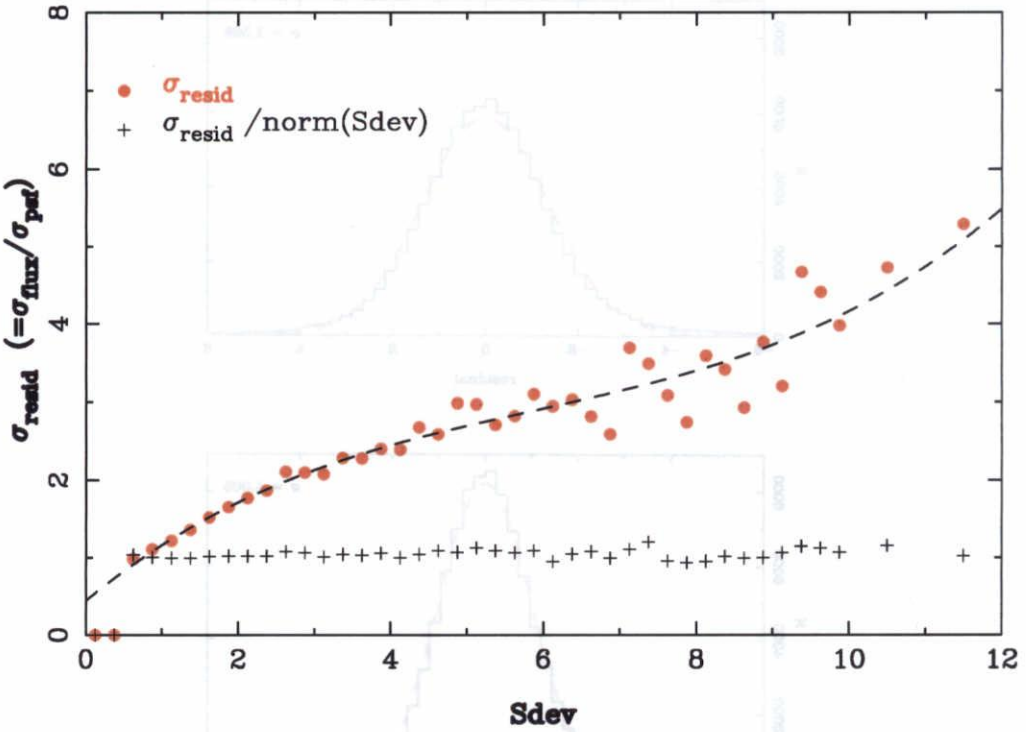

Figure 5.3: The half width of the region containing 68% of residuals which are a ratio of the actual scatter to the photon noise estimate as a function of standard deviation in PSF fitting (filled circle) and the same plot with renormalization (cross). The data in this plot come from 90,000 individual measurements of 1,000 constant stars. The dashed line indicates the best fit for the residual plot with 3-degree polynomial. and this function is used as the renormalization function.

Figure 5.5, we found that the noise (standard deviation) in this analysis is about 40% above the photon noise limit.

5.5 Calibration of Fluxes

The information derived by DIA is slightly different than that from conventional photometry such as DoPHOT. Difference imaging returns relative photometry ΔF in linear flux units, that is the light curve from which some constant flux has been subtracted. This value depends on the brightness of the object in question on the reference image F_{ref}. To convert ΔF measurements onto a magnitude scale, it is necessary to determine a corresponding "total flux" F_{total} given by

$$F_{total} = F_{ref} + \Delta F. \tag{5.14}$$

If the source star is bight enough and isolated on the reference image, then F_{ref} can be measured by applying a profile fitting program such as DoPHOT to the reference image. However, there are some situations where it may not be possible to measure the reference

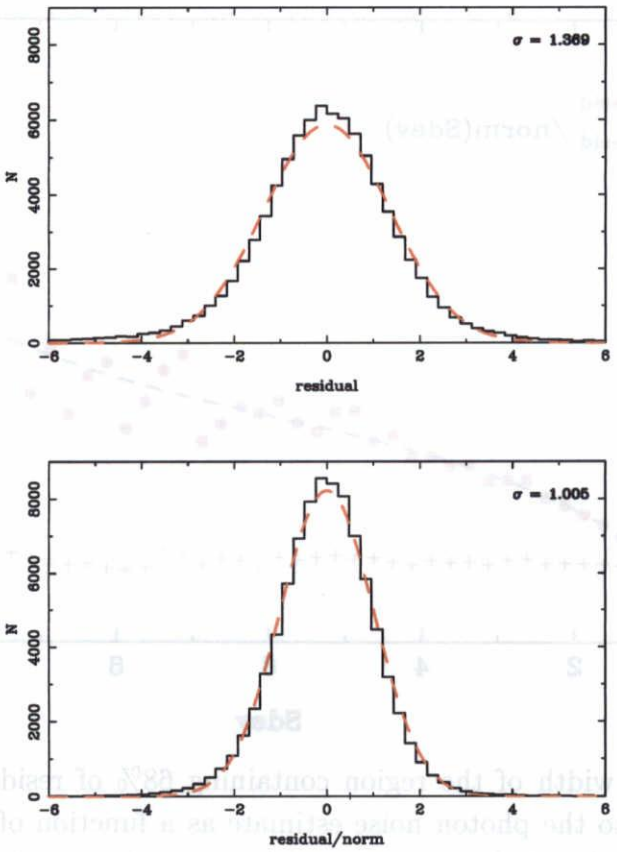

Figure 5.4: The distribution of residuals (upper) and renormalized (lower) residuals for 90,000 individual measurements of constant stars. The data are represented by the histograms and the dotted lines indicate the best fit Gaussian distributions centered on 0. The half widths of the regions containing 68% of the residuals σ are 1.369 and 1.005 respectively.

flux, hence the total flux, for a particular event. If the source star is strongly blended with a close bright star or is fainter than the observation limit, then measurements of a reference flux are impossible. In such a situation , classical profile fitting photometry will not be able to yield a reliable light curve. However photometry with DIA will at least yield a reliable differential flux ΔF light curve. If the S/N of the light curve is high, one can derive the reference flux and unamplified source flux f_0 by fitting a theoretical standard microlensing profile to the observed ΔF light curve (Han 1999). If the S/N is not high enough, then f_0 and the event time scale t_E degenerate, and it is difficult to determine the correct amplification and t_E. For such events there are similarities between the light curve of events with different timescales and amplifications (Woźniak & Paczyński 1997; Bond et al. 2001).

To obtain the source magnitude from the f_0 given by light curve fitting, we need the transformation relation between the flux in the reference image and the apparent magnitude in standard passbands. We used the UBVI photometry catalogue of selected stars in Baade's window provided by OGLE (Paczyński et al. 1999) that are contained in some of

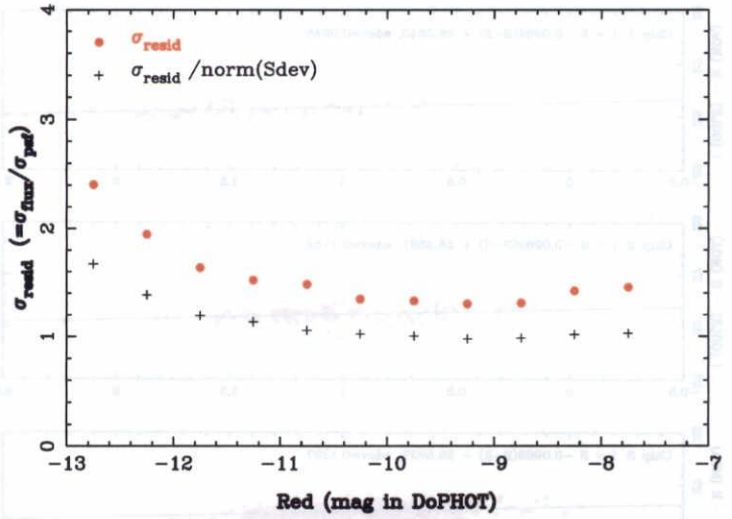

Figure 5.5: The half width of the region containing 68% of the residuals which are a ratio of the actual scatter to the error from the photon noise (filled circle) as a function of Red magnitude in DoPHOT photometry and the same plot with renormalization (cross). The data in this plot come from 90,000 individual measurements of 1,000 constant stars.

the MOA Galactic Bulge fields (ngb2-1, ngb2-2, ngb3-3, where ngb2-1 means chip 1 in field ngb2). In these regions, the extinction is relatively low and uniform. Our reference images are selected from various frames taken at different times. So, the transformation functions driven by using these 3 MOA-OGLE overlap fields are not applicable for other fields and chips.

Therefore, at first, we applied DoPHOT to half of all the frames for each field which contain $\sim$ 20 Blue images taken during the 2000 season. Then we made the $R(MOA)$ and $B(MOA)$ catalogue of all stars in our Galactic Bulge fields by taking the median for each star so as to increase the accuracy of the photometry and to avoid the daily difference of extinction by the atmosphere. And then the DoPHOT photometry R_{ref} on the reference images was compared with the catalogue value R_{med}. The differences are $R_{ref} - R_{med} = -0.1 \sim +0.03$ mag and spatial variations in one chip are about ~ 0.02 mag. So we neglected local differences in the chip and stored one offset value for each chip. These offsets were used in the following calibrations.

Next, the R and B measurements in our catalogue of 3 MOA-OGLE overlap fields were compared with the V and I photometry of the corresponding star in the OGLE catalogue. Fundamentally the transformation to the standard V and I from MOA non-standard R and B depends on the color index $B - R$. The transformations obtained to the standard I and V for each chip are shown in Figure 5.6 and 5.7, and are given by following equations.

$$I = R - 0.0969(B - R) + 26.2840 \quad \text{(chip1)}, \tag{5.15}$$

$$I = R - 0.0969(B - R) + 26.3331 \quad \text{(chip2)}, \tag{5.16}$$

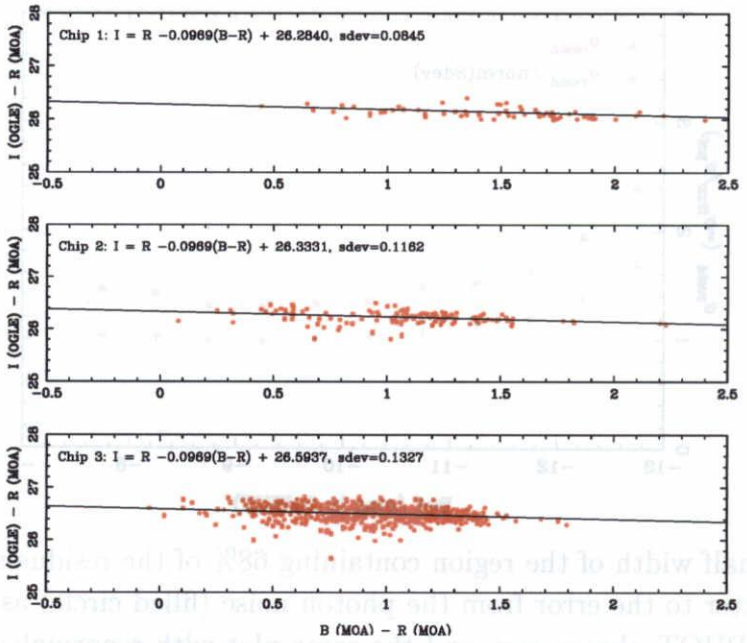

Figure 5.6: Calibration of MOA Red measurements to the standard I band magnitude for the three CCDs (chip1, 2 and 3 from top to bottom) with the color term.

$$I = R - 0.0969(B - R) + 26.5937 \quad \text{(chip3)}, \tag{5.17}$$

$$V = B - 0.160(B - R) + 26.350 \quad \text{(chip1)}, \tag{5.18}$$

$$V = B - 0.160(B - R) + 26.800 \quad \text{(chip2)}, \tag{5.19}$$

$$V = B - 0.160(B - R) + 26.192 \quad \text{(chip3)}. \tag{5.20}$$

Here the slopes were estimated by the using full data of all 3 chips, and the offsets were estimated individually for each chip.

We applied this transformation to our star catalogue made in the previous section 5.4.1. As shown in Figure 5.6, the color dependence in transformation to I from R is weak, and we found that the transformation without a color term seems to work properly, as shown in Figure 5.8. The transformation functions can be written as follows

$$I = R + 26.0923 \quad \text{(chip1)}, \tag{5.21}$$

$$I = R + 26.2210 \quad \text{(chip2)}, \tag{5.22}$$

$$I = R + 26.4963 \quad \text{(chip3)}. \tag{5.23}$$

These equations are very useful because our data were usually taken only in Red.

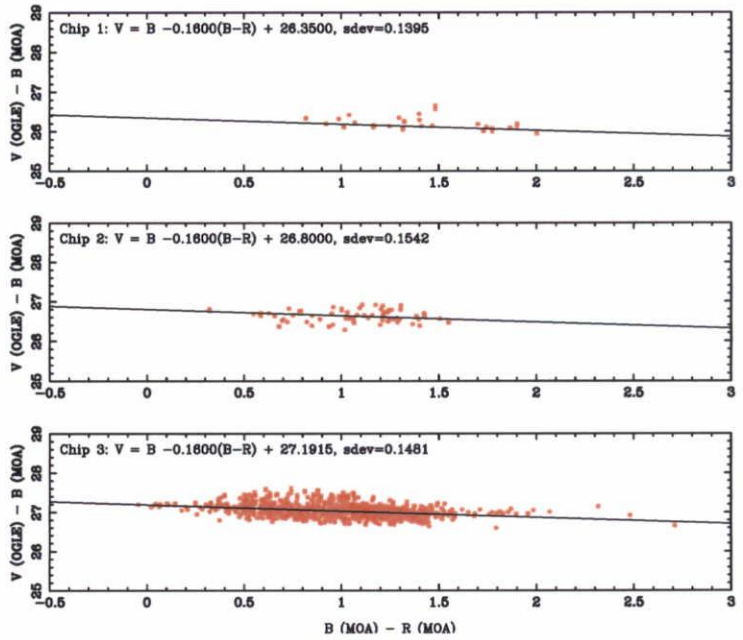

Figure 5.7: Calibration of MOA Blue measurements to the standard V band magnitude scale of the three CCDs of the camera MOA-cam2 with the color term.

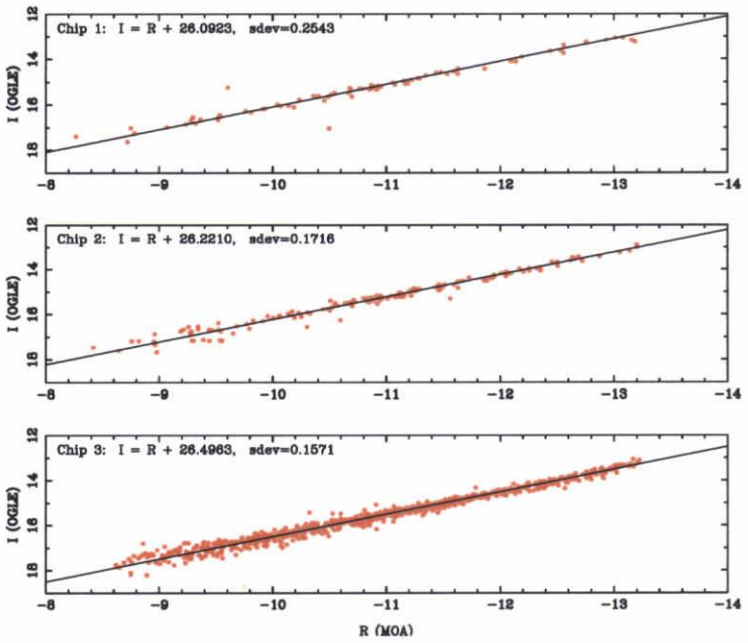

Figure 5.8: Calibration of MOA Red measurements to the standard I band magnitude scale of the three CCDs of the camera MOA-cam2 without a color term.

Chapter 6

Results

The DIA analysis was carried out on the data of 14 fields towards Galactic Bulge taken in the 2000 season (from April to November). These data consist of 7,200 images which correspond to 118 $\sim$ 224 frames for each field depending on their priority, and in total they amount to $\sim$ 100 GByte. Of these images, 6,600 images were successfully reduced. This constitutes $\sim$ 92% of the original data set of observations for these fields. The reduction failures in the analysis occurred as a result of poor data conditions, i.e., bad pointing, poor seeing and very low transmission relative to the reference image due to clouds.

For these subtracted images we found 2,000 $\sim$ 10,000 variable objects in each field. And 200 $\sim$ 1,000 objects of these variable objects passed the "cut1", for which the PSF photometry was performed to make the light curves. For these variable light curves, we applied an additional selection, i.e., "cut2" which search the bump in the light curve and "cut3" in which the microlensing fitting was performed. As a result, we found 28 microlensing event candidates from these light curves.

6.1 Event Selection

To perform event selection one must realize that spurious detections of objects can occur for a number of reasons. One is outbreak object, e.g., asteroids, satellite tracks, cosmic rays, hot pixels, leaked electron from saturated stars, and bad subtraction due to differential refraction. To rule out these spurious detections we required at least two (cut1) or three (cut2) consecutive significant data points. If there are many consecutive excursions in the light curve, we identified these as variable stars. While standard microlensing events have a single peak, we don't require that the microlensing light curve has a single peak throughout the following many selection cuts. Not applying this type of cut allows us to detect binary lensing events which have multiple peaks, but makes the removal of variable stars more difficult. We applied a combination of many loose cuts to reject variable stars. These criteria are chosen empirically.

6.1.1 cut1

The first cut is very loose but effective cut named as "point cut". We applied this cut for the initial variable objects detected in section 5.3 by using the number of detections of each object in a time series of frames.

There are 3 type of events in our data set. The first one is the event in which the source star is not magnified in the reference frame. The second one is that in which the source star is magnified maximumly in the reference image. The third one is in-between, i.e., the source star is magnified but not at the peak magnification in the reference image.

For type 1, the objects are detected only when the source is magnified as a positive excess. For type 2, the objects are detected in almost all frames except around the peak as a negative excess. And for type 3, the same excess as for types 1 and 2, or the combination of a cluster of positive excesses at the peak and a negative base line are detected depending on the phase of magnification in the reference image. By considering these characteristics of each type of events, we required the following criteria for each type.

First we count the number of clusters of positive and negative detections $N_{clus,p}$ and $N_{clus,n}$ which is the consecutive detections whose separation are less than 4 observation frames are grouped as one cluster.

For type 1 which has the no negative detections $N_{det,n} = 0$, the positive detection should be larger than 2, i.e., $N_{det,p} \geq 2$, which rejects many spurious detections and low S/N events. $N_{clus,p}$ should be less than 4 to reject short period pulsating variable stars, and $N_{det,p}$ should not be equal to $N_{clus,p}$ to reject objects with noisy sparse detections. We divided all frames into three regions of observation time, and calculated the detection ratio $Ratio_{1,2,3}$ which is the number of detections $N_{det,1,2,3}$ out of all observation frames $N_{frame,1,2,3}$. We required that the $Ratio_1 \leq 0.1$ or $Ratio_3 \leq 0.1$ to reject some of the long or middle period variables.

For type 2, which has the no positive detection $N_{det,p} = 0$, the negative detection should be larger than a quarter of all observation frames, i.e., $N_{det,n} \geq N_{frame}/4$ because these negative detections represent the base line. This cut rejected many spurious detections. $N_{clus,n}$ should be less than 5 to reject short period pulsating variable stars because the base line should be stable.

For type 3 which has both positive and negative detections, $N_{clus,p}$ should be less than 4, and $N_{clus,p}$ should be less than 5 to reject short period pulsating variable stars, the same as for types 1 and 2. Either of the criteria for type1 $N_{det,p} \geq 2$ and $N_{det,p} \neq N_{clus,p}$, or for type2 $N_{det,n} \geq N_{frame}/4$ should be satisfied. We listed all these criteria of cut1 in Table 6.1.

These cuts reduce the variable objects in order, from thousands ($2,000 \sim 10,000$) to hundreds ($200 \sim 10,00$), depending on each field, without rejecting the microlensing-like light curves. For the objects which passed this cut, PSF photometry was performed and light curve of each object was made as mentioned in section 5.4. These light curves would be tested by following the selection "cut2".

Table 6.1: Selection criteria in cut1.

type	criteria
type 1	$N_{det,n} = 0$
	$N_{det,p} \geq 2$
	$N_{clus,p} < 4$
	$N_{det,p} \neq N_{clus,p}$
	$Ratio_1 \leq 0.1$ or $Ratio_3 \leq 0.1$
type 2	$N_{det,p} = 0$
	$N_{det,n} \geq N_{frame}/4$
	$N_{clus,n} < 5$
type 3	$N_{det,n} \neq 0$ and $N_{det,p} \neq 0$
	$N_{clus,p} < 4$
	$N_{clus,n} < 5$
	($N_{det,p} \geq 2$ and $N_{det,p} \neq N_{clus,p}$) or $N_{det,n} \geq N_{frame}/4$

6.1.2 cut2

The second event selection "cut2" named "Bump filter" was applied to the light curves of variable objects which passed "cut1". This cut searched for a microlensing-like "Bump" in the light curve on the stable baseline. This cut rejected many variable stars from the database which had passed the looser cut1. This cut is very quick. So reducing the number of candidates by this cut is very effective because the following "cut3", in which the microlensing model fitting is applied, is relatively slow.

At first, we required the minimum number of photometric data points to be 70 points. Next we set the time interval of 120 days as a "window" in the light curve, where the number of data points in the window N_{in} and outside the window N_{out} are required to be more than 3 and 9 points respectively. In this window, we counted the number of peaks N_{peak}, which is defined to be that consecutive excess whose significance is larger than 2.5σ and at least the significance of 2 points of these should larger than 4σ. Here the significance of each photometric point is calculated as follows

$$\sigma_i = \frac{f_i - f_{med,out}}{\sqrt{\sigma_i^2 + \sigma_{out}}}, \tag{6.1}$$

where f_i and $\sigma_{f,i}$ are the flux and error of the ith data point, and $f_{med,out}$ and σ_{out} are the median value and variance of data points using outside the window.

To pass this cut, N_{peak} is required to satisfy $1 \leq N_{peak} \leq 3$, and the maximum of the sum of the significance of the points in each peak $\sum_{i,peak} \sigma_i$ should be larger than 20. We defined a high excess as one or more consecutive data points whose significance is larger than 2.5σ, i.e., all excesses including "peak" defined above and one which is not significant to categorize as a "peak". The number of the high excesses N_{hi} in the window should be less than 6, which rejects short period variables and noisy light curves.

We required that the reduced chi-square of data outside the window χ^2_{out} should be less than 4. But if the ratio of chi-square inside and outside the window χ^2_{in}/χ^2_{out} is larger than 15, the cut with χ^2_{out} is not required, so as to allow the high S/N long duration events to pass. We listed all these criteria of cut2 in Table 6.2.

Table 6.2: Selection criteria in cut2.

$N_{total} \leq 70$
$N_{in} > 3$
$N_{out} > 9$
$1 \leq N_{peak} \leq 3$
$\sum_{i,peak} \sigma_i \geq 20$
$N_{hi} < 6$
$\chi^2_{out} < 4$ or $\chi^2_{in}/\chi^2_{out} \geq 15$

In this "cut2", 24,543 candidate light curves were reduced to 1,014 in all our Galactic bulge fields. The resultant light curves are microlensing candidates, dwarf novae and some long period variables (LPV).

6.1.3 cut3

For the light curves which passed cut2, the microlensing model fitting with equations (2.12) $\sim$ (2.15) are applied in cut3. Actually, in DIA, we observe only the variation of the flux from that in the reference image as follows

$$\Delta F(t) = F_0 A(t) - F_0 A(t_{ref}), \tag{6.2}$$

where F_0 indicates a baseline source flux which is not amplified. And t and t_{ref} are the time when the current and the reference image are taken respectively. The background blending flux F_b in equation (2.15) is canceled out in this formula. In general the reference image does contain some lensed flux and is not equal to the baseline flux. Even if the source is not visible at baseline, the best seeing images used to form the reference image may occur when the source is lensed. This is true for some of the microlensing events presented here. The equation (6.2) with four parameters (F_0, t_0, u_{min}, t_E) is applied to differential flux ΔF light curves in this cut3.

To check the shape of the light curve we used standard χ^2 statistics. The reduced chi-square χ^2 in a microlensing fit are required to be less than 3.5 to reject most of LPVs and noisy light curves, although very high S/N events are sometimes not well fitted by the standard microlensing model because of exotic effects such as parallax. So, for the events whose peak flux is larger than 450,000 ADU, we required $\chi^2 < 100$ instead of $\chi^2 < 3.5$, which still doesn't pass the very bright LPVs. The event ngbl-2-2717 falls into this category because of the parallax effect. After these cuts, 75 light curves still remain, most of which

have a clear single peak and stable baseline. These are microlensing candidates, dwarf novae and low S/N faint LPVs.

The main background in this microlensing event selection are dwarf novae which can be quite well fitted by microlensing in the case of poor sampling. In our light curves which passed the cut1, 20 light curves are clearly identified as novae. These have usually single and sometimes multiple asymmetric flares in the light curve, which usually rise quickly and fade slowly.

To check whether each object is nova or not, we used the existing light curves measured by the MACHO group (http://wwwmacho.mcmaster.ca/) because some fraction of our GB fields are overlapping with those of the MACHO group. We cross-referenced each position of the objects to the existing objects in the MACHO group's database and found other flares in the light curves of 5 objects, i.e., these are clearly novae. The novae are much bluer during the outburst. However we usually observed only with the Red filter to increase the sampling rate, and only sometimes took Blue exposures (only about 30 frames for each field). For 23 light curves in these 75 candidates, we could measure the color during the flare. Five of these 23 light curves are categorized as dwarf novae because they a have very blue color ($V - I \leq 1.0$). In 15 light curves, including 5 of the above 10 novae, an asymmetric flare is clearly shown. In total 20 objects are categorized as dwarf novae.

Two of these novae were rejected at cut2. And one nova was removed at χ^2 cut in cut3. To reject other novae, we didn't impose the color cut because we have no color information in most of the light curves. On the other hand we have frequent sampling data points for these objects, which makes it easier to identify a nova from the shape. And we found the following cuts could reject almost all dwarf novae in addition to LPVs.

The minimum impact parameter u_{min} should be less than 1. The 15 novae were fitted with a large u_{min} as a result of the their characteristic shape of the light curve. Some of LPVs are also cut with this criterion. Furthermore we imposed the condition that the timescale should be $t_E < 200$ days. Two further novae were rejected here, which were fitted to very large event timescales ($t_E > 1000$ days). In consequence, all novae which were clearly identified were rejected by these cuts. Especially 5 of these were identified as novae not by a clear shape of the flare but by their color or by the existence of other flares in past data. Though the probability to get the color or to be cross-referenced to the objects in the MACHO group's database is at random, all novae are rejected by our cuts. These results give us the confidence that all novae were rejected by these cuts. Even if a few novae are not rejected, it should not be a significant fraction in our results.

At the same time 9 microlensing-like light curves, which could not be clearly distinguished whether they are novae or microlensing, were rejected with this cut. In some microlensing events which are measured only around the peak, the time scale t_E and the impact parameter u_{min} would be degenerate. Due to this degeneracy the light curve with large t_E and small u_{min} represent similar light curves to those with small t_E and large u_{min}. For some of these events the best fit t_E would be very large with very small u_{min}. Such events are useless for the optical depth estimation. If the S/N of the light curve is high, one can derive the unamplified source flux F_0 by fitting a theoretical standard microlensing

profile to the observed differential flux ΔF light curve even for the events with a faint source star (Han 2000). So some real microlensing events might fail at this cut. These effects are also seen for the artificial events with faint source stars in our simulation (see section 8.3). If both the colors are taken simultaneously or the catalogue of novae is made, we can easily distinguish real microlensing events from novae and issue the alerts. Such kinds of events are usually high magnification events, because their source star is fainter than the observational limiting magnitude. If the baseline flux is measured by follow up observations with larger high resolution telescope such as HST or VLT, the timescale is well constrained. Other LPVs are also cut here.

As a result, 31 objects passed all these criteria. In these light curves 3 low S/N LPVs still remain. We rejected these variables directly as we were doing in real-time analysis (Bond et al. 2001) instead of imposing more complicated criteria. In real-time analysis we made the list of variable stars and the objects whose positions are matched to these variable stars were rejected. This treatment doesn't affect the optical depth estimation because this is position-dependent and these positions are rejected in following all our optical depth analysis in the simulation.

As a result, we found 28 microlensing event candidates in our GB database during 2000. Three out of 20 candidates which are reported in real-time analysis (Bond et al. 2001) failed in this off-line analysis because t_E were not well constrained in these low S/N events. And 11 new candidates were found in this off-line analysis. This is because we changed the detection threshold when we found variable objects in the subtracted images (see section 5.3). In the real-time analysis the events were selected by eye in many light curves. So the detection rates were heavily dependent on the degree of training of the person, and this was not high at the beginning of the real-time analysis in 2000. We summarize these event selection processes in Figure 6.1.

We show all light curves of these 28 candidates in Figure 6.2 $\sim$ 6.7, where the ΔF data points have been converted to amplifications using the fitted parameters for F_0. The gap around JD = 2451750 in the light curves is due to our camera system not functioning for $\sim$ 40 days.

And we summarize the position of each of the candidates with an ID number in this analysis in Table 6.3. The ID in real-time analysis and alert ID reported in Bond et al. (2001) are also written. We listed the best fit parameters in the standard single-lens microlensing fit and 1σ lower and upper limits in Table 6.4 for all 28 microlensing candidates. The I band baseline magnitude of the source star I_0 is de-reddened to match the HST field by using the I band extinction A_I map of each of the fields (see Chapter 7). These fitted parameters are not biased by the blending effects due to nearby stars which appear in DoPHOT-type analyses (Udalski et al. 1994; Alcock et al. 1997a,b). In DIA all other blending components could be subtracted.

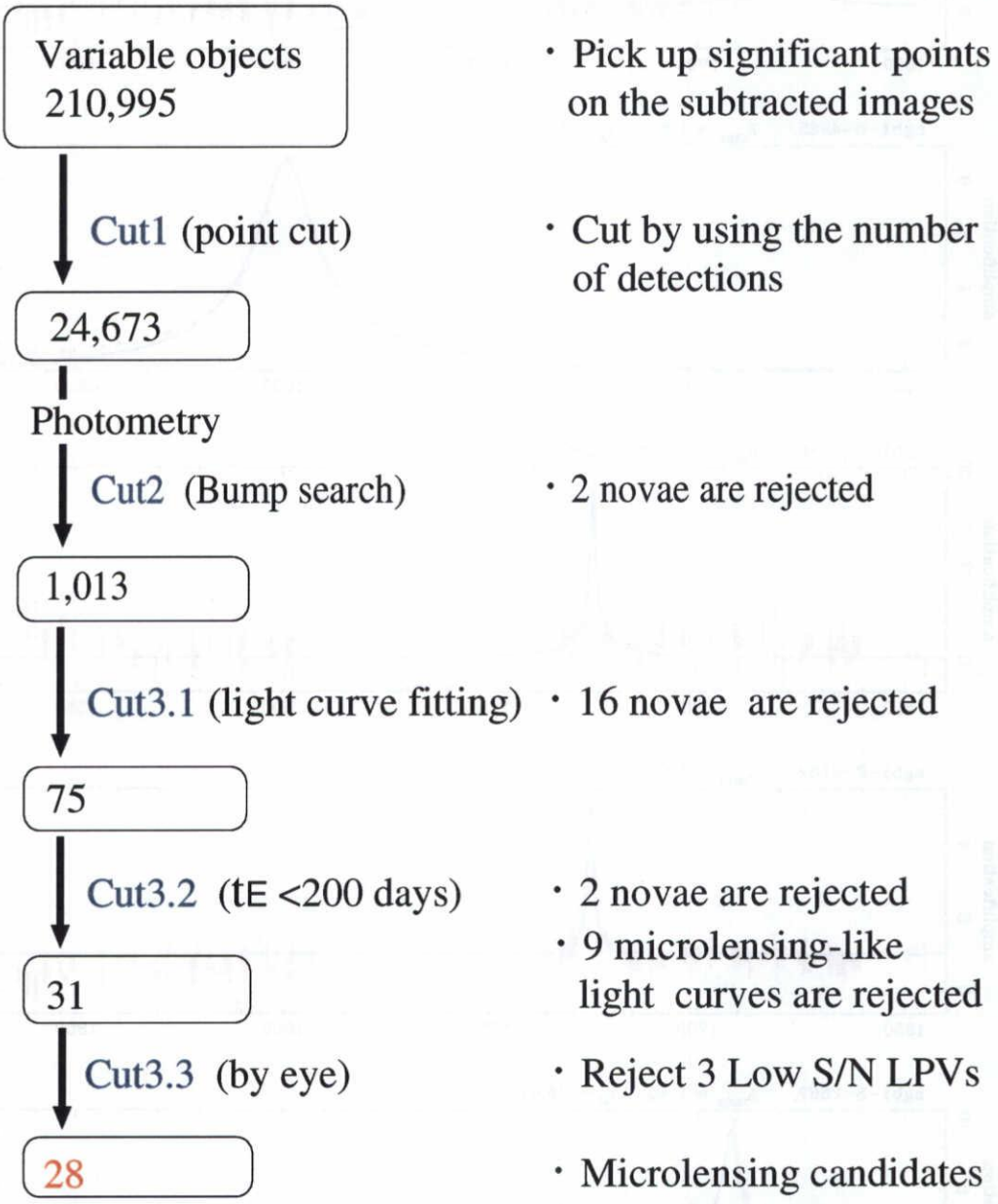

Figure 6.1: A flowchart of the procedure for selection of microlensing candidates.

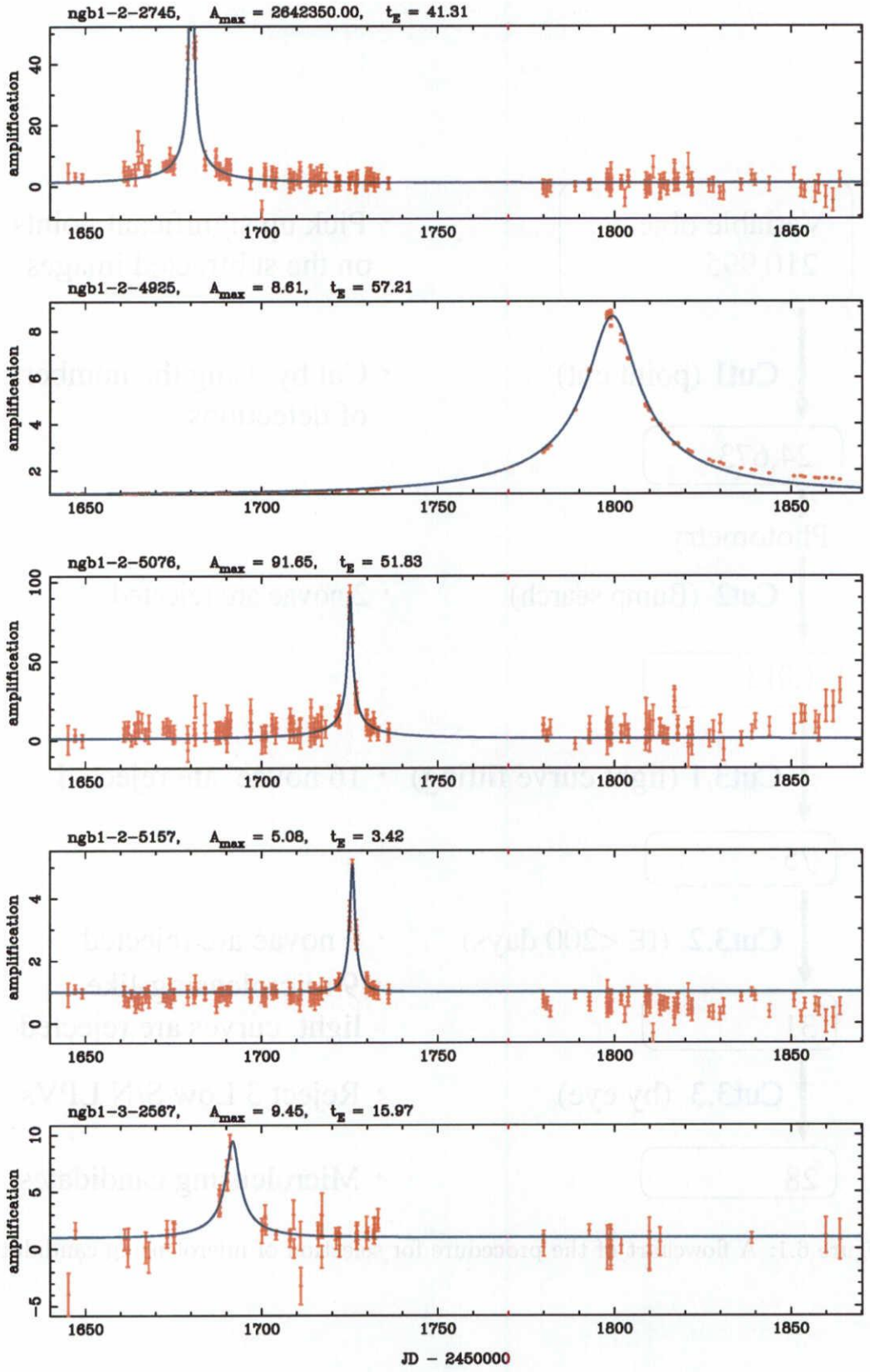

Figure 6.2: Light curves of microlensing event candidates.

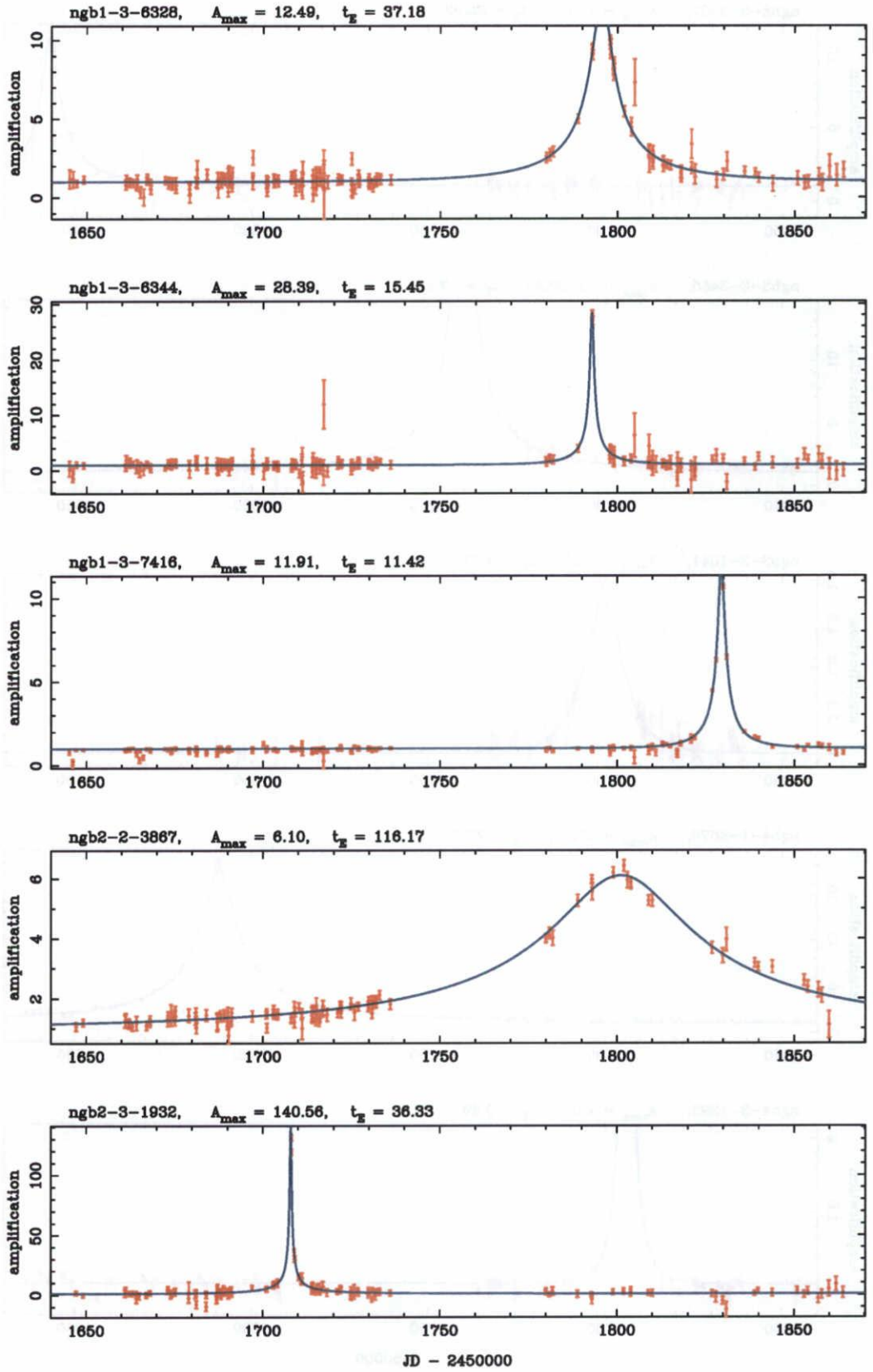

Figure 6.3: Light curves of microlensing event candidates.

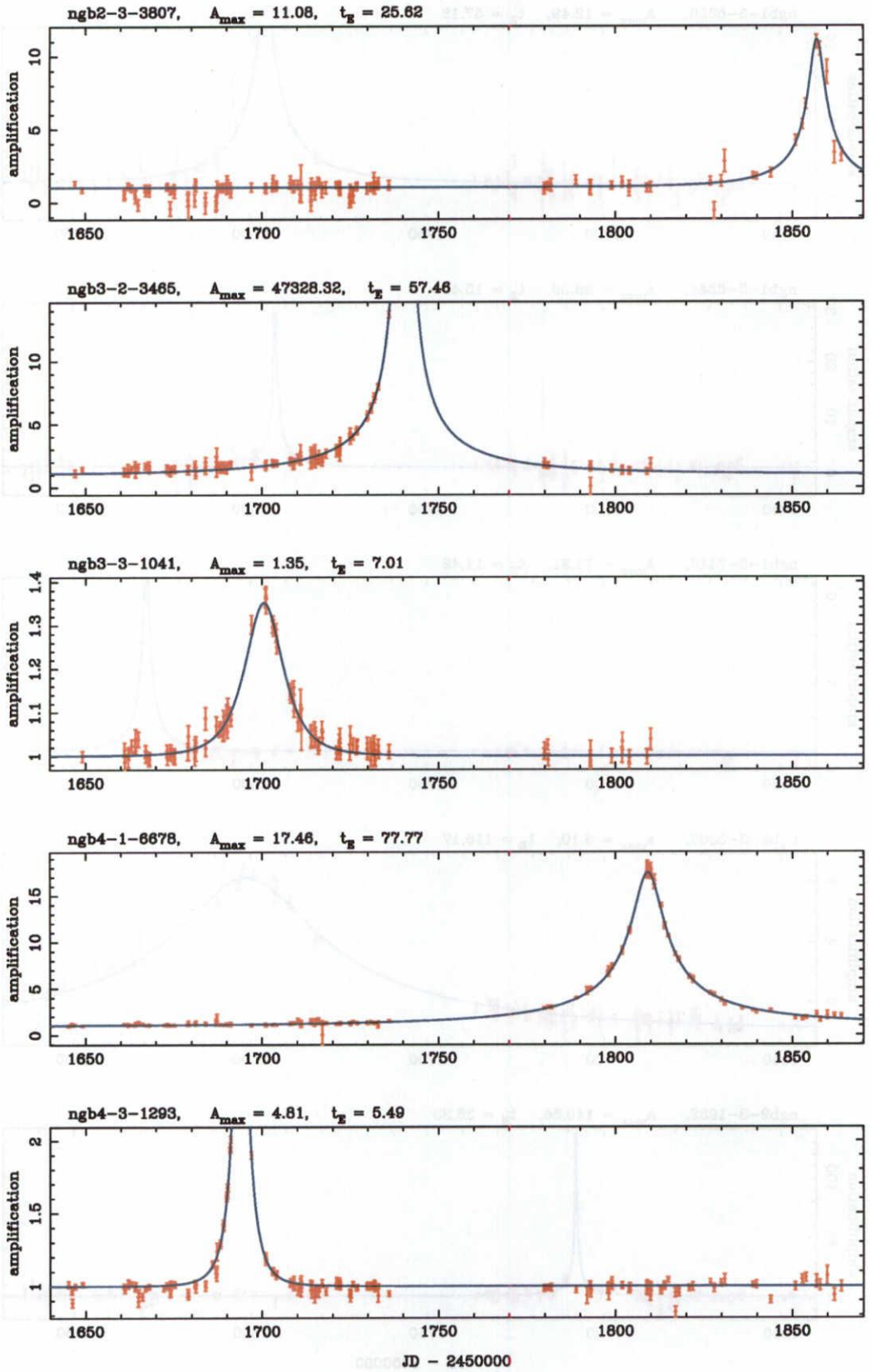

Figure 6.4: Light curves of microlensing event candidates.

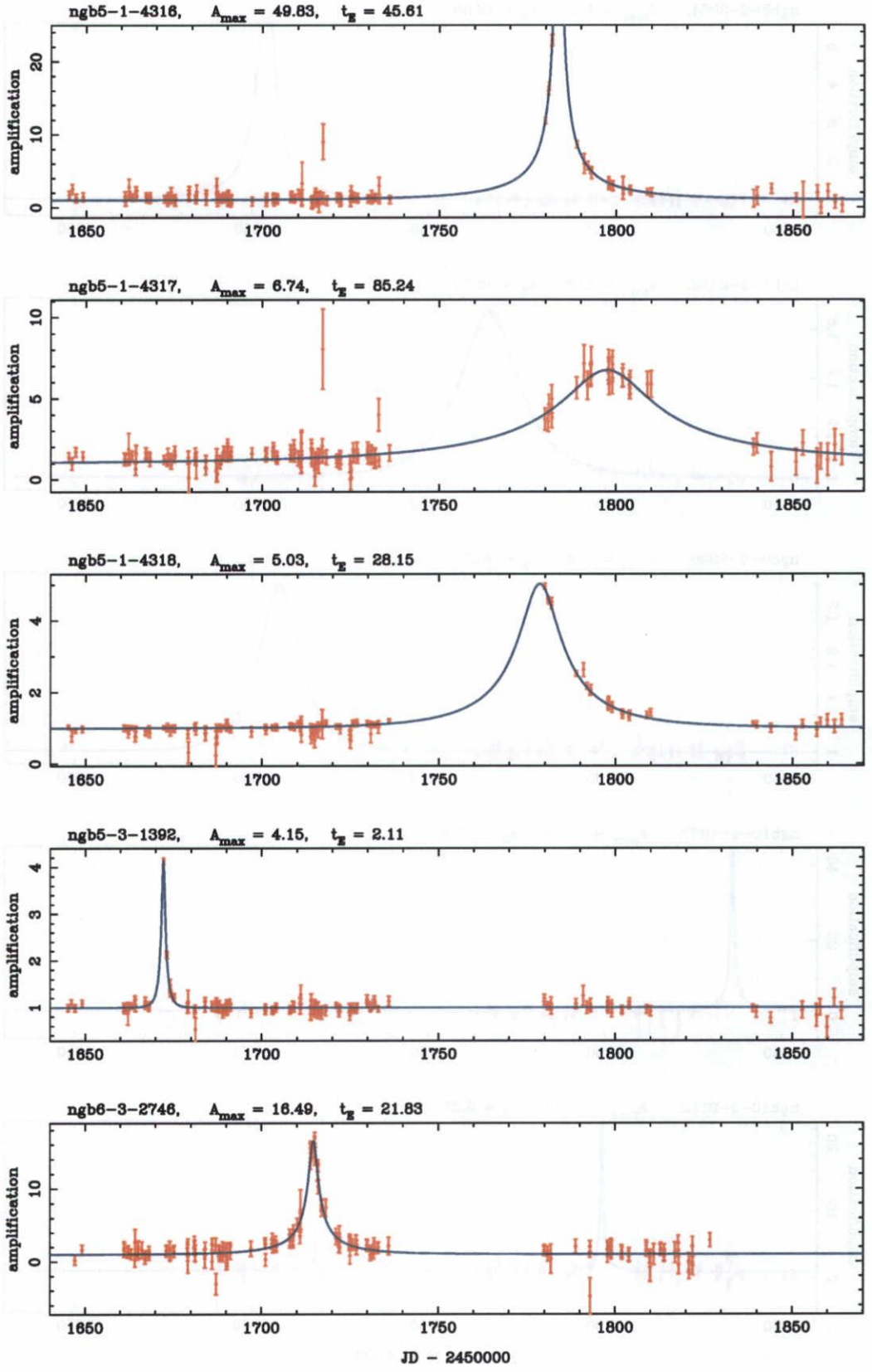

Figure 6.5: Light curves of microlensing event candidates.

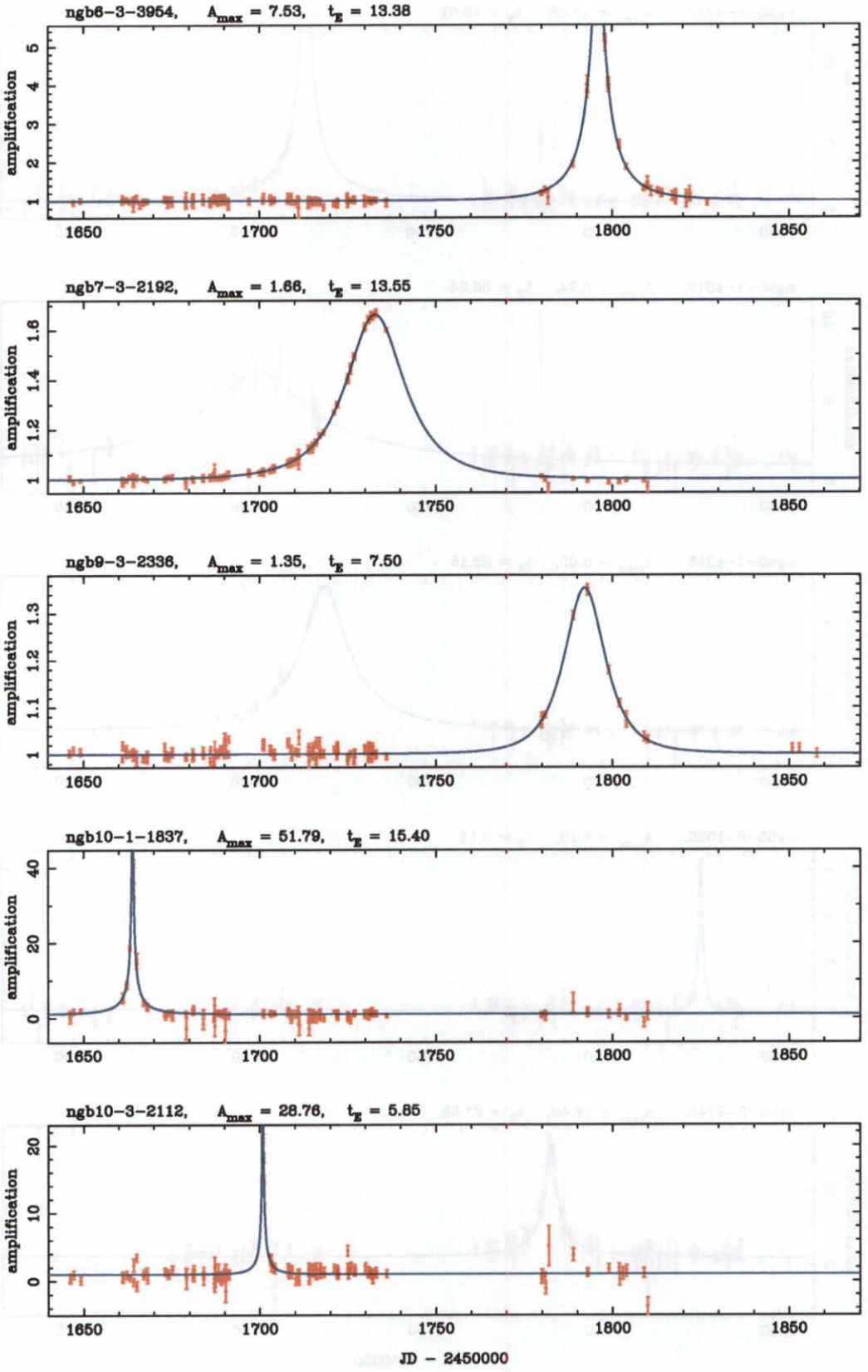

Figure 6.6: Light curves of microlensing event candidates.

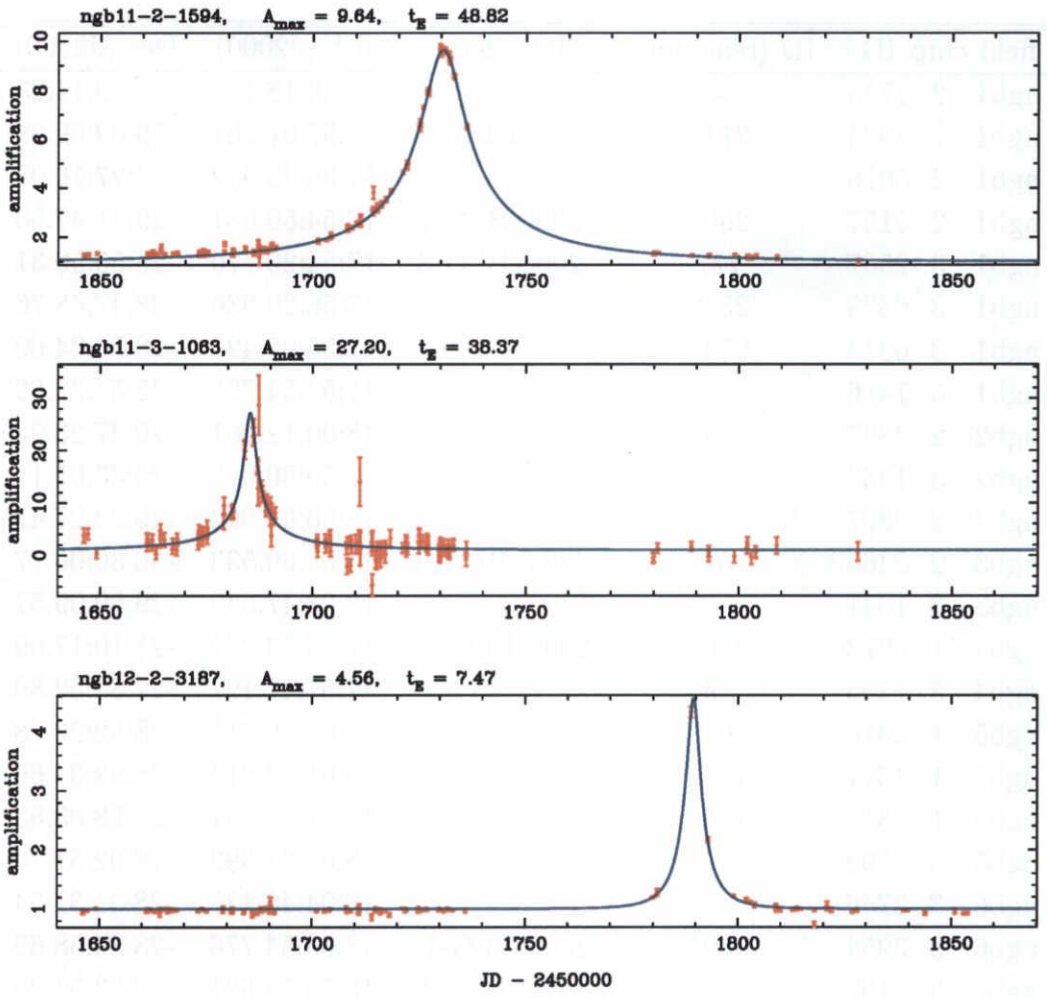

Figure 6.7: Light curves of microlensing event candidates.

Table 6.3: The Position of 28 microlensing event candidates with ID in this offline analysis. The ID in real-time analysis and alert ID in Bond et al. (2001) are also presented.

field	chip	ID	ID (real-time)	ID (alert)	RA (J2000)	Dec (J2000)
ngb1	2	2745	-	-	17:58:13.136	-29:09:14.23
ngb1	2	4925	2717	2000-BLG-11	17:57:07.907	-29:09:59.28
ngb1	2	5076	-	-	17:56:33.952	-29:27:16.08
ngb1	2	5157	2667	2000-BLG-7	17:54:56.681	-29:31:47.50
ngb1	3	2567	727	2000-BLG-3	17:54:29.770	-28:55:59.31
ngb1	3	6328	2540	-	17:58:20.936	-28:47:48.76
ngb1	3	6344	2548	-	17:55:05.425	-28:50:34.60
ngb1	3	7416	-	-	17:57:54.728	-28:54:32.66
ngb2	2	3867	1648	-	18:00:12.361	-29:37:23.93
ngb2	3	1932	-	-	17:59:00.087	-29:33:01.11
ngb2	3	3807	-	-	18:00:07.092	-29:23:27.47
ngb3	2	3465	1316	2000-BLG-9	18:05:09.533	-30:36:06.77
ngb3	3	1041	-	-	18:06:47.640	-29:50:09.57
ngb4	1	6678	2806	2000-BLG-13	17:55:33.202	-28:10:17.09
ngb4	3	1293	159	-	17:57:47.197	-27:33:52.80
ngb5	1	4316	1673	-	18:01:06.711	-28:52:22.28
ngb5	1	4317	1672	-	18:01:26.814	-28:52:34.66
ngb5	1	4318	1668	-	18:01:44.791	-28:58:03.53
ngb5	3	1392	-	-	18:01:21.393	-28:02:51.70
ngb6	3	2746	-	-	18:04:46.138	-28:31:31.54
ngb6	3	3954	1425	2000-BLG-12	18:03:54.776	-28:34:58.62
ngb7	3	2192	703	2000-BLG-8	18:10:55.621	-29:03:54.20
ngb9	3	2336	841	-	18:10:17.990	-27:31:19.31
ngb10	1	1837	-	-	18:08:32.453	-26:09:29.66
ngb10	3	2112	-	-	18:08:51.926	-25:24:40.46
ngb11	2	1594	1142	2000-BLG-10	18:11:28.310	-26:15:05.81
ngb11	3	1063	-	-	18:11:57.020	-25:54:57.32
ngb12	2	3187	1052	-	18:14:47.421	-25:32:53.64

Table 6.4: The parameters in microlensing light curve fitting for 28 candidates. I band baseline magnitude of source star I_0 is de-reddened to match the HST field by using the I band extinction A_I map of each of the fields (see Chapter 7). The symbol "-" means that a value could not be constrained.

MOA ID			t_0	A_{max}			t_E/days			I_0
field	chip	ID	JD-245000	lower	best	upper	lower	best	upper	mag
ngb1	2	2745	1680.16	200.0	2.6×10^6	8.8×10^8	26.9	41.3	-	19.7
ngb1	2	4925	1799.38	8.5	8.6	8.7	56.9	57.2	57.5	13.6
ngb1	2	5076	1725.17	56.1	91.7	234.4	33.2	51.8	106.4	20.8
ngb1	2	5157	1725.79	4.1	5.1	6.2	2.9	3.4	4.0	17.1
ngb1	3	2567	1691.82	2.9	9.4	293.9	6.9	16.0	-	17.5
ngb1	3	6328	1795.55	9.4	12.5	16.8	30.6	37.2	45.9	17.6
ngb1	3	6344	1792.80	14.9	28.4	60.3	10.0	15.4	27.3	18.3
ngb1	3	7416	1829.40	10.6	11.9	13.2	10.6	11.4	12.2	16.2
ngb2	2	3867	1801.09	4.6	6.1	9.1	92.0	116.2	163.6	17.4
ngb2	3	1932	1707.91	76.5	140.6	361.4	21.1	36.3	181.2	19.9
ngb2	3	3807	1857.06	7.2	11.1	17.6	18.1	25.6	37.9	17.8
ngb3	2	3465	1740.18	979.3	47328.3	47375.7	46.0	57.5	220.6	18.5
ngb3	3	1041	1700.57	1.2	1.4	1.9	0.3	7.0	9.6	15.1
ngb4	1	6678	1809.17	16.4	17.5	18.6	73.4	77.8	82.4	16.2
ngb4	3	1293	1693.95	3.0	4.8	12.8	4.8	5.5	6.2	14.5
ngb5	1	4316	1783.60	33.5	49.8	89.0	35.2	45.6	62.8	18.1
ngb5	1	4317	1797.46	3.8	6.7	16.9	55.2	85.2	188.2	17.9
ngb5	1	4318	1778.51	3.3	5.0	6.8	22.0	28.2	34.2	16.0
ngb5	3	1392	1672.15	2.4	4.1	5.8	1.6	2.1	3.0	16.5
ngb6	3	2746	1714.69	11.5	16.5	24.6	16.3	21.8	30.9	19.7
ngb6	3	3954	1796.00	6.5	7.5	8.8	12.4	13.4	14.5	16.5
ngb7	3	2192	1732.84	1.5	1.7	1.8	12.7	13.5	14.4	14.6
ngb9	3	2336	1792.14	1.2	1.4	1.9	0.8	7.5	10.3	14.1
ngb10	1	1837	1663.93	38.2	51.8	71.5	12.7	15.4	19.0	19.0
ngb10	3	2112	1700.85	15.0	28.8	-	2.9	5.8	99.4	18.3
ngb11	2	1594	1730.46	9.0	9.6	10.4	45.7	48.8	52.3	16.6
ngb11	3	1063	1685.29	16.5	27.2	82.4	25.6	38.4	107.1	19.7
ngb12	2	3187	1789.45	3.7	4.6	5.6	6.7	7.5	8.2	15.8

6.2 Parallax event

The light curve of the event ngb1-2-4925 was not well fitted by the standard microlensing profile given by equations (2.12) $\sim$ (2.15). The light curve exhibits an asymmetric profile which is characteristic of parallax microlensing. If the event timescale is long the circularly accelerating motion of the Earth around the Sun is not negligible. In this case v_t is not constant any more, but depends on the orbital phase of the Earth, i.e., a time t. To take this effect into account, we must replace the expression of $u(t)$ in equation (2.13) with

$$\begin{aligned} u^2(t) &= u_{min}^2 + \left(\frac{t-t_0}{t_E}\right)^2 + \alpha^2 \sin^2[\Omega(t-t_c)] \\ &\quad +2\alpha \sin[\Omega(t-t_c)]\left[\frac{t-t_0}{t_E}\sin\theta + u_{min}\cos\theta\right] \\ &\quad +\alpha^2 \sin^2\beta \cos^2[\Omega(t-t_c)] \\ &\quad +2\alpha \sin\beta \cos[\Omega(t-t_c)]\left[\frac{t-t_0}{t_E}\cos\theta - u_{min}\sin\theta\right], \end{aligned} \tag{6.3}$$

where θ is the angle between v_t and the north ecliptic axis, and t_c is the time at which the Earth is closest to the Sun-source line (Alcock et al. 1995). Note u_{min} is no longer the minimum impact parameter but is the minimum distance between the lens and Sun-source line. The parameters α and Ω are given by

$$\alpha = \frac{1\mathrm{AU}}{t_E \tilde{v}}\{1 - \epsilon\cos[\Omega_0(t-t_p)]\}, \tag{6.4}$$

and

$$\Omega(t-t_c) = \Omega_0(t-t_c) + 2\epsilon\sin[\Omega_0(t-t_p)], \tag{6.5}$$

where t_p is the time of perihelion, $\tilde{v} = v_t/(1-x)$ is the transverse velocity of the lens object projected to the solar position, $\Omega_0 = 2\pi$ yr^{-1} is the Earth's radial velocity, $\epsilon = 0.017$ is the Earth's orbital eccentricity and β is the angle between the Sun-source line and the ecliptic plane.

Bond et al. (2001) performed the light curve fitting with the best fit standard constant velocity and parallax microlensing models for the event ngb1-2-4925 (MOA–2000–BLG–11) including the data taken by MOA in 1999. We show this light curve along with the best fit standard and parallax microlensing models in Figure 6.8. The best fit parameters are also given in Table 6.5. We will use the values from the parallax fit in Table 6.5 for the following optical depth estimation.

In a parallax event the degeneracy in the mass, lens distance, and transverse velocity could be partially resolved, i.e., $\tilde{v}$ can be obtained. Following Alcock et al. (1995), assuming that the velocity dispersion in the disk and the bulge is negligible, the transverse speed projected onto the solar position can be written as $\tilde{v} = 200x/(1-x)$ kms^{-1}, and the mass of the lens M, can written as

$$M(x) = \frac{1-x}{x}\frac{\tilde{v}^2 t_E^2 c^2}{4GD_s}. \tag{6.6}$$

Substituting the parameters obtained from parallax fit and assuming $D_s = 8$ kpc we obtained $D_l \sim 1.4$ kpc and $M \sim 0.3 M_\odot$.

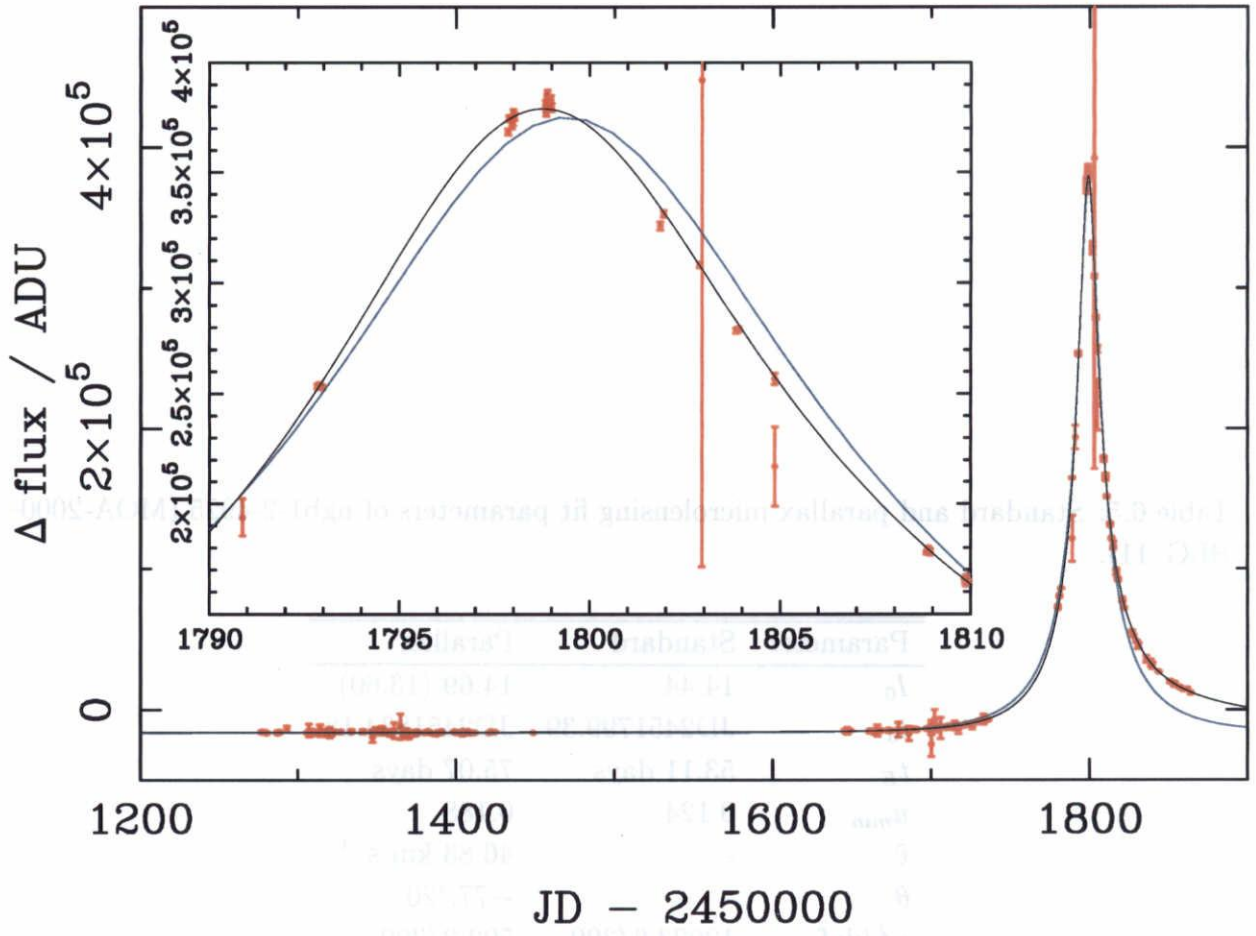

Figure 6.8: Δ flux light curve of ngb1-2-4925 (MOA–2000–BLG–11) with standard and parallax microlensing fits.

Table 6.5: Standard and parallax microlensing fit parameters of ngb1-2-4925 (MOA-2000–BLG–11).

Parameter	Standard	Parallax
I_0	14.44	14.69 (13.60)
t_0	JD2451799.39	JD2451834.18
t_E	53.11 days	75.07 days
u_{min}	0.124	0.188
$\tilde{v}$	-	46.83 km s^{-1}
θ	-	$-77.°20$
χ^2/dof	12023.6/399	592.2/309

Note: The de-reddened I band magnitude is written in brackets. The data taken in 1999 are included in this fitting (Bond et al. 2001).

Chapter 7

Extinction Map

As is well known, the extinction due to dust is very significant towards the galactic bulge. This effect can be seen in the Color Magnitude Diagram (CMD) of our Galactic Bulge fields. We show our CMD of the field near Baade's Window (left panel) and another high extinction field (middle panel) in Figure 7.1. We can see that the CMD is more scattered in the high extinction field than in the Baade's Window field, as a result of the extinction and the reddening. Information on the extinction in each region is needed to estimate the number of stars in this region by using the luminosity function. Here we show how we estimated extinction values for our galactic bulge fields and show the resultant extinction map in the I band.

Many determinations of the extinction towards Baade's Window have been performed in recent years, with a number of different techniques, including those of stellar simulation (Ng et al. 1996), mean magnitudes of red-clump stars (Kiraga et al. 1997), the absolute magnitude of RR Lyrae stars (Alcock et al. 1998) and magnitude of the K-giants (Gould et al. 1998).

Woźniak & Stanek (1996) proposed a new method to investigate the coefficient of the selective extinction, based on two-band photometry, which uses red clump stars as a means to construct the reddening curve. The CMD is used to obtain the quantitative values of the offset on the CMD between the different subfields, caused by differential extinction. They used red clump-dominated parts of the CMDs for determining the offsets, the clump being seen at fainter magnitudes and redder colors in subfields with higher extinction. They applied this method to the OGLE data and then found the selective extinction coefficient $A_V/E_{V-I} = 2.44$. This is consistent with Ng et al. (1996). And Stanek (1996) also applied this method to the OGLE data to obtain differential extinction A_V and reddening E_{V-I} in a $40' \times 40'$ region of Baade's window, with resolution of $\sim 30''$. They estimated $A_V/E_{V-I} = 2.49 \pm 0.02$. Paczyński et al. (1999) applied this method to OGLE-II data. They made a reddening map for their fields ($14'.2 \times 14'.2$ with resolution of $20'' \times 20''$) because determining the reddening E_{V-I} (horizontal shift in CMD) is easier than A_V and A_I (vertical shift in CMD). Then the extinction map was calculated according to the following formulae:

$$A_I = 1.5 \times E_{V-I}, \tag{7.1}$$

$$A_V = 2.5 \times E_{V-I}. \tag{7.2}$$

We applied this method to our bulge fields. We divided our one image into 8×16 subframes which each cover $3.45' \times 3.45'$ region. We made CMDs in I and V for each subframe by using the catalogue made in section 5.4.1 and 5.5. A sample of these CMDs of different subregions in the image near Baade's window is shown in the right panel of Figure 7.1. As shown in this figure, differential reddening is clearly seen, even for the field near Baade's window. We selected the red-clump-giant region in the CMD following Paczyński et al. (1999) as indicated Figure 7.1. These parallel lines are described by the equations

$$I - 1.5(V - I) = 1.2, 13.25, \tag{7.3}$$

where the slope of these lines was chosen so that they are parallel to the reddening vector (Stanek 1996).

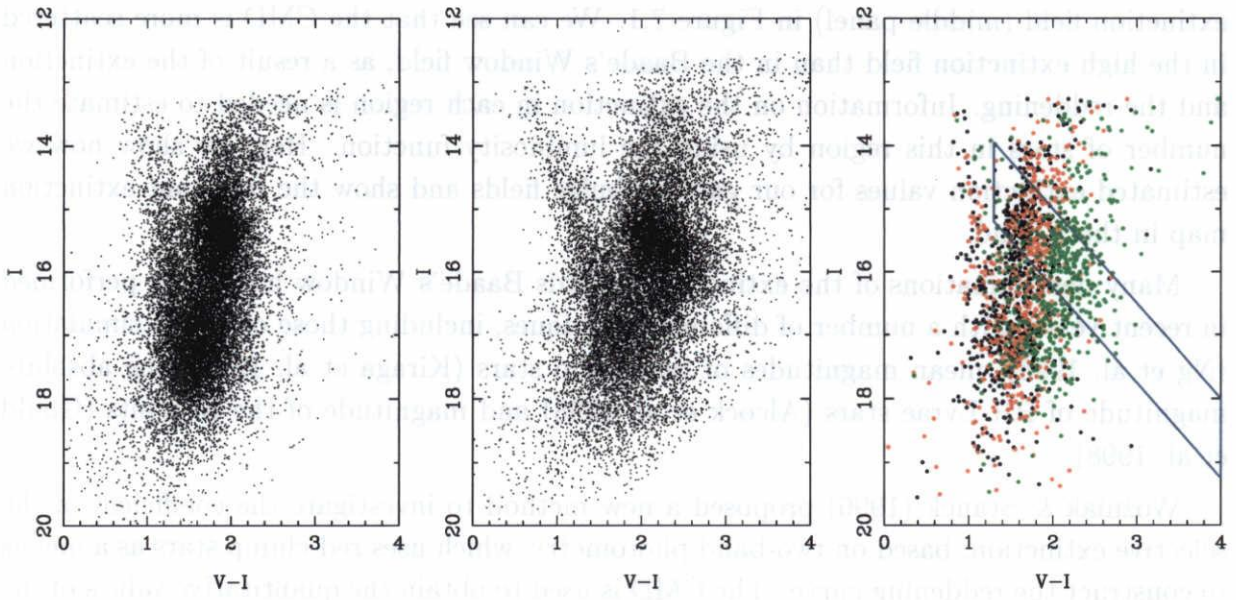

Figure 7.1: Color Magnitude Diagram (CMD) of the Baade's window field (left panel), a higher extinction field (middle panel) and three subregions in the Baade's window field (right panel). The extinction A_I in each of the subregions (in right panel) are 0.761 (black points), 0.984 (red points) and 1.470 (green points). The shift of each plot is clearly seen. The box in the right panel encloses the red clump giant region defined by $I - 1.5(V - I) = 1.2, 13.25$.

We estimated the mean values of $(V - I)$ and I for red clump giants in each of the subregions, which correspond to the correlation between differential reddening $E(V - I)$ and differential extinction A_I. These values in a field are plotted in Figure 7.2, where the best fitted line was given by

$$I = (1.45 \pm 0.12)(V - I) + 12.7. \tag{7.4}$$

This slope is consistent with Stanek (1996). The error in determining this slope mainly comes from the uncertainty in I. The mean color $(V - I)_{mean}$ are more reliable than that of I. So we estimated E_{V-I} from $(V - I)$ by using the following relation and transforming to A_I with equation (7.2).

To get the relation of $(V - I)_{mean}$ and E_{V-I}, we compared the mean color $(V - I)_{mean}$ from our data and the reddening E_{V-I} map (centered on (18:03:20.9, −30:02:06)) calculated with Stanek (1996) in the overlap regions (ngb2-1, ngb2-2 and ngb3-3), where Stanek (1996)'s and our method provide only a differential reddening map. The zero point adopted by Stanek (1996), and therefore also by us, is based on the determination by Gould et al. (1998) and Alcock et al. (1998). A correlation between $(V - I)_{mean}$ and the reddening E_{V-I} is shown in Figure 7.3. The agreement is good, and the relation between $(V - I)_{mean}$ and E_{V-I} is as follows:

$$E_{V-I} = (V - I)_{mean} - 1.18 \pm 0.05. \tag{7.5}$$

Using these relations, we made an I-band extinction A_I map from the $(V - I)_{mean}$ map in our data. This map is shown in Figure 7.4. The error in A_I is about 0.07 mag. This map was used to make a luminosity function for each region. In this map we can see the galactic disk , in which the extinction is high, in the diagonal line from the top-left to bottom-right.

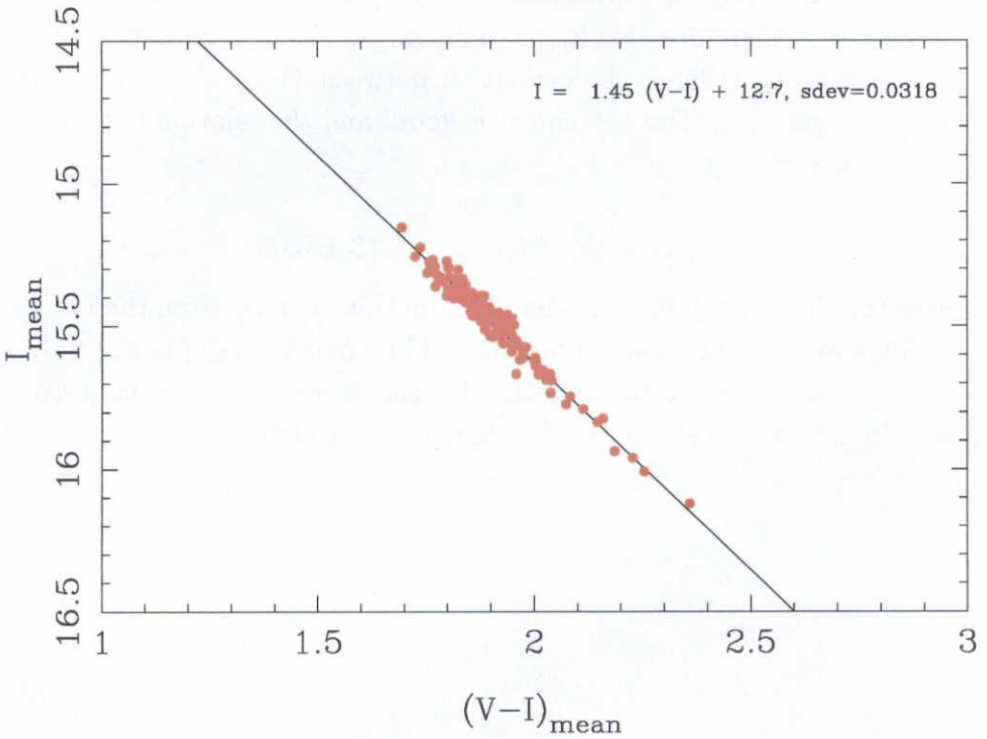

Figure 7.2: Correlation between mean values of $(V - I)$ and I for red clump giants in each of the subregions. This corresponds to the correlation between differential reddening $E(V - I)$ and differential extinction A_V. The fitted line is $I = 1.45(V - I) + 12.7$.

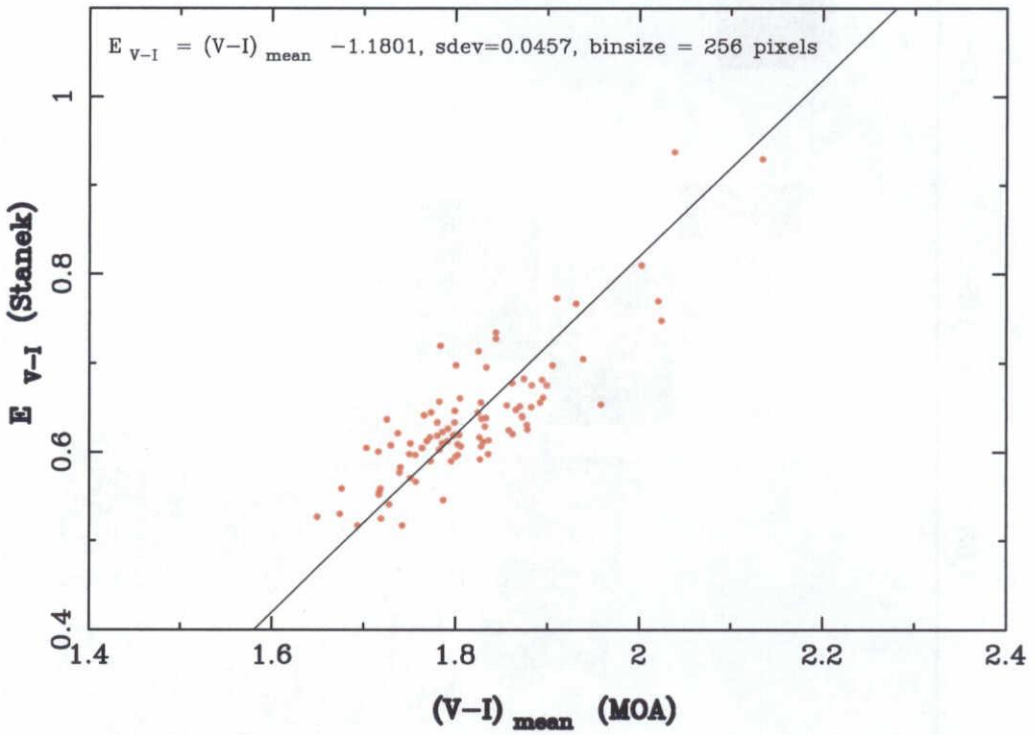

Figure 7.3: Correlation between $(V-I)_{mean}$ from MOA and E_{V-I} from Stanek (1996) in the overlap region. The fitted line is $E_{V-I} = (V-I)_{mean} - 1.18 \pm 0.05$.

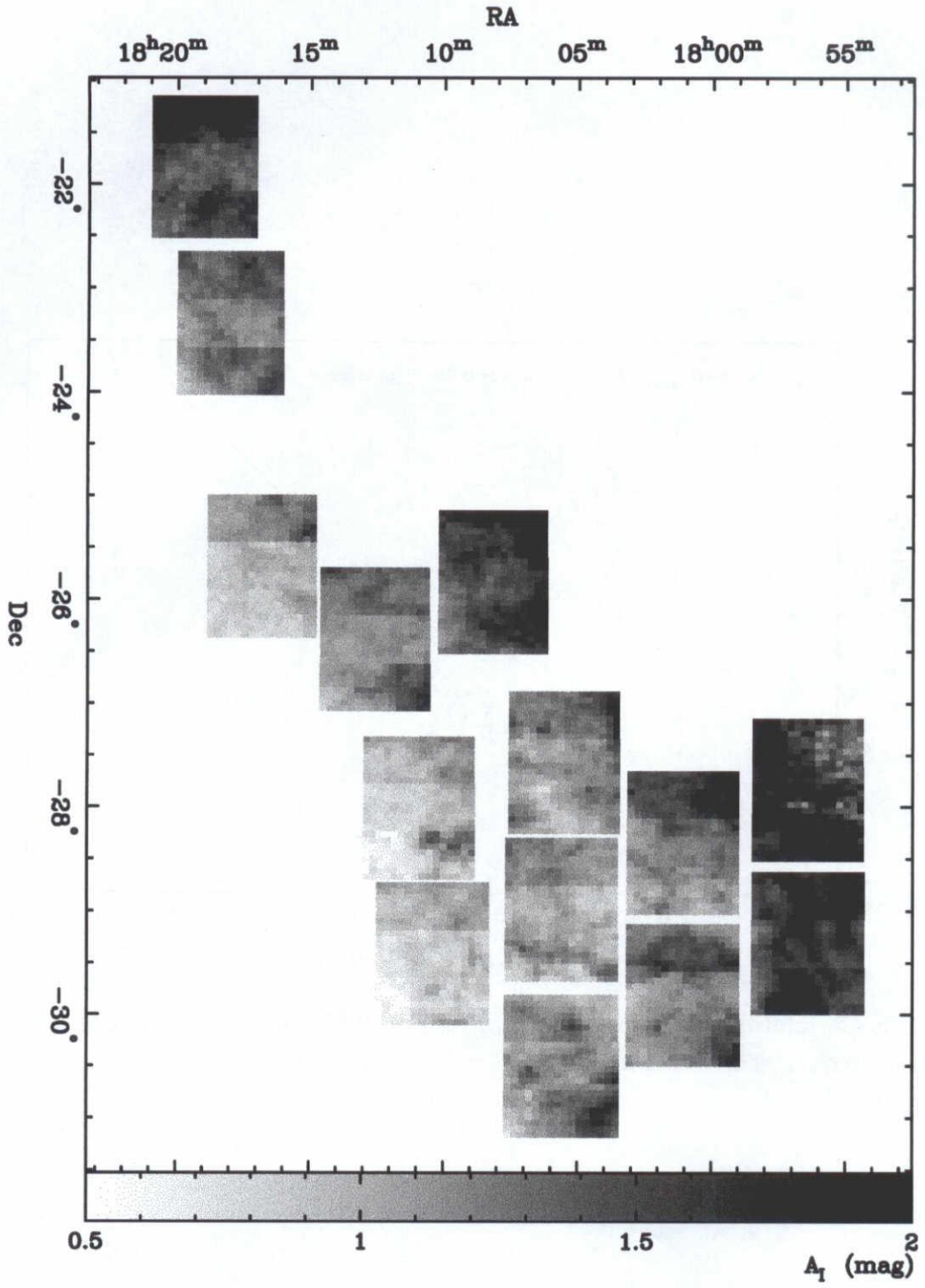

Figure 7.4: I-band extinction A_I map of 14 Galactic Bulge fields. The darker regions indicate higher extinction, whiter regions mean lower extinction. We can see the galactic disk, in which the extinction is high, in the diagonal line from the top-left to bottom-right.

Chapter 8

Optical Depth

To determine the microlensing optical depth from detected events it is necessary to know the detection efficiency of our observation system and analysis technique. In this Chapter we show how we estimated our detection efficiency using the Monte Carlo simulation.

There are a number of ways to determine the microlensing event detection efficiency. One is by adding the microlensed flux into actual photometric light curves of constant stars, which are used for DoPHOT type analysis (Alcock et al. 2000b). However the method of adding the microlensed star images into actual images or all simulated artificial images seems to be better for DIA analysis, because the detection process of variable objects in the subtracted image (see section 5.3) is very important.

A full Monte Carlo approach requires us to know about the existence and distribution of all observational parameters in the analysis. In many real situations there can be hidden parameters which would not be taken into account in this approach.

In this analysis we added artificial microlensed star images to the real subtracted images. Here u_{min} and t_0 of microlensing events, which follow the well known simple distribution, are simulated as random parameters. On the other hand, other parameters whose distribution are not simple (e.g., seeing, extinction, sample rate etc.) are simulated by using real images.

First we derived the luminosity function of the source stars in the Galactic Bulge by combining the existing MOA and HST data. In the previous Chapter we made the extinction map for our observation fields to know the offset of the combined luminosity function for each of the fields. Using this offset luminosity function and the stellar density of bright stars in our field, we estimated the number of all stars in our observation fields down to $I < 23$, which is the event detection limit for our analysis estimated in this Chapter. Next we generated artificial events and counted the number of events which passed the same event selection cuts as applied to the real event selection described in Chapter 6.

Then we estimated the optical depth towards the Galactic bulge by using the events detected in this analysis and our detection efficiencies. We discuss the timescale distribution and optical depth distribution as a function of timescale.

8.1 Luminosity Functions

To add the artificial microlensing events, we have to know the distribution of the luminosity of source stars, i.e., the Luminosity Functions (LF) of Galactic bulge fields. Recently there have been a number of observations of the LF for the Galactic bulge (Holtzman 1998; Ruelas-Mayorga & Noriega-Mendoza 1995). We used the deepest observations with WFPC2 camera of HST from Holtzman (1998), which measured stars in Baade's window down to V (F555W) ~ 28 and I (F814W) ~ 24. A completeness correction has been applied for the HST LF for fainter stars. The bright end of the HST LF is poorly defined, because the field of view of the HST WFPC2 is small (~ 5 arcmin^2). On the other hand, the MOA data have a large number of bright stars because of the wide field of view (~ 1.2 deg^2), but are poor for fainter stars. So we combined the HST LF and MOA LF at $I = 15 \sim 16$ as shown in Figure 8.1. Here the MOA LF is made from stars in field ngb2-2 (0.4 deg^2) which includes the HST field. The photometry of stars in local subregions over this field have a different offset due to differential extinction (see Chapter 7). These offsets are corrected to match that of the HST field ($A_I = 0.742$ mag). We used the MOA LF for $I < 16$ and the HST LF for $I \geq 16$ in this analysis. We used this composite LF for all our Galactic bulge fields assuming that the morphology of the LF doesn't vary between the small HST field and the large MOA fields.

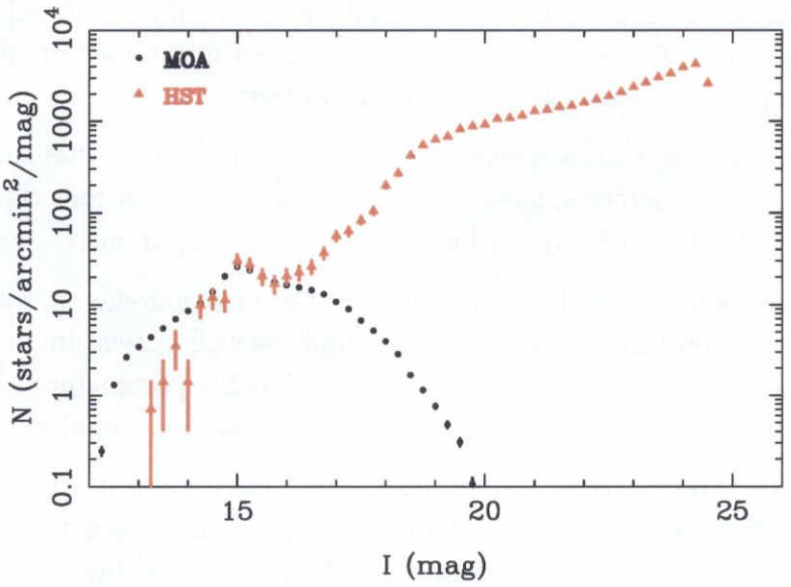

Figure 8.1: Combined luminosity function of Baade's window from MOA (filled circle) and HST (filled triangle). The completeness corrected HST data are from Holtzman (1998). MOA data are from ngb2-2 which have an overlap region with the HST field. For these MOA data the offset value due to differential extinction was corrected to match that of the HST field. We used MOA data for $I < 16$ and HST data for $I \geq 16$ as the luminosity function of stars in this analysis.

8.2 Simulation

To estimate the event detection efficiency of this analysis, we have done a Monte Carlo simulation for each field. We generated 160,000 artificial microlensing events in each sub field, i.e. each CCD chip. Those parameters which follow the well known simple distribution such as the position (x, y), the peak time t_0 and the impact parameter u_{min} were selected at random. And the magnitude of the source star was weighted with the LF of the Galactic bulge made in previous section. And many other components which are expected to affect the event detection were automatically simulated because we used real subtracted images in this simulation. And we counted the number of artificial events which passed all criteria for the real event selection. And we made our detection efficiency as a function of the event time scale t_E.

8.2.1 Artificial event generation

To generate artificial microlensing events, we added the artificial differential star images on a time series of real subtracted images which are current images after subtracting the reference image in section 5.2.3. The differential stars were made from the same PSF as that of each frame and scaled by the differential flux expressed in equation (6.2). Each PSF was formed by the same procedure as in section 5.4. The local high S/N PSF in the reference image was convolved by the kernel which was actually used in the analysis of the corresponding frame and normalized.

To make artificial images more realistic, in generating the artificial image, the photon noise was taken into account following Poisson statistics with an additional flux in the current image. The flux in all subtracted images was scaled to match the reference image in its ADU value (see section 5.2.3). The ADU flux of the artificial star in the current image $F_0 A(t)$ in equation (6.2) was calculated in the scale on the reference image. So, to estimate the photon noise from the additional flux, this additional flux should be transformed to the number of electrons in the current image. The number of electrons in the current image is given by $F_0 a_0/G$, where G and a_0 are the gain in ADU/e^- and a scale factor in the kernel respectively. Then the electron signals were simulated randomly following a Poisson distribution with the mean value of $F_0 a_0/G$. The resultant simulated random electron signals were rescaled back to the reference image in ADU by multiplying by G/a_0. Actually the differential flux $\Delta f_i(t)$ of the ith pixel is given by

$$\Delta f_i(t) = \frac{Poisson(\frac{PSF_i f_{0,i} A(t) a_0}{G})G}{a_0} - PSF_i f_{0,i} A(t_{ref}), \tag{8.1}$$

where $Poisson(f_{mean})$ means the random value following a Poisson distribution with the mean value of f_{mean}. PSF_i and $f_{0,i}$ are ADU flux in the ith pixel of the normalized PSF and unamplified source.

The photon noise from the sky background, the blending of stars and the wings of nearby stars in the current image and reference image are already included in the real

subtracted images. Furthermore the systematic noise from the poor subtraction due to the low S/N is also included. These noise sources heavily depend on the sky condition, seeing, tracking of the telescope and star density of each frame. So it is difficult to simulate with full artificial images.

We cut off the 23×23 pixels of small subimage from the subtracted image at a randomly selected position, and put the corresponding $\Delta f_i(t)$ onto each pixel of this small subimage. Sample of the cut raw subtracted image (left panel) and the generated artificial differential image (right panel) are shown in Figure 8.2.

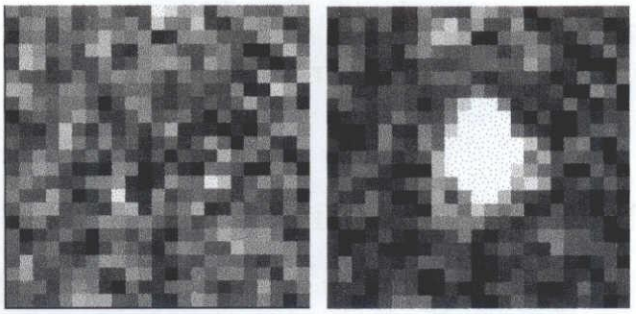

Figure 8.2: A sample of a cut raw subtracted sub image (left) and an image with artificial event (right). They have 23×23 pixels.

For a series of generated artificial images, we applied the same variable object detection process as in section 5.3 to check whether these objects could be detected or not in each frame. And the PSF photometry was applied using the same procedure as in section 5.4. Where the pixels had ADU values which were too high ($> 30,000$ ADU) these were rejected in the analysis, as the real analysis also did. The results of the detection process and photometry in each frame were stored in the database of artificial events.

Sample of the light curves of these artificial events are shown in Figure 8.3.

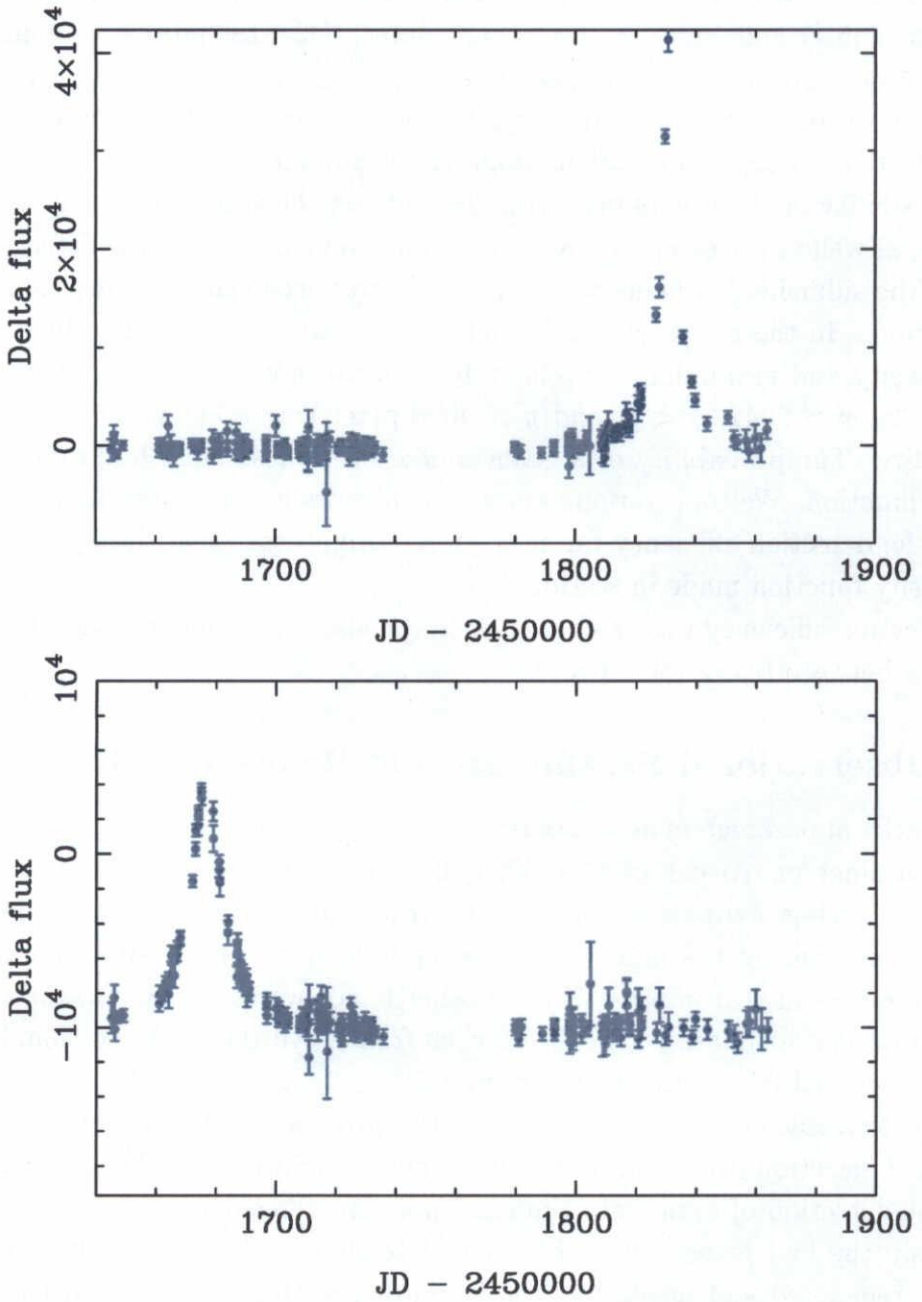

Figure 8.3: Samples of the light curves of artificial microlensing events with $t_E = 20$ days and $I_0 \sim 17$.

8.2.2 Event Parameters

Here we summarize specific details of the parameters used in this simulation.

The parameters which follow the well known simple distribution were selected at random. The times of peak magnification t_0 were taken to lie between the first observation date (JD2451645.1) and the last observation date (JD2451863.9) at random following a flat distribution. The minimum impact parameter u_{min} came from the simple geometry between the lens trajectory and source position, so, u_{min} must follow a uniform distribution too. We selected the u_{min} values at random between 0 and 1.

The possibility of the events occurring depends on the star density and the extinction due to dust, as well as the sampling rate and so on. So we estimated the detection efficiency for each of the subfields (14 fields $\times$ 3 chips). We produced the event position (x,y) in the CCD at random in the range $36 \leq x \leq 2042$ pixels and $5 \leq x \leq 4090$ pixels because the the star density and extinction are relatively uniform in each subfield. The edges of the CCD ($x < 35$, $x > 2042$, $y < 4$, and $y > 4090$ pixels) were cut in this analysis because of bad quality. The probability of a given source brightness must be proportional to the luminosity function. We took various source magnitudes in a uniform distribution, and we estimated the detection efficiency for each source brightness, then these were weighted by the luminosity function made in section 8.1.

The detection efficiency was calculated with the above parameters as a function of event timescale t_E between $0.3 \sim 150$ days.

8.2.3 Observational Parameters and Realism of this Simulation

The observational parameters are more important to estimate the detection efficiency than the event parameters. Alcock et al. (2000a) have fully simulated many observational parameters, e.g., seeing, extinction, sample rate, star density, bad pixels and so on, by using estimated values during the analysis. However it is very complicated and there can be hidden parameters in real images. On the other hand, we used real subtracted images in this simulation and estimated the PSF on each frame. All these observational parameters are already included in real subtracted images.

The detection efficiency was determined by two process, i.e., the object detecting process and the event selection process from the photometric light curves. The components which obstruct the detection of events are time and position dependent.

Obviously the bad pixels affect the event detections. The bad pixels in the reference image were registered and masked at the beginning of this analysis, and the stars under these pixels are not counted in the star catalogue of our fields (see section 5.2.1). However the pointing of the telescope slightly varies for every frame. The offsets are about some tens of pixels. Because of this shift, other stars were affected by bad pixels, and some stars near the edge of CCD chip were not observed. The effects of bad pixels and of the edge of CCD chip caused by the variation of the pointing of the telescope in each frame are included in the real images. The saturated stars were masked after the image subtraction by mask images which were made in section 5.2.1. But stars which are too bright are not

masked completely and their wide tail and the leak lines of photo-electrons vary depending on various conditions, e.g., the brightness, seeing and sky background. In these regions the detection of the events becomes very difficult. This effect is also included in this analysis. We also took into account the case that the artificial event saturates because of its high amplification.

There are ($500 \sim 2,000$) variable stars in each our GB subfields. Obviously at the position near the variable stars the detection efficiency deteriorated, and only high S/N events could be detected. This effect is small $< 2\%$, but was included in this analysis. We didn't take into account the case that the source star is variable, because this possibility is very small ($< 0.01\%$).

The detection efficiencies also depend on the sampling rate of each field, which changes due to the weather, the duration of the night, the instrumental condition, the position of the target and the observation priority. By using real images, the sampling rate is completely the same as for real observations.

The photometric uncertainty can be a strong determinant of whether an event is detected or not. The photometric uncertainty is affected by photon noise in the region where the PSF fitting is performed. The photons from the blending and nearby stars depend on the stellar density at this position and the distribution of the photons of each star (i.e. the PSF). The variation of the seeing, the focusing, and the tracking accuracy of the telescope in each frame affect the distribution of photons from these background stars. These variations of the PSF and the stellar density are reflected in the real images. And the contributions from the sky background are significant to the photon noise which changes from $2,000 \sim 10,000$ ADU depending on the time during the night, the relative position and the phase of the Moon, the aurora and other unknown components. The photon noise from the sky background level was included in the subtracted images.

The variation of degree of transparency due to the atmosphere also affects the photometric uncertainty. This has a well known relation with airmass, but is also affected by the amount of atmospheric dust and the presence of thin patchy clouds. These effects are calibrated by the scale factor a_0 in the kernel function of each subframe (see section 5.2.3), and the variation of noise is scaled by this factor (see section 5.4 and 8.2.1) in the subtracted images. We observed the targets even under relatively bad conditions if the star can be seen. If the condition of each frame was too bad due to thick cloud, too high a sky background or too bad seeing, then the DIA analysis failed. In this case these frames were rejected in the analysis, and this affects the sampling rate instead of the photometry.

It is well known that the PSF shape can vary across the focal plane of a telescope because of irregularities in the optics and poor focus (Tomany & Crotts 1996). This effect is stronger near the edges of an image. Here the subtraction is poorest and the systematic residuals can be seen in the subtracted images (Alcock et al. 2000a). Our spatial variational kernel can correct this effect. However if this effect is too much, the small systematic residuals can be seen in the subtracted images. If this effect exists, it must be included in the real subtracted images. The quality of our DIA is very good, however there are systematic residuals some of which can be seen in the subtracted images. These residuals appear

depending on the S/N of the current images. The systematic residuals of subtraction also come from the differential refraction, which is mainly dependent on the color of the stars and the airmass. These systematic residuals are contained in the subtracted images.

The other sources of noise which reduce the accuracy of photometry or lead to spurious detections, such as cosmic rays, satellite tracks and asteroids are also included in these images. And any other unknown systematic noise sources are also completely simulated. Though the possibility that the real microlensing events in the real subtracted images affect the artificial events is very small, this is of course also included. We list all the properties of our simulations as follows.

Event parameters which we generated as artificial events:

- Time of peak magnification t_0 (random between JD2451645.1 $\sim$ JD2451863.9)
- The minimum impact parameter u_{min} (random between $0 \sim 1$)
- Position (x, y) in the field. (random between $36 \leq x \leq 2042$ pixel and $5 \leq x \leq 4090$ pixel)
- Baseline source flux f_0 (following the luminosity function)
- Event timescale t_E (Variable of the efficiency function, taken between $1 \sim 150$ days)
- Photon noise from additional flux (random following the Poisson statistics).

Observational parameters which were automatically simulated in the real subtracted images:

- Position of bad pixels (depending on pointing)
- Position of edge of CCD (depending on pointing)
- Effect of variable stars
- Effect of saturated stars
- Effect of real microlensing events
- Sampling rate
- Background star density at the position of event
- Seeing
- Focusing
- Tracking of the telescope
- Sky background

- Transparency due to the atmosphere (included in kernel coefficient a_0)
- Clouds
- PSF variation due to the position in the focal plane
- Differential refraction (depending on the color of star and the airmass)
- Systematic residuals in DIA
- Cosmic rays
- Satellite tracks
- Asteroids.

Analytic parameters which were simulated in analysis:

- Luminosity function (estimated by MOA + HST)
- Reddening due to dust in the Galactic bulge (estimated from CMD)
- Differential flux (calculated)
- Quality of reference image
- Uncertainty in differential flux
- Detection threshold (same as in real analysis).

8.3 Detection Efficiencies

In each of our 42 (14 fields $\times$ 3 chps) subfields, the density of stars, sampling rate, and observational condition are different. So, to determine the total optical depth towards the 14 Galactic bulge fields, we estimated the detection efficiencies individually for each of the 42 subfields. We show the resultant detection efficiencies as a function of the event timescale, the source magnitude and the minimum impact parameter.

8.3.1 Detection Efficiency as a function of Event Timescale

We show one of the resultant detection efficiencies as a function of the event timescale t_E in Figure 8.4. Here the dashed line indicates the event detection efficiencies for bright stars ($I_0 \sim 14$) as a source of the event, and the solid line represents the total event detection efficiencies for all possible sources ($I_0 < 23$). The differential flux ΔF due to microlensing is proportional to the baseline flux of the source star F_0. So, for the events with bright source stars, a large variation of flux ΔF is generated even with a small amplification due to microlensing. These events are only slightly influenced by the background noise from

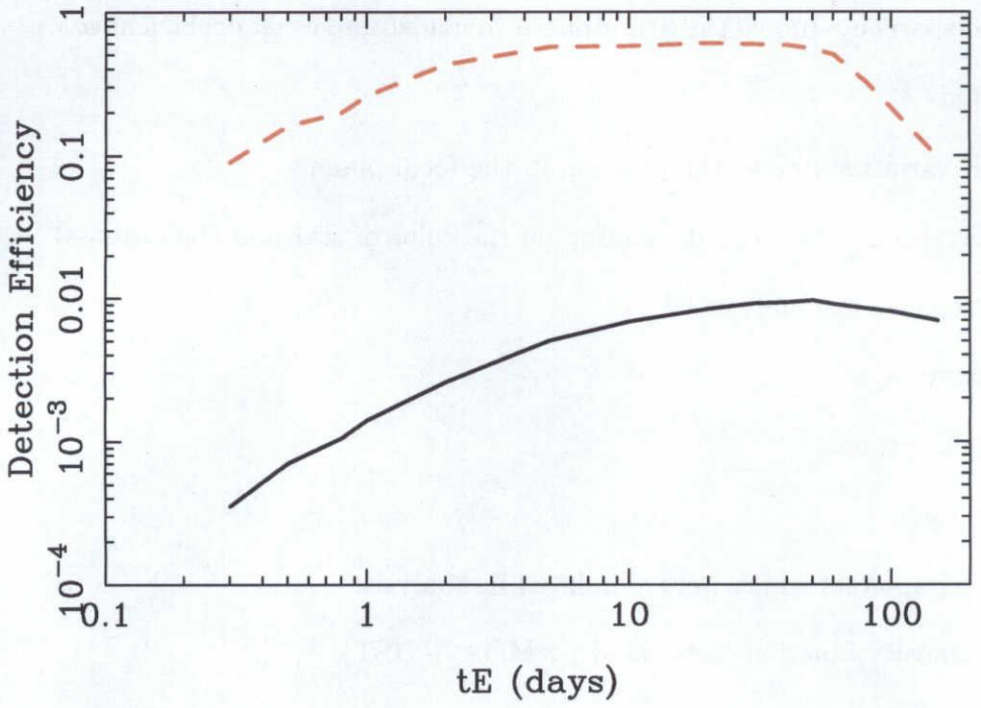

Figure 8.4: MOA detection efficiency as a function of event timescale for the ngb1-2 subfield. The solid line indicates the total detection efficiency for all source stars down to $I_0 = 23$, and the dashed line indicates the efficiency for bright sources $I_0 = 14$. The efficiencies slightly differ for each subfield because of differences in the sampling rate, the star density and the reddening.

blending stars and sky. As clearly seen in Figure 8.4, most events with bright source stars whose timescale is longer than 1 days can usually be detected.

On the other hand, the total event detection efficiencies (solid line, $I < 23$) are very low. This is because most source stars are fainter than our observational limiting magnitude ($I \sim 17$) as shown in Figure 8.1. These faint source stars are usually not visible at the baseline. Only when these sources are highly magnified over the background noise level, can this be detected as a microlensing event. The possibility that such a high magnification (i.e. small impact parameter u_{min}) event occurs is small because the distribution of impact parameters is flat. For example, to magnify the source star with $I \sim 20$ to 17, u_{min} should be smaller than 0.06 (see equation (2.27)). The probability of this is only 6% of that with the normal event detection criteria defined as $u_{min} < 1$. So the resultant distribution of the minimum impact parameter u_{min} in the detected events is no longer uniform. Of course, the real detection efficiency heavily depends on the event timescale. Such faint source events can not be detected any more for shorter timescale events.

8.3.2 Detection Efficiency as a function of Source Magnitude

We present the detection efficiencies as a function of the I-band magnitude of source stars for various event timescales in Figure 8.5, where I-band magnitudes are extinction corrected to match those of the HST field ($A_I = 0.742$). The efficiencies are very high for brighter source events, as expected. One can see the fall off at the bright end of this efficiency curve. This is due to the saturation of the source stars. Such bright source stars are easily saturated with relatively low amplification due to microlensing. In this case the photometry becomes unreliable and not well fitted by a microlensing light curve. The fact that this effect appears in our simulation is one of the pieces of evidence that this simulation is proper. On the other hand efficiencies fall off to fainter stars, because these require a high amplification in order to be detected. The maximum of our detection efficiency is not so high, even for bright source events, because our data have a gap for ~ 40 days due to our camera system not functioning.

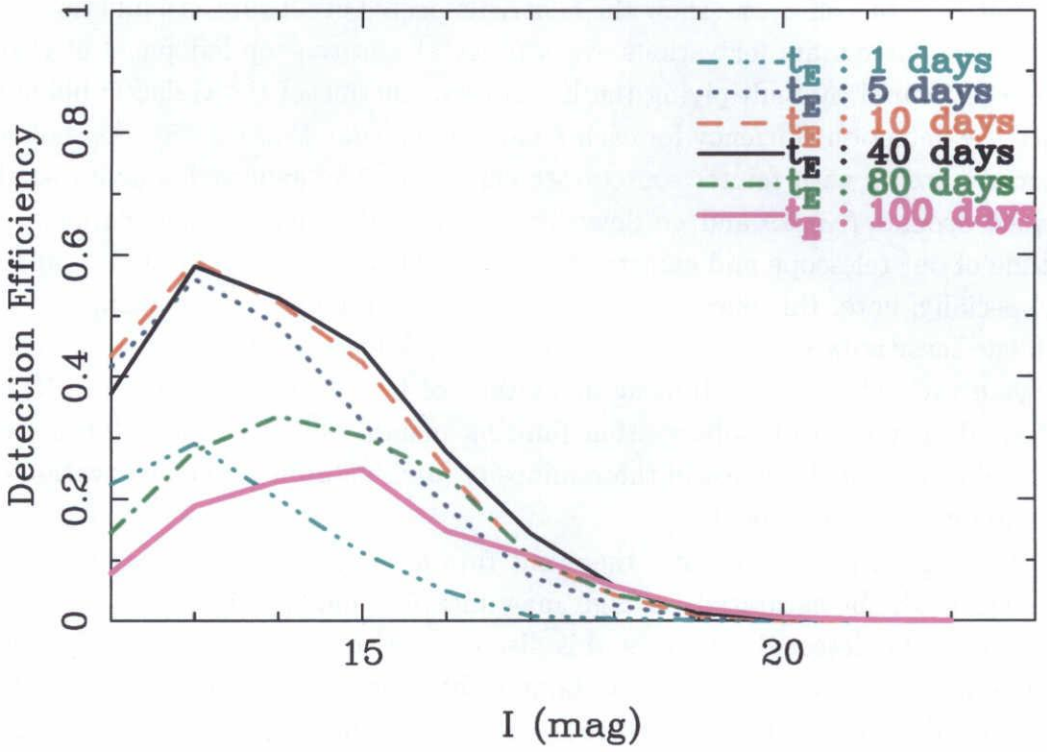

Figure 8.5: MOA event detection efficiencies as a function of source I band magnitude for the ngb1-2 subfield. The various lines indicate the efficiency for the event timescales of $1, 5, 10, 40, 80, 100$ days as indicated in the figure.

Comparing each of the timescales, for the longtime scale events, the efficiency falls off more significantly than that of the shorter timescale events at the bright end of these curves. This is because the number of saturated points is large and we required a stable flat baseline to identify the event. In the long timescale events ($t_E > 50$ days), the stable flat baseline in the light curve is very short. These effects are significant for brighter source

and longer timescale events. On the other hand, this effect is small for the fainter source and the shorter timescale events, because they have enough baseline and a low possibility of being saturated. Meanwhile, at the faint end, the efficiencies are inverted compared to those at the bright end. For long timescale events the duration with a significant excess in the light curve is longer than that of shorter timescale events. So, the short timescale events can not be detected any more, because we required more than three consecutive excess points to the events (see section 6.1).

These efficiencies falls off towards fainter end, as we explained above. However this fall off is fainter than the luminosity function from MOA data shown in Figure 8.1. We note there is a small but still adequate efficiency down to $I \sim 22$. For other fields, these efficiencies are similar, but some of them go slightly fainter than $I > 22$ for low extinction fields. This is the main improvement in the analysis by changing from DoPHOT-type analysis to DIA. In DoPHOT analysis, there is no detection efficiency for those source stars not resolved in the reference image.

To emphasize this effect, we show the relative expected event rate as a function of I-band magnitude of source stars for various event timescales in the top-left panel of Figure 8.6. These are estimated by multiplying the luminosity function of the Galactic bulge (Figure 8.1) with the detection efficiency for each I band magnitude (Figure 8.5). As shown in this figure, many events with fainter sources are expected. The expected source distributions are peaked around $I \sim 19$ and go down to $I \sim 22$, although the observational limiting magnitude of our telescope and camera is $I \sim 17$. This does show a dramatic capability of DIA. Especially, note, this effect was increased by our highly frequent sampling strategy. Though the sensitivity of the MACHO group (Alcock et al. 2000a) became 2 magnitudes deeper than their observation limiting magnitude of $V \sim 21$ by DIA, that of MOA is ~ 5 magnitude deeper than our observation limiting magnitude of $I \sim 17$. (Of course, this effect also depends on the shape of the luminosity function around the observation limiting magnitude for each experiment.)

For the longer timescale events, the event rate for bright stars decreases, because the source stars might be saturated for high magnification and we required a stable baseline for the event to be detected. However this distribution could reach to much fainter source stars. The longer the timescale is, the fainter the source events that could be detected. And the second peak seen around $I \sim 15$ is due to red clump giants which can also be seen in the luminosity function (see Figure 8.1).

In the top-right panel in Figure 8.6, the observed I-band baseline magnitude I_0 distribution is shown as the histogram with corresponding expected event rates scaled to match the histogram. Here the observed I-band baseline magnitude I_0 is de-reddened to match that in the HST field. The expected and observed distributions are in good agreement for the observed t_E range ($5 < t_E < 100$ days).

As mentioned in section 6.1.3, many possible microlensing events failed to be recorded by the criterion of $t_E < 200$ days in cut3. These events have a significant increase in the Δ flux, but their parameters could not be well constrained, because the light curve was measured only around the peak. In such events u_{min} and t_E would be degenerate. If the

baseline flux is measured by the follow-up observations, this degeneracy could be broken. If we have made the catalogue of all variable stars and novae from some years observations, as now we are doing, or if we take the data with both Red and Blue colors, we could easily identify the real microlensing events and issue alerts for these faint source events, without the criterion of $t_E < 200$ days.

We show the expected event rates without the cut of $t_E < 200$ days in the bottom-left panel of Figure 8.6. In this figure we can see a significant increase of the expected event rate for the longer timescale events with the dimmer source stars. These dim source star events intrinsically should have high amplification. We can see this effect in the minimum impact parameter distribution for each of the cases in the following section 8.3.3. On the other hand, no significant change can be seen for the short timescale events, though the duration of the excess in the light curve of these events are as short as that of the events of a longer timescale but with faint source stars. So, the efficiency for the short timescale events is not affected by this criterion.

To compare these results with the traditional DoPHOT-type analysis, we show the same distributions by using only the MOA luminosity function (filled circle points in Figure 8.1) as the source luminosity distribution in the bottom-right panel of Figure 8.6. This reflects the same situation as with the DoPHOT analysis, in which the source star should be resolved in the reference image. This is not the real source magnitude distribution obtained by DoPHOT analysis, because the DIA can improve the photometric accuracy, even for stars resolved in the reference image. Furthermore there are many faint source events which are blended by bright resolved stars. These effects will cancel each other. Anyway, these are relatively smaller effects than the difference in DIA and DoPHOT analysis. So this distribution, shown in the bottom-right of Figure 8.6, should not be so much different from the actual one and good to be compared.

In this figure, the difference from DoPHOT (bottom-right) to DIA (top-left) is clear. The peak of this distribution is at $I \sim 15$, which corresponds to the second peak in the top-left panel of Figure 8.6 due to red clump giant stars as the source stars. The DIA method increases the number of events by more than a factor of 2. In particular we can detect many events in which the source stars are fainter than the observation limiting magnitude by using DIA.

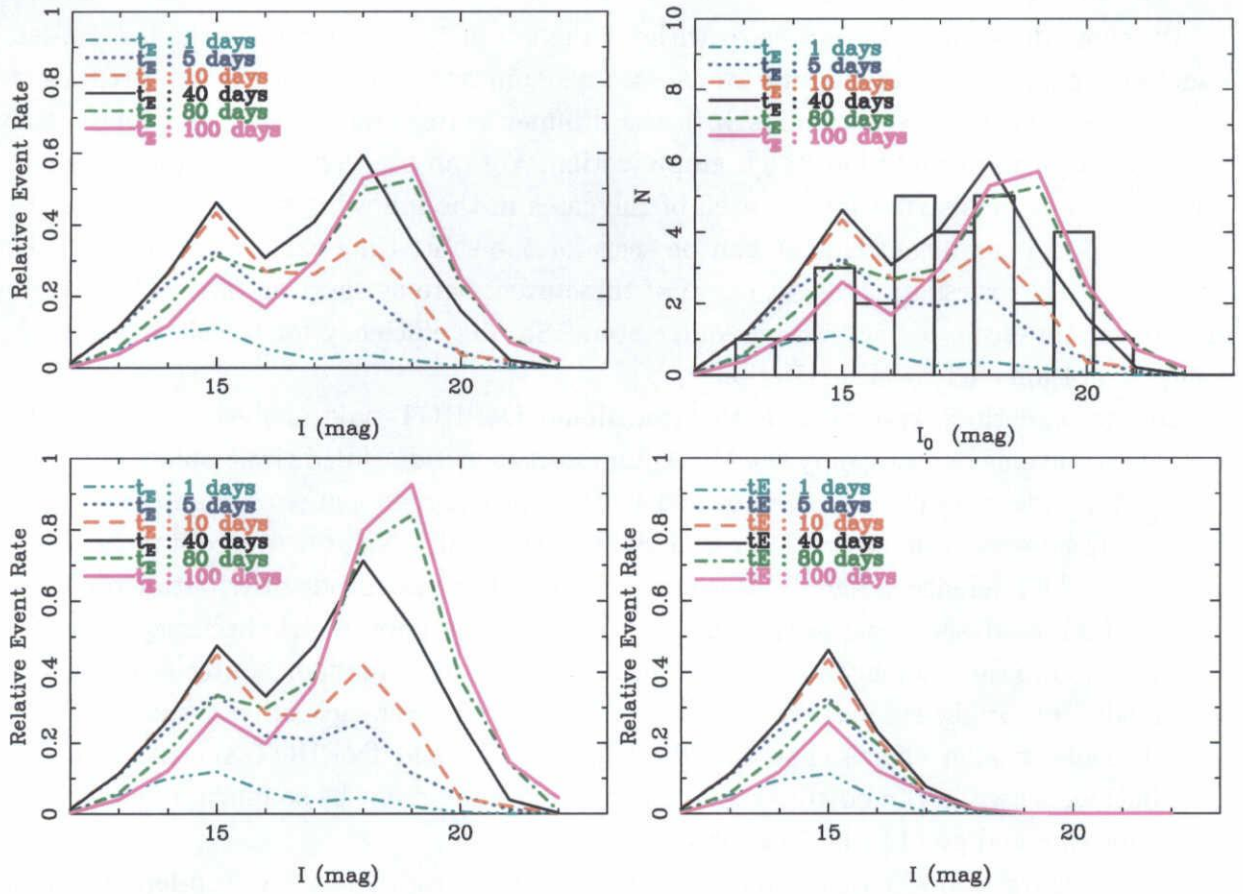

Figure 8.6: Expected relative event rates as a function of source I band magnitude. Top-left: Expected event rates in this analysis. Top-right: Histogram of the observed I-band baseline magnitude I_0 with corresponding expected event rates scaled to match the histogram. The expected and observed distributions are in good agreements for the observed range of t_E ($5 < t_E < 100$ days). Bottom-left: Expected event rates without the cut of $t_E < 200$ days in cut3. A significant increase can be seen for the longer timescale events with the dimmer source stars. Bottom-right: Expected event rates for the case that the sources are only resolved stars in the reference image. This corresponds to the event rate by DoPHOT-type analysis. Of course this is not real, but not is so different. This is shown in comparison with that by DIA. The various lines indicate the relative event rates for the event timescales of $1, 5, 10, 40, 80, 100$ days as indicated in the figure.

8.3.3 The Minimum Impact Parameter Distribution.

Because of the simple geometry of microlensing, the probability distribution of the minimum impact parameter u_{min} is uniform. However, in actual experiments, the detection efficiency heavily depends on u_{min}. The smaller the impact parameter, the higher the source will be amplified. The high amplification makes it easier to detect the events because of their high S/N, especially those events with faint sources require a high amplification to be detected. Hence the distribution of the minimum impact parameter would be biased towards smaller impact parameters.

This effect can be seen in our observed minimum impact parameter distribution (histogram) and the estimated detection efficiencies in the simulation (lines) as a function of u_{min} for various timescales which are scaled to match to the histogram as shown in Figure 8.7. Here the lines are the mean efficiencies for all our fields. These detection efficiency distributions from the simulation are equivalent to the expected event distribution because the real u_{min} distribution is flat. These observed and estimated distributions are in good agreement for the range where the observed timescales are founded (between $10 \sim 100$ days, see section 8.5).

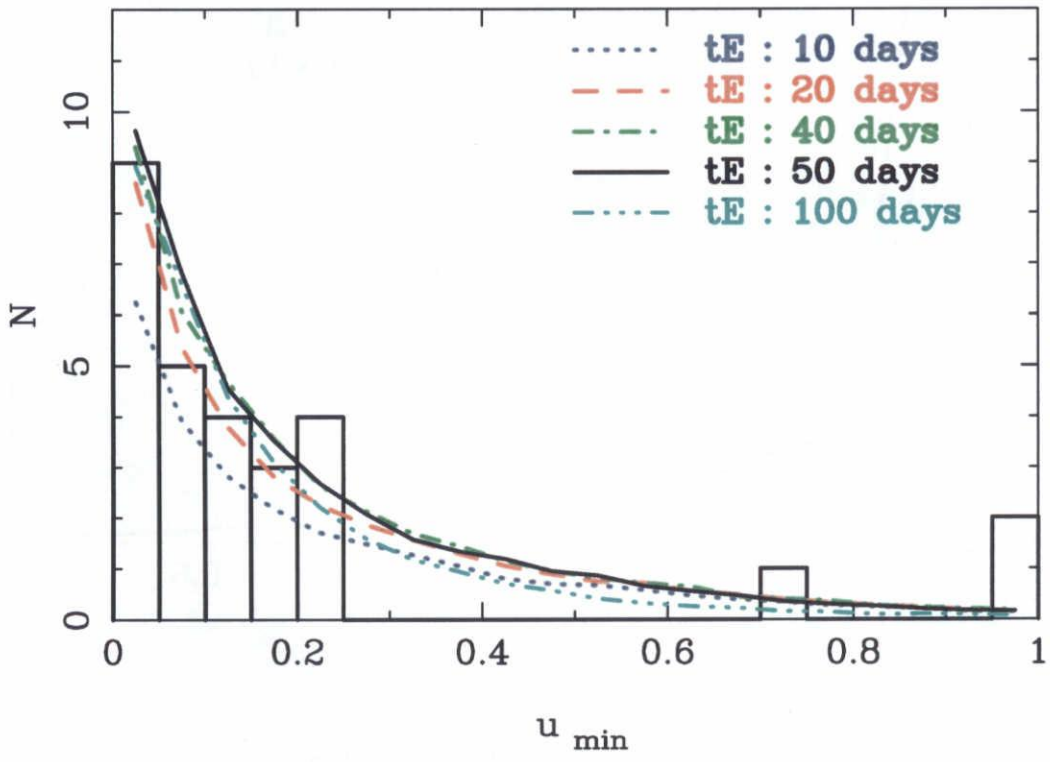

Figure 8.7: Observed minimum impact parameter u_{min} distribution (histogram) and the MOA event detection efficiency distributions as a function of u_{min} scaled to match the histogram. The various lines represent the efficiency for the event timescale of $10, 20, 40, 50, 100$ days as indicated in the figure.

In this distribution we can see that half of the detected events have a small minimum

impact parameter ($u_{min} < 0.1$), though the fraction of events with $u < 0.1$ is only 10% in the DoPHOT analysis of the MACHO group (Alcock et al. 1997a) and 30% in the recent DIA analysis of the MACHO group (Alcock et al. 2000a). This is because our sampling rate is higher ($5 \sim 6$ times/day) than that of the MACHO group (once per day).

As mentioned in section 6.1.3, many possible microlensing events failed to be detected by the criterion of $t_E < 200$ days in cut3. These events have a significant increase of the Δ flux, but parameters could not be well constrained because the light curves are measured only around the peak. In such events u_{min} and t_E would be degenerate. If these events are included as mentioned in the previous section, then $5 \sim 15\%$ more high magnification events would be expected, because the source stars of such events are very faint (see section 8.3.2). We show the distribution of the mean detection efficiency in u_{min}, i.e. the expected event rate distribution, for the typical timescale of $t_E = 40$ days without this $t_E < 200$ days cut in Figure 8.8. To compare, we also show the u_{min} distribution with the t_E cut (the actual cut in this analysis as shown in Figure 8.7) and the same distribution for the events with brighter source stars ($I < 17$), which correspond to the DoPHOT analysis.

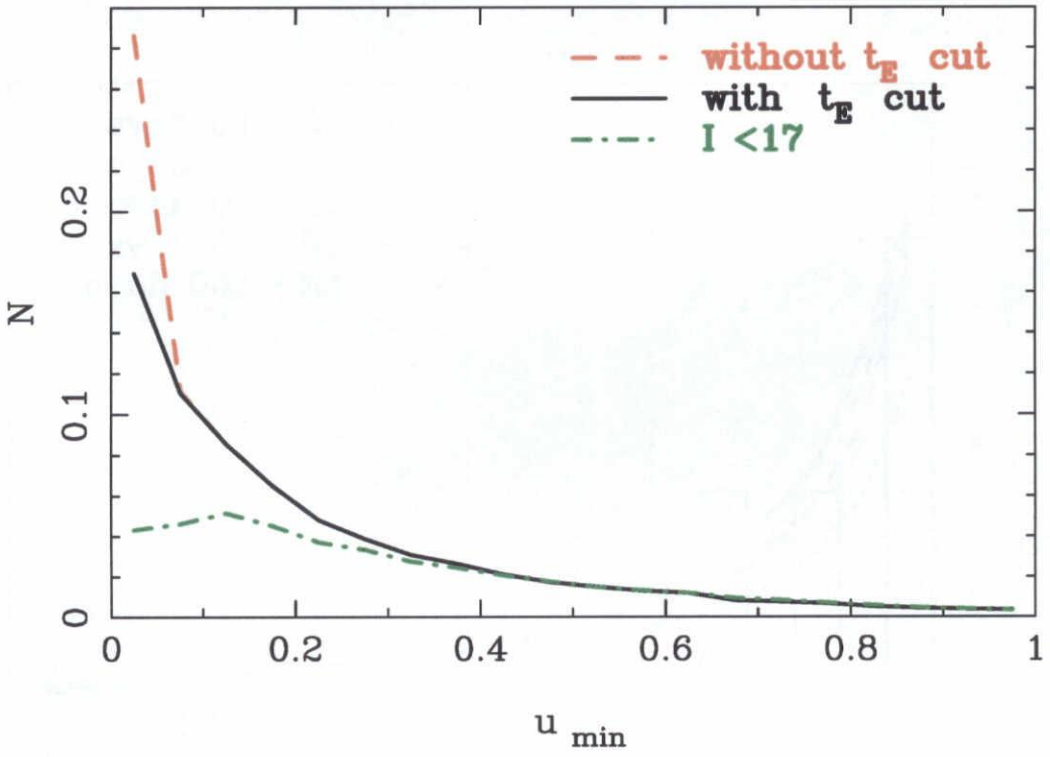

Figure 8.8: Event detection efficiencies as a function of u_{min} for the typical timescale of $t_E = 40$ days with the $t_E < 200$ days cut (solid line), and without $t_E < 200$ days cut (dashed line). The efficiency curve with the $t_E < 200$ days cut for the bright source star ($I < 17$) events (dot-dashed line), which is scaled to match the others at $u = 1$, is also shown for comparison.

From this figure, it is clear that our analysis with DIA (solid line) can detect the high magnification events more efficiently than a DoPHOT-type analysis, which correspond to

that for bright source events (dot-dashed line). In the curve for bright source events, the efficiency decreases for the highest amplification events. This is because of the saturation of source stars. While this effect is negligible in other two lines which include all faint source stars because the fraction of very faint source events is larger in these cases. Furthermore it will be possible to detect more ($\sim$ 10%) high magnification events without the $t_E < 200$ days cut (dashed line) in the near future.

8.4 Optical Depth

Here we estimate the optical depth towards the Galactic bulge by using the events detected in this analysis and our detection efficiencies. We have made a Monte Carlo simulation to estimate the uncertainties in the observed optical depth.

8.4.1 Optical depth Estimation

The optical depth is defined as the probability that any given star is microlensed with impact parameter $u_{min} \leq 1$ at any given time. The optical depth is independent of the mass of the lens object. So any information about the velocity distribution and mass function of the lens objects is not required. The optical depth from the event time scales of the observed events can be estimated by following equation:

$$\tau = \frac{\pi}{2N_s T_o} \sum_i \frac{t_{E,i}}{\varepsilon(t_{E,i})} \tag{8.2}$$

where N_s is the total number of source stars in the observation fields and T_0 is the duration of observation of this analysis in days. t_E is the event timescale (Einstein radius crossing time) for the ith event and $\varepsilon(t_{E,i})$ is the detection efficiency for a given timescale. To estimate N_s, we counted the number of bright stars ($I < 15$ which is de-reddened to match the HST field) whose observation efficiency is nearly 100%, and scaled by the ratio N_{23}/N_{15} where N_{15} and N_{23} are the number of stars in the range $I < 15$ and $I < 23$ respectively in our combined LF. This is because our detection efficiencies were estimated by taking all stars with $I < 23$ into account.

We estimated the optical depth by using the estimated timescales of detected events in Chapter 6 with $N_s \sim 250$ millison stars ($I < 23$), $T_o = 219$ days for ngb1 $\sim$ 12. We didn't include the ngb13 and 14 fields in this analysis because these two fields are far from Baade's Window in which it is difficult to compare with other observations or models. Our estimated timescales in Chapter 6 are not biased as a result of the blending, because we used the DIA and not the DoPHOT, as mentioned in Alcock et al. (2000a). For events with timescales within $0.3 < t_E < 150$ days, we estimated the optical depth as

$$\tau_{0.3}^{150} = 2.62^{+0.72}_{-0.56} \times 10^{-6}, \tag{8.3}$$

where the lower and upper limit of this value were estimated by a Monte Carlo simulation as discussed in the following section.

This optical depth is mostly due to disk and bulge (bar) stars. The optical depth in the direction of the Galactic bulge due to halo objects of any kind is only $\sim 0.13 \times 10^{-6}$ (Griest et al. 1991), which in any case is much less than the contribution due to any disk or bulge models.

8.4.2 Uncertainties in the Optical Depth

The statistical uncertainties in the observed optical depth τ_{obs} were determined with the following procedure, which is same as used by the MACHO group (see Alcock et al. 1997a,b, 2000a). The uncertainty in the optical depth does not follow Poisson statistics. However, since the number of events still obeys Poisson statistics, it is straight forward to evaluate confidence level limits by using Monte Carlo simulations. We have simulated "experiments" in which the number of detected events N is selected according to Poisson statistics with the mean of the number of expected events N_{exp}. In order to calculate the optical depth for a given simulation, each simulated event must also be assigned a timescale $t_{E,i}$ according to the assumed event timescale distribution. We randomly selected one of our measured event timescales for each simulated event. We simulated 50,000 experiments to make the distribution for each N_{exp}. For example, the simulated optical depth distributions with $N_{exp} = 20$ and 32 are shown in Figure 8.9. Here the mean optical depth of each distribution $< \tau(N_{exp}) >$ (dashed line) and the observed optical depth τ_{obs} (solid line) are also presented.

We estimated the probability $P(\tau(N) > \tau_{obs})$ that the optical depth $\tau(N)$ in each simulated experiment is larger than the observed optical depth τ_{obs} (i.e., the fraction of the right side relative to the solid line (τ_{obs}) in Figure 8.9) for each N_{exp}. This probability as a function of the mean optical depth $< \tau(N_{exp}) >$ of the experiments, in which the expected number of events is N_{exp}, allows us to estimate the statistical distribution of the optical depth. We estimated the 1σ confidence limit of the optical depth as the mean optical depth $< \tau(N_{exp}) >$ in which this probability is 15.85% (lower) and 84.15% (upper). We show this distribution with the observed optical depth τ_{obs} (solid line) and 1σ confidence limits (dashed lines) in Figure 8.10.

This procedure will underestimate the variance of the timescale distribution by a factor of $(N-1)/N$ because both the mean and variance are measured from the same data set (Alcock et al. 1997b). However we think this procedure gives a relatively reasonable error bar, because this is less dependent on theoretical models.

This optical depth is almost certainly underestimated because of the fact that some fraction of the source stars are foreground stars in the foreground disk, for which the optical depth is considerably lower.

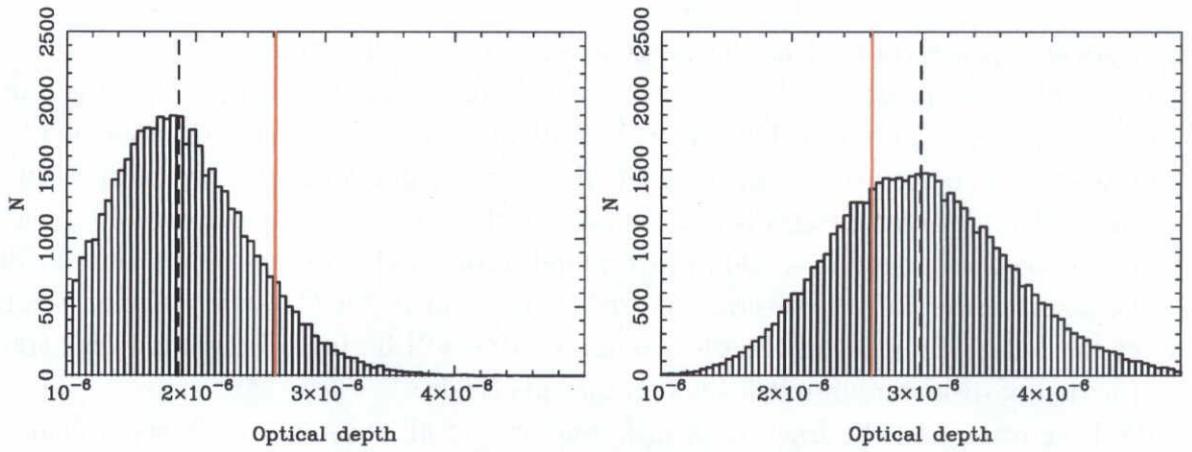

Figure 8.9: The simulated optical depth distribution with $N_{exp} = 20$ (left panel) and 32 (right panel). The mean optical depth of each distribution $< \tau(N_{exp}) >$ (dashed line) and the observed optical depth τ_{obs} (solid line) are also presented. 50,000 experiments were simulated for each distribution.

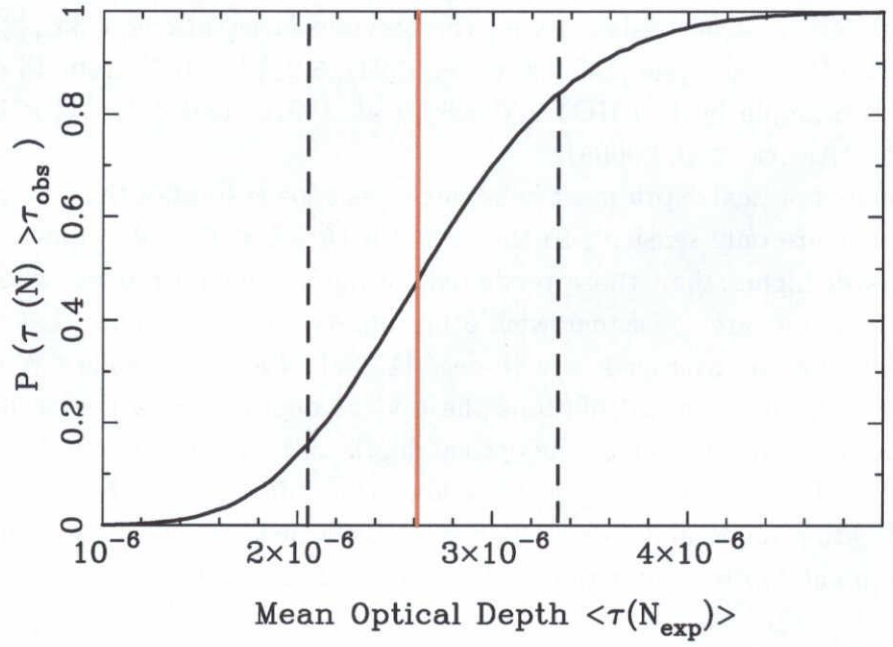

Figure 8.10: The probability $P(\tau(N) > \tau_{obs})$ that the optical depth $\tau(N)$ in each simulated experiment is larger than the observed optical depth τ_{obs} as a function of the mean optical depth $< \tau(N_{exp}) >$ of experiments in which an expected number of events is N_{exp}. This represents the distribution of statistical uncertainty in the optical depth from the Monte Carlo simulation. The 1σ confidence limits (dashed line) and the observed optical depth τ_{obs} (solid line) are also presented. 50,000 experiments were simulated for each distribution.

8.4.3 Disk Contribution

The optical depth estimated in the previous section is underestimated. In the number of stars monitored in our fields N_s, some fraction of the stars are probably foreground Galactic disk stars. The contribution to the optical depth due to the disk stars as a lens is not as small as described in section 2.3.4. However the optical depth for the disk source stars (so-called disk-disk events) is quite small. So the total optical depth would be lower. There are also background disk stars which would have a higher optical depth, but our line of sight towards the bulge is several hundred persecs out of the Galactic plane on the far side of the bulge. So most of the disk contamination will be from foreground disk stars. The fraction of disk stars in our fields is rather uncertain.

We have estimated the fraction of disk stars out of all stars in our observed fields as $f_{disk} \sim 23\%$ by using the standard double-exponential disk, the non-rotating triaxial bar models and Kiraga & Paczyński (1994)'s luminosity function (see section 8.5). This value is consistent with the value used by the MACHO group of $f_{disk} \sim 20\%$ (Alcock et al. 1997a) and $f_{disk} \sim 25\%$ (Alcock et al. 2000a), where most of our GB fields are overlapping with the MACHO group's fields. This gives

$$\tau_{bulge} = 3.40^{+0.94}_{-0.73} \times 10^{-6}[0.77/(1 - f_{disk})]. \tag{8.4}$$

This optical depth value is consistent with the previous observations of $3.3^{-1.2}_{+1.2} \times 10^{-6}$ from 9 events by DoPHOT analysis (Udalski et al. 1994), $3.9^{-0.9}_{+1.2} \times 10^{-6}$ from 13 events in the clump giant subsample by DoPHOT (Alcock et al. 1997a) and $3.23^{-0.50}_{+0.52} \times 10^{-6}$ from 99 events by DIA (Alcock et al. 2000a).

This measured optical depth must be regarded as a lower limit of the true value because our observations are only sensitive to the events with $0.3 < t_E < 150$ days. Nevertheless this value is still higher than those predicted by most Galactic models whose mass and inclination of the bar are consistent with other observations. We note that our observed optical depth values are averaged over 16 deg^2 (12 fields) around Baade's Window $(l, b) = (1°.0, -3°.9)$, while in most calculations the optical depth is estimated exactly towards Baade's Window. In most models, the optical depth averaged over our Bulge fields is very close to that at Baade's Window, so we ignore this difference in this paper. Even the smallest inclination angle and a large bar mass have been reported to be insufficient to produce an optical depth greater than $\sim 2.5 \times 10^{-6}$ (Peale 1998).

8.5 Timescale Distribution

The observed timescale distribution depends on the mass function and the velocity dispersion of the lens and source. To make the models of Galactic structure, both the optical depth and the timescale distribution should be consistent with the observations. Peale (1998) and Mera et al. (1998) show that it is difficult to reproduce the observed timescale distribution of Alcock et al. (1997a) with the existing Galactic models.

We show our observed timescale distribution in Figure 8.11. Our observed timescales are not biased by the blending, because we used the DIA not DoPHOT, as mentioned in Alcock et al. (2000a).

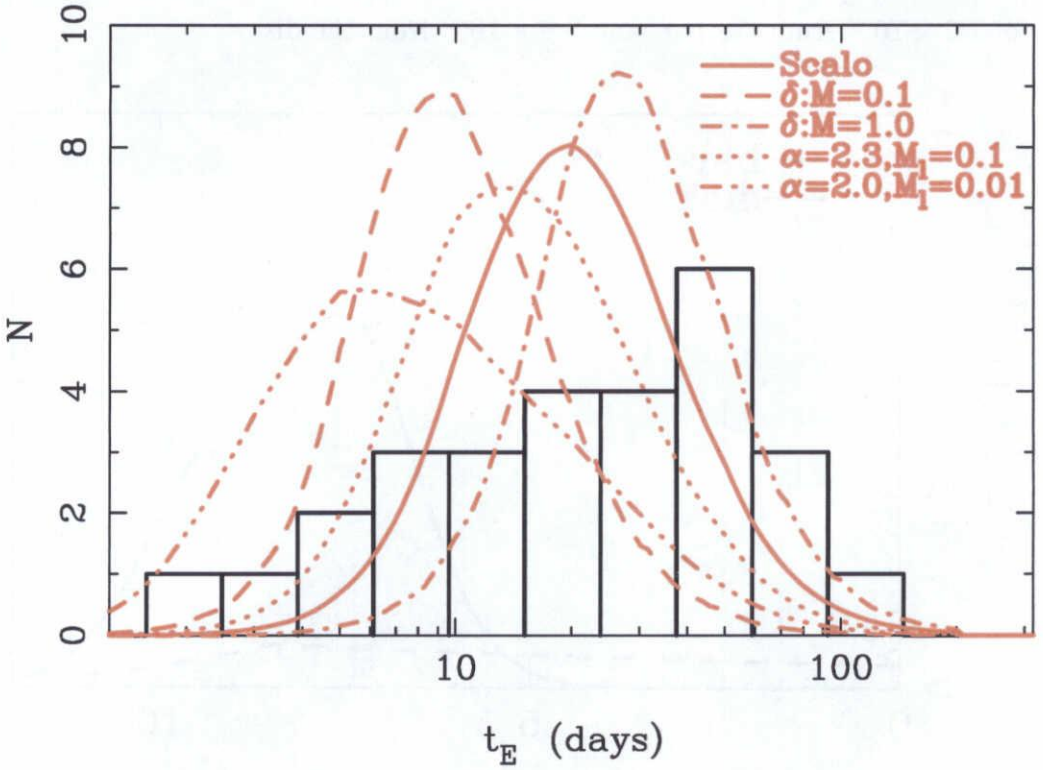

Figure 8.11: Histograms of the event timescale t_E distribution for 28 observed events with expected timescale distributions, normalized to the observed number of events, for a fixed bar and disk density model and for various mass functions. The solid line indicates (i) Scalo (1986)'s PDMF; the dashed and dot-dashed lines indicates δ function (ii) at $M = 0.1M_\odot$ and (iii) at $M = 1.0M_\odot$ respectively; the dotted and three dot-dashed lines show the power-law (iv) with $\alpha = 2.3$, $M_l = 0.1$ and (v) with $\alpha = 2.0$, $M_l = 0.01$, where the later one represent the brown dwarf rich mass function.

To be compared, we also plotted the expected timescale distribution for a fixed bar and disk density model with various mass functions in Figure 8.11. These distributions are corrected by our detection efficiencies and normalized to the number of observed events. We used the Han & Gould (1995a)'s models, i.e., a triaxal bar model given by equation

(2.21) with the bar inclination angle of $\theta = 20°$, and a double-exponential disk model with a density profile given by

$$\rho_d = \rho_{d0} exp\left(\frac{-|z|}{h_z} - \frac{R - R_0}{R_d}\right), \tag{8.5}$$

where $R = R_0^2 + D^2 \cos^2 b - 2R_0 D \cos b \cos l$ and $z = D \sin b$ are the disk cylindrical Galactocentric coordinates, D is the distance from the Sun and (l, b) are the Galactic latitude and longitude. $h_z = 325$ kpc and $R_d = 3.5$ kpc are the disk scale height and length, $\rho_{d0} = 0.06 M_\odot$ is the density constant chosen to match the density in the solar neighborhood. We show the density profile of these bar and disk models towards Baade's window at $(l, b) = (1°, -3°.9)$ in Figure 8.12. These models give optical depths towards Baade's window of 1.2×10^{-6} from the bar, and 0.6×10^{-6} from the disk.

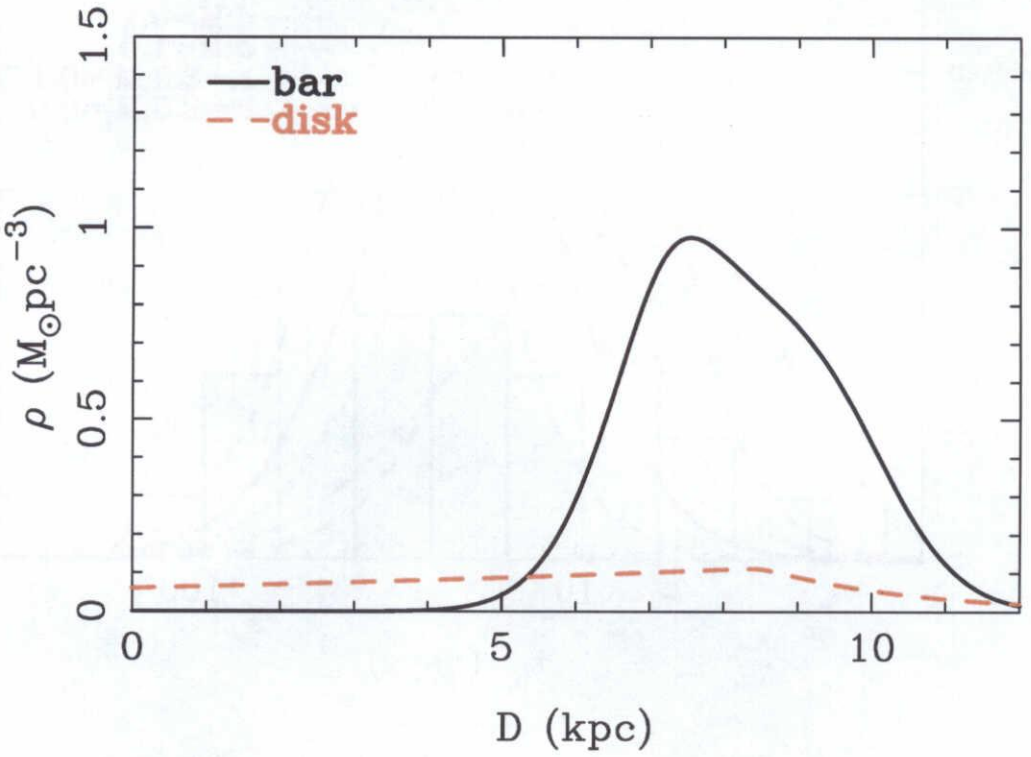

Figure 8.12: The density profile of the bar (solid line) and the disk (dashed line) models used in this analysis.

Following Kiraga & Paczyński (1994) and Han & Gould (1995a), the event rate in the case that both the source and lens are bar stars, Γ_{bar}, is given by

$$\begin{aligned}\Gamma_{bar} &= 4\sqrt{\frac{G}{c^2 M}}\left[\int_0^\infty dD_s n(D_s)\right]^{-1} \int_0^\infty dD_s n(D_s) \\ &\int_0^{D_s} dD_d \rho_b(D_d) \sqrt{\frac{D_d(D_s - D_d)}{D_s}} \int dv v f(v),\end{aligned} \tag{8.6}$$

where $n(D_s)$ is the number density of source stars. As the distance from the observer increases, the volume element and the total number of stars in the element increase. However, the actual number of stars one can detect decreases with increasing distance because of the detection limits. In our computation, we assumed that these two factors cancel out (Han & Gould 1995a). This is equivalent to the $\beta = -1$ model of Kiraga & Paczyński (1994), and then $n(D_s) \propto \rho_b(D_s)$. And v is the transverse velocity and $f(v)$ is its distribution.

On the other hand, for the events lensed by the disk stars, the source bar stars are located within a narrow region compared to the typical values of D_d and $D_s - D_d$ of disk lenses. Therefor D_s could be approximated as a fixed distance of $D_s = R_0 = 8.5$ kpc. Then the event rate is given by

$$\Gamma_{disk} = 4\sqrt{\frac{G}{c^2 M}} \int_0^{D_s=R_0} dD_d \rho_d(D_d) \sqrt{\frac{D_D(D_s - D_d)}{D_s}} \int dv v f(v). \tag{8.7}$$

The events in which the disk stars are lensed by disk stars, so-called disk-disk lensing, is negligible.

The transverse velocity v is defined as

$$v = v_d - \left[v_s \frac{D_d}{D_s} + v_o \frac{D_s - D_d}{D_s} \right]. \tag{8.8}$$

where v_d, v_s and v_o are the transverse velocities of the lens, source and observer, respectively. We assume that the velocity distribution for each component of lens and source are represented by a Gaussian as $f(v) = f(v_{d,y}) f(v_{d,z}) f(v_{s,y}) f(v_{s,z})$, where

$$f(v_i) = \frac{1}{\sqrt{2\pi\sigma_i^2}} exp\left[-\frac{(v_i - \bar{v}_i)i^2}{2\sigma_i^2} \right]. \tag{8.9}$$

Here $\bar{v}_i$ is the mean velocity of the ith component. We adopt $(\bar{v}_{bar,y}, \bar{v}_{bar,z}) = (0,0)$ and $(\sigma_{bar,y}, \sigma_{bar,z}) = (110, 110)$ for the bar lens and source, $(\bar{v}_{disk,y}, \bar{v}_{disk,z}) = (220, 0)$ and $(\sigma_{disk,y}, \sigma_{disk,z}) = (30, 30)$ for the disk lens, $(\bar{v}_{o,y}, \bar{v}_{o,z}) = (220, 0)$, $(\sigma_{o,y}, \sigma_{o,z}) = (0, 0)$ for the observer in km/s (Han & Gould 1995a; Alcock et al. 2000a).

For these bar and disk models, we evaluated timescale distributions towards Baade's window with the following five mass functions: (i) Scalo (1986)'s Present Day Mass Function (PDMF), a δ-function (ii) at $M = 0.1 M_\odot$ and (iii) at $M = 1.0 M_\odot$, and the power-law $\phi(M) \propto M^{-\alpha}$ (iv) with $\alpha = 2.3$ and the low mass end $M_l = 0.1 M_\odot$, (v) with $\alpha = 2.0$ and $M_l = 0.01 M_\odot$, where the function (v) represents the brown dwarf rich mass function (Alcock et al. 1997a). Results are shown in Figure 8.11.

The timescale of detected events is distributed in the range $5 < t_E < 100$ days and centered around $t_E \sim 30$ days. This feature is consistent with the timescale distribution from the MACHO group (Alcock et al. 2000a) though their distribution is slightly sharper around the mean than ours. The distribution of Alcock et al. (2000a) is well fitted by the timescale distribution expected from the Scalo (1986)'s PDMF except for some fraction of long timescale events, though those models do not explain the large observed optical depth. For our distribution in Figure 8.11, Scalo (1986)'s PDMF also seems to be more

reasonable than the others. Although our detection efficiency is sufficiently high for the short timescale events ($t_E \sim 0.3$ days) because of our frequent sampling ($5 \sim 6$ times/day), there are only two short timescale events ($t_E < 4$ days). The short timescale events could be produced when the lenses are either near the observer or the source. However, this effect is relatively small unless the distance from the lens to the source or to the observer is very small. So the timescale distribution traces the mass distribution. The timescale t_E for the most common events is $\sim 7(M/0.1M_\odot)^{1/2}$ days for both bulge and disk lenses (Han & Gould 1995a). The number of observed short events is much smaller than that expected from the brown dwarf rich mass function (v). This implies that there is no large population of small lenses such as brown dwarfs along the line of sight towards the Galactic bulge, as described in Alcock et al. (2000a).

We can also see some fraction of long timescale events ($t_E > 70$ days) as reported in Alcock et al. (2000a), which can not be reproduced with Scalo (1986)'s mass function (i) and the contemporary Galactic models (Han & Gould 1996). Such long timescale events could be produced when the lenses are heavy, moving at low transverse velocity, or in the middle of the line from observer to source. If both the lens and source are in the disk, so called disk-disk lensing, then the timescale would be long. The probability of this is constrained by star counts, and it is very small. The effect of geometry is relatively small (factor ~ 2). There might be some unknown population of dynamically cold or massive dark objects, such as white dwarfs or neutron stars in the Galactic disk or bulge. More discussion on this can be seen in Alcock et al. (2000a).

We show our observed timescale distribution, corrected by the detection efficiency, i.e., the expected true t_E distribution, as is also given in Figure 8.13. This distribution is similar to that from the MACHO group's observations (Alcock et al. 2000a) except the part for the short timescale events. Though their distribution is sharply truncated at $t_E \sim 4$ days except for one short event with $t_E = 1.4$ days, our distribution is flat to 2 days. However this difference is not significant because these shorter two bins are based on only two events, and the amount is still small.

The contribution to the total optical depth of the observed timescale distribution is given in Figure 8.14. The contributions of the short timescale events to the total optical depth are quit small.

In any case, we need more statistics to investigate in more detail about the mass function and the Galactic structure.

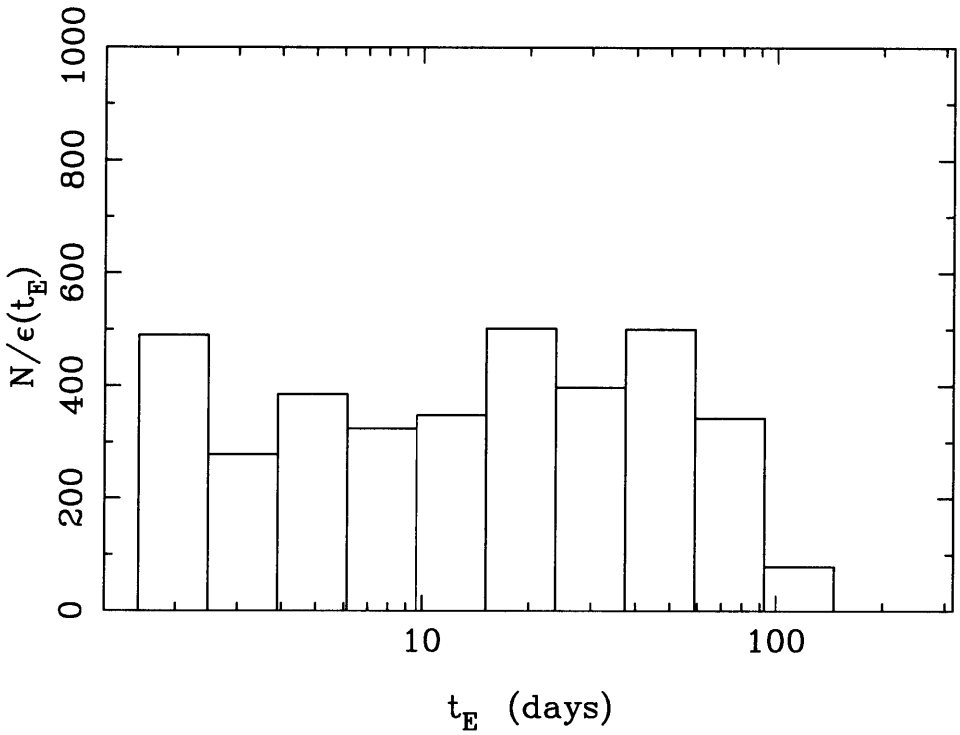

Figure 8.13: Histograms of the observed t_E distribution, corrected for the detection efficiency, i.e., the expected true t_E distribution.

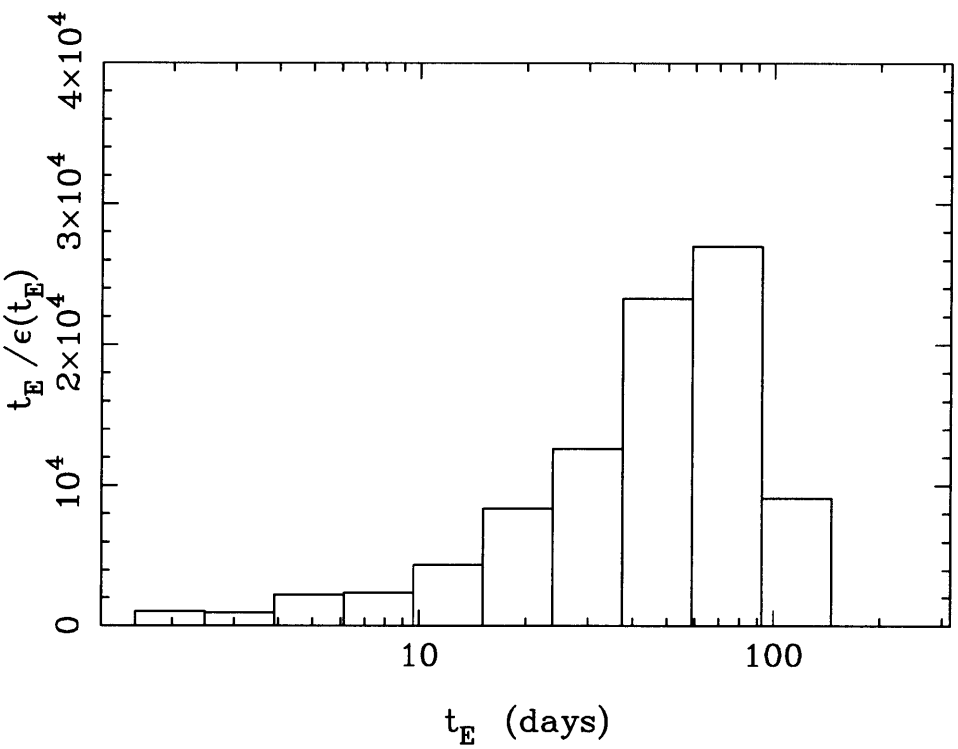

Figure 8.14: The contribution to the total optical depth ($t_E/\epsilon(t_E)$) of the event timescale t_E distribution for observed microlensing events. The contribution of the short timescale events to the optical depth is quite small.

Chapter 9

Discussion and Conclusion

We proposed two new methods to constrain the location of the lens objects of microlensing events towards the LMC. First we showed that one can distinguish whether the lens objects are in the halo or the LMC by using the Finite Source effect in EAGLE events (section 3.1). Next we showed that it is possible to distinguish whether lens objects are in the halo or the Galactic thick disk by using the Parallax effect in EAGLE events (section 3.2). These methods would be very useful to determine the nature of the MACHOs, i.e., the Galactic dark halo.

To test the possibility that such EAGLE events could actually be detected, and to study the structure of the Galactic bulge, we have analyzed the MOA GB data during the 2000 season with the DIA in off-line analysis (about on-line analysis, see Bond et al. (2001)). In this analysis we found 28 microlensing event candidates in 12 of our GB fields. The DIA is more suitable than DoPHOT analysis for our purpose, since the former method can detect the luminosity variation at any position, even where no star was previously identified.

We have done a Monte Carlo simulation to estimate the microlensing event detection efficiencies of our observations and analysis for various timescales. By using these efficiencies and unbiased timescales of our 28 detected events, we estimated the optical depth towards the Galactic bulge for events with timescales within the range $0.3 < t_E < 150$ days as

$$\tau_{0.3}^{150} = 2.62^{+0.72}_{-0.56} \times 10^{-6},$$

where the statistical uncertainty of the optical depth was estimated by Monte Carlo simulation, in which the number of events followed Poisson statistics. The timescales obtained by fitting of our detected events are not biased by blending effects due to nearby stars which appear in DoPHOT-type analysis (Udalski et al. 1994; Alcock et al. 1997a). These blending effects would make t_E shorter. In DIA all other blending components could be subtracted. The Galactic bulge microlensing optical depth, in which the disk source stars component ($f_{disk} = 23\%$) is taken into account, is given by

$$\tau_{bulge} = 3.40^{+0.94}_{-0.73} \times 10^{-6}[0.77/(1 - f_{disk})].$$

This value is consistent with the previous observations of $3.3^{-1.2}_{+1.2} \times 10^{-6}$ from 9 events by

DoPHOT analysis (Udalski et al. 1994), $3.9^{-0.9}_{+1.2} \times 10^{-6}$ from 13 events in a clump giant subsample by DoPHOT (Alcock et al. 1997a) and $3.23^{-0.50}_{+0.52} \times 10^{-6}$ from 99 events by DIA (Alcock et al. 2000a).

This observed optical depth must be regarded as a lower limit of the true value, since our observation is only sensitive to the events with $0.3 < t_E < 150$ days. Nevertheless this value is still higher than those predicted by most Galactic models whose mass and inclination of the bar are consistent with other observations. Even the smallest inclination angle and a large bar mass could not reproduce an optical depth greater than $\sim 2.5 \times 10^{-6}$ (Peale 1998).

The smallest inclination produces the largest optical depth. However the bar inclination has been reported to be in a wide range between $10° - 45°$ with various types of observations as summarized in Table 7 in Alcock et al. (2000a).

The optical depth depends on the mass of the bulge. However various observations provide conflicting values. Zhao & Mao (1996) found $M_{bulge} = (2.2 \pm 0.2) \times 10^{10} M_{\odot}$ based on COBE map data. However Dwek et al. (1995) found a mass of only $M_{bulge} = 1.3 \times 10^{10} M_{\odot}$. Holtzman (1998) found $M_{bulge} = 0.74 - 1.5 \times 10^{10} M_{\odot}$.

The bar mass has been also predicted by many authors. Han & Gould (1995b) predicted $M_{bar} = 1.6 \times 10^{10} M_{\odot}$ based on the virial theorem. However Blum (1995) predicted $M_{bar} = 2.8 \times 10^{10} M_{\odot}$ when the pattern rotation of the Galactic bar is included. Zhao & Mao (1996) said that the bar mass of at least $M_{bar} = 2.0 \times 10^{10} M_{\odot}$ is required for the COBE G1 model with $\theta = 11°$ to account for the observed amount of lensing of Alcock et al. (1997a). If a bar mass is $2.8 \times 10^{10} M_{\odot}$, the model of Zhao & Mao (1996) is consistent with Alcock et al. (1997a) at the 2 σ level. Gyuk & Crotts (1999) found $M_{bar} = 2.5 \times 10^{10} M_{\odot}$ based on a maximum-likelihood estimate of the COBE G2 model with a small inclination of $\theta = 12°$ by using the results of Alcock et al. (1997a). However, if $\theta = 20°$ is taken instead, which is consistent with most of the values observed (see Table 7 in Alcock et al. (2000a)), the bar mass rises to $\sim 3.6 \times 10^{10} M_{\odot}$ to explain the results of microlensing. Such a high mass would imply low halo MACHO fractions (Gates et al. 1996). A massive bulge puts tight constraints on the contribution of the disk to the rotation curve at small radii. A small disk, however, leaves more room for the halo. Since microlensing results towards the LMC fix the MACHO content in the halo, a massive halo implies a smaller MACHO fraction.

Such a heavy bar is required to explain our observed optical depth, however there is no evidence that the bar is massive enough to produce the observed optical depth. The uncertainties in the Galactic bar orientation, the bar mass and the stellar mass function are still large. Then there might be scope to explain this observation by other models without adding other dark components. We need more accurate measurements to constrain the bar mass used in the models. We listed the various Galactic models and the optical depth expected from each model in Table 9.1 for the comparison with our results (c.f., Alcock et al. 2000a).

We showed our observed timescale distribution which is not biased by blending. Though our statistics are smaller, this seems to be consistent with that previously presented by the

Table 9.1: Optical depth from various Galactic models.

Reference	Model characteristics	$M_{bulge,bar}$ $(10^{10}M_{\odot})$	τ (10^{-6})
Paczyński (1991)	Double-exponential disk	–	0.4-0.8
Griest (1991)	Double-exponential disk + halo	–	0.5-1.1
Evans (1994)	Symmetric bulge + massive disk	1.9	1.9
Zhao, Spergel & Rich (1995)	Bar + truncated disk	2.0	2.2 ± 0.45
Alcock et al. (1997a)	Bar + double-exponential disk	1.8	1.9
Fux (1997)	N-body model	3.0-5.0	1.8-2.0
Nikolaev & Weinberg (1997)	Non-bisymmetric disk	1.65	1.1-1.8
	Bisymmetric disk	1.65	1.1-1.6
Peale (1998)	Bar + nucleus + double-exp disk	2.2	1.54
	Bar + nucleus + double-exp disk	3.3	2.14
Sevenster et al. (1999)	Fux N-body and OH/IR stars	2.0	2.2
Gyuk & Crotts (1999)	Maximum likelihood	–	1.93 ± 0.39
Grenacher et al. (1999)	Thick + thin disk	1.8	1.9
Hafner et al. (2000)	Schwarzschild orbits	1.8	1.9

MACHO group (Alcock et al. 2000a), which supports the conclusion that microlensing towards the Galactic center can be explained by the observed normal stars, assuming they follow the Scalo (1986) mass model, without requiring a large population of brown dwarfs. The number of short events was quite small, in spite of our high detection efficiency for short timescale events down to $t_E \sim 0.3$ days. So we have confirmed that there is no significant amount of small mass lenses such as brown dwarfs towards the Galactic center.

A significant amount of long timescale ($t_E > 70$ days) events are detected, as reported previously by the MACHO group (Alcock et al. 2000a). These could not be explained by any current Galactic model (Han & Gould 1996). These might be a heavier remnant component, such as white dwarfs. So, the lens objects of microlensing towards the Galactic bulge might be a mixture of low-mass main-sequence stars and heavier remnant components. Any way, we need more statistics to investigate in more detail about the mass function and Galactic structure.

Another purpose to observe the Galactic bulge is searching for extrasolar planets. As described in section 2.5, the probability to detect extrasolar planets in the high magnification microlensing events is higher than in moderate magnification events. We showed how MOA can detect the high magnification events efficiently and fond $50 \sim 60\%$ out of all detected events have high magnification ($u_{min} < 0.1$). This fraction is much higher than 10% in DoPHOT analysis (Alcock et al. 1997a) and 30% in recent DIA analysis (Alcock et al. 2000a) by the MACHO group. This is because our sampling rate is higher ($5 \sim 6$ times/day) than that of the MACHO group. This result makes us believe that high frequency observations and the analysis with DIA, that MOA is now carrying out, can detect

high magnification microlensing events very efficiently. And this is very useful to search for extrasolar planets, even with a small telescope.

If the same observations would be taken towards the LMC, we can expect many such high magnification events as EAGLE events (see sections 3.1 and 3.2.2). In these EAGLE events the possibility to measure the proper motion v_t/x (by the finite source effect) or the reduced velocity $v_t/(1-x)$ (by the parallax effect) of lens objects is higher if the lenses are in the LMC or Galactic thick disk respectively. And then we can constrain the location of the lens objects towards the LMC, i.e., we could determine whether the lenses are MACHOs or normal stars in the LMC or the thick disk.

Accurate and frequent follow-up observations near the peak with larger telescopes are needed to measure the finite source effect and parallax effect. And follow-up observations with very high resolution telescopes such as HST or VLT are needed after the event to measure the accurate baseline of the source star, which is needed to get accurate parameters in light curve fitting. In short, a reasonable and practical observational strategy would be to observe hourly with a 1-m class telescope and perform a real-time analysis with the DIA to issue alerts to observatories in the world for follow-up observations. And after the events, the baseline should be measured by HST or VLTs. The analysis in this paper was a good demonstration to show that it is possible to find the EAGLE events with similar observations towards the LMC.

A real-time alert system with frequent sampling and the analysis by DIA, such as that recently introduced by the MOA collaboration[1] would be a powerful tool to study MACHOs and extrasolar planets.

[1] see `http://www.phys.canterbury.ac.nz/~physib/alert/alert.html`

Acknowledgment

I would like to express my deepest gratitude to Y. Muraki for his supervision, whose constructive suggestions and fruitful discussions were always of great benefit. Also I would like to thank the colleagues of his laboratory, T. Yuda, Y. Matsubara, K. Masuda, F. Abe and T. Sako, from whom I learned the bases for the scientific research. I appreciate T. Yanagisawa for teaching me the details of the CCD camera when we repaired the camera. I am very grateful to P. Yock and I. Bond for their helpful comments and discussions. I would like to thank P. Kilmartin, A. Gilmore and the other members of MOA collaboration for their support with the observations. I would like to acknowledge J. Hearnshaw for the careful reading of this thesis and for his comments. I am also grateful to M. Honma and Y. Kan-ya for their collaborations and helpful discussions. I would like to thank A. Drake for helpful comments. I also acknowledge J. Holtzman, K. Stanek, the MACHO collaboration and the OGLE collaboration for making their data publicly available. Finally I would like to thank my parents and my sister for their kind support.

References

Afonso, C. et al. 1998, A&A, 337, 17

Afonso, C. et al. 1999, A&A, 344, 63

Afonso, C. et al. 2000, ApJ, 532, 340

Alard, C. 1997, A&A, 321, 424

Alard, C. 2000, A&A, 144, 363

Alard, C. & Guibert, J. 1997, A&A, 326, 1

Alard, C. & Lupton,R.H. 1998, ApJ, 503, 325

Albrow, M. D. et al. 1999, ApJ, 512, 672

Alcock, C. et al. 1993, Nature, 365, 621

Alcock, C. et al. 1995, ApJ, 454, 125L

Alcock, C. et al. 1997a, ApJ, 479, 119

Alcock, C. et al. 1997b, ApJ, 486, 697

Alcock, C. et al. 1998, ApJ, 494, 396

Alcock, C. et al. 1999a, ApJ, 518, 44

Alcock, C. et al. 1999b, ApJ, 521, 602

Alcock, C. et al. 2000a, ApJ, 541, 734

Alcock, C. et al. 2000b, ApJ, 542, 281

Alcock, C. et al. 2001, preprint (astro-ph/0008282)

Allen, C. W. 1973, Astrophysical Quantities (London: Athlone Press)

Ansari, R., et al. 1997, A&A, 324, 843

Aubourg, E., et al. 1993, Nature, 365, 623

Aubourg, É., Palanque-Delabrouille, N., Salati, P., Spiro, M., & Taillet, R. 1999, A&A, 347, 850

Bahcall, J. N. 1986, ARA&A 24, 557

Bahcall, J. N., Flynn, C., & Gould, A. 1992, ApJ, 389, 234

Bennet, D. & Rhie, S. 1996, ApJ, 472, 660

Binney, J. & Tremaine, S. 1987, Galactic Dynamics (Princeton: NJ,Princeton University Press)

Binney, J., Gerhard, O. E. & Spergel, D. S. 1991, MNRAS, 252, 210

Blaauw, A. 1963, Basic Astr. Data

Blum, R. 1995, ApJ., 444, L89

Boden, A. et al. 1997, Venis97(ESA SP-402) ed. M. A. C. Perryman and P. L. Bernacca (Noordwijk:ESA), 789

Bolatto, A. D. & Falco, E. E. 1994, ApJ, 436, 112

Bond, I. A. et al. 2001, MNRAS, in press

Bond, I. A. et al. 2002, MNRAS, in press

Charbonneau, D. et al. 2000, ApJ, 529, L45

Charlot, S. & Silk, J. 1995, ApJ, 445, 124

Chwolson, O. 1924, Astron. Nachr., 221, 329

Crotts, A. P., 1992, ApJ, 399, L43

Crotts, A., & Tomaney, A. 1996, ApJ, 473, L87

Davis, J. & Webb, R. J. 1970, in IAU Symp. 36, On Ultraviolet Fluxes, Bolometric Corrections, and Effective Temperatures of Late B to F Stars, ed. L.Houziaux & H.E.Butler(Dordrecht:Reidel),90

Derue, F. et al. 1999, A&A, 351, 87

de Vaucouleurs, G. 1957, AJ, 62, 69

de Vaucouleurs, G. 1964. IAU Symp. 20. The Galaxy and the Magellanic Clouds, ed. F. J. Kerr & A. W. Rogers (Canberra: Australian Acad. Science, MSSSO), 195

Dwek, E. et al. 1995, ApJ, 445, 716

Dyson, F. W., Eddington, A. S., & Davidson, C. R. 1920, Mem. R. Ast. Soc., 62, 291

Einstein, A. 1936, Science, 84, 506

Evans, N. W., 1994, ApJ, 437, L31

Evans, N. W., Gyuk, G., Turner, M. S. & Binney, J. 1998, ApJ, 501, L45

Fich, M. 1989, ApJ, 342, 272

Fujita, Y., Inoue, S., Nakamura, T., Manmoto, T. & Nakamura, K.E. 1998, ApJ, 495, L85

Fux, R. 1997, A&A, 327, 983

Gates, E., Gyuk, G. & Turner, M. S. 1995, Phy. Rev. Lett., 74, 3724

Gates, E., Gyuk, G. & Turner, M. S. 1996, Phy. Rev. D, 53 4138

Gates, E., Gyuk, G., Holder, G. P., & Turner, M. S. 1998, ApJ, 500, 145

Gibson, B. K. & Mould, J. R. 1997, ApJ, 482, 98

Gilmore, G., & Reid, N. 1983, MNRAS, 202, 1025

Gilmore G. et al. 2000, GAIA: ed. J. B. Brekinridge and P. Jakobsen, Proc. SPIE, 4013

Gould, A. 1992, ApJ, 392, 442

Gould, A. 1994a, ApJ, 421, L71

Gould, A. 1994b, ApJ, 421, L75

Gould, A. 1995, ApJ, 440, 510

Gould, A. 1995, ApJ, 441, 21

Gould, A. 1996, ApJ, 470, 201

Gould, A. 1997, ApJ, 480, 188

Gould, A. 1998, ApJ, 506, 253

Gould, A. & Depoy, D. L. 1998, ApJ, 497, 62

Gould, A., Miralda-Escude, J. & Bahcall, J. N. 1994, ApJ, 423, 105

Gould, A. & Loeb, A. 1992, ApJ, 396, 104

Gould, A., Popowski, P. & Terndrup, D. M. 1998, ApJ, 492, 778

Grenacher, L., et al. 1999, A&A, 351, 775

Griest, K. 1991, ApJ, 366, 412

Griest, K. & Safizadeh, N. 1998, ApJ, 500, 37

Griest, K. et al. 1991 ApJ, 372, L79

Gyuk, G. & Crotts, A. 1999, preprint(astro-ph/9904314)

Gyuk, G., Dalal, N. & Griest, K. 2000, ApJ, 535, 90

Hafner, R. M., et al., 2000, MNRAS, 314, 433

Han, C. & Gould, A. 1996, ApJ, 467, 540

Han, C. 1997, ApJ, 490, 51

Han 1999, preprint (astro-ph/9910198)

Han, C. 2000, MNRAS, 312, 807

Han, C. & Gould, A. 1995, ApJ, 447, 53

Han, C. & Gould, A. 1995, ApJ, 449, 521

Hansen, B. M. S. 1998, nature, 394, 860

Holz, D. E. & Wald,R.M. 1996, ApJ, 471, 64

Holtzman, J. A. 1997, AJ, 113, 656

Holtzman, J. A. 1998, ApJ, 115, 1946

Honma, M. 1999, ApJ, 511, L29

Honma, M. & Kan-ya, Y. 1998, ApJ, 503, L139

Honma, M. & Sofue, Y. 1996, PASJ, 48, L103

Ibata, R., Irwin, M., Bienaymé, O., Schlz, R., & Guibert, J. 2000, ApJ, 532, L41

Ioka, K., Tanaka, T. & Nakamura, T. 2000, ApJ, 528, 51

Jedamzik, K. 1997, Phys. Rev. D, 55, 5871

Johnson, H. L. 1964, Bol. Inst. Tonantzintla, 3, 305

Kaswasaki, M. & Yanagida, T. 1999, Phys. Rev. D, 59, 043512

Kippenhahn, P. & Weigert, A. 1990, Stellar Structure and Evolution (Berlin:Springer)

Kiraga, M., & Paczyński, B. 1994, ApJ, 430, L101

Kiraga, M., Paczyński, B. & Stanek, K. Z., 1997, ApJ, 485, 611

Kuijken K. & Gilmore G. 1989, MNRAS 239, 605

Lebach, D. E., Shapiro, I. I. & Ratner, M. 1995, Phys. Rev. D, 75, 1439

Liebes, S. 1964, Phys. Rev., 133, 835

Mao, S. & Paczyński, B. 1991, ApJ, 374, L37

Mao, S. & Paczyński, B. 1996, ApJ, 473, 57

Mather, J. C. et al. 1997, ASP Conf. Ser.119,245

Mayor, M. & Queloz, D. 1995, Nature, 378, 355

Mera, D., Chabrier, G. & Schaeffer, R. 1998, A&A, 330, 937

Miyamoto, M., & Yoshii Y. 1995, AJ, 110, 1427

Miyamoto, M. & Zhu, Z. 1998, ApJ, 506, 253

Nakamura, T., Kan-ya, Y., & Nishi, R. 1998, ApJ, 473, 99

Nakamura, T. & Nishi, R. 1998, Progress of Theoretical Physics, vol.99, 963

Nemiroff, R. J. & Wickramasinghe, W. A. D. T. 1994, ApJ, 424, 21

Ng, Y. K., et al. 1996, A&A, 310, 771

Nikolaev, S. & Weinberg, M. D., 1997, ApJ, 487, 885

Oort, J. H. 1960, Bull. Astron. Inst. Neth. 15, 45

Paczyński, B. 1986, ApJ, 304,1

Paczyński, B. 1991, ApJ., 371, L63

Paczyński, B. et al. 1994, ApJ., 435, L113

Paczyński, B. et al., 1999, Acta. Astron.,49, 319

Peale, S. J. 1998, ApJ, 509, 177

Peng, E. W. 1997, ApJ, 475, 43

Pennycook, G. 1996, M.Sc thesis, University of Auckland

Perryman, M. A. 2000, Rep. Prog. Phys., 63, 1209

Phillips, A. C. & Davis, L. E. 1995, ASP conf. series, 77, Astronomical Data Analysis and Software System IV, ed. R. A. Shaw et al., 297

Refsdal, S. 1964, MNRAS, 128, 295

Refsdal, S. 1966, MNRAS, 134, 315

Reiss, D. J. et al., 1998, AJ, 115, 26

Rhie, S. 2000, ApJ, 533, 378

Rubin, V. et al. 1980, ApJ, 238, 471

Rubin, V. et al. 1982, ApJ, 261, 439

Rubin, V. et al. 1985, ApJ, 289, 81

Ruelas-Mayorga, A. B. & Noriega-Mendoza, H. 1995, Rev. Mex. Astron. Astrofis., 31, 115

Sahu, K. 1994, PASP 106, 942

Sahu, K., et al., 2001, Nature, 411, 1022

Scalo, J. M. 1986, Fundam. Cosmic Phys., 11, 1

Schechter, L., Mateo, M., & Saha, A., 1993, PASP, 105, 1342S

Schild, R. et al. 1971, ApJ, 166, 95

Schneider, P. & Weiss A. 1986, A&A, 164, 237

Sekiguchi, M. 1998, Experimental Astronomy, 8, 51

Sevenster, M. J. et al. 1999, MNRAS, 307, 584

Soldner, J. 1805, Berliner Astron. Jahrb. 1804, 105, 161

Soszyński, I. et al. 2001, preprint (astro-ph/0012144)

Stanek, K. Z. 1996, ApJ, 460, 37L

Sumi, T. & Honma, M. 2000, ApJ, 538, 657

Tomany, A. B. & Crotts, A. P., 1996, AJ, 112, 2872

Udalski, A., et al. 1993, Acta. Astron.,43, 289

Udalski et al., 1994, Acta Astronomica, 44, 165

Uehara, H. & Inutsuka, S. 2000, ApJ, 531, L91

Ueruc, F., et al. 1999, A&A, 351, 87

Uglesich, R., et al., 1999, AASM, 194, 9904

Vallee, J. P. 1995, AASM, 454, 119

Walsh, D., Carswell, R. F., & Weyman, R. J. 1979, Nature, 279, 381

Wambsganss, J. 1997, MNRAS, 284, 172

Wang, Y. & Turner, E. L. 1996, ApJ, 464, 114

Westerlund, B. 1991, IAU Symp. 148, The Magellanic Clouds, ed. R.Haynes and D.Milne (Dordrecht, Kluwer),15

Westerlund, B. 1997, The Magellanic Clouds (Cambridge: Cambridge Univ. Press)

Williams, A. 1996, PhD thesis, University of Western Australia

Witt, H. 1995, ApJ, 449, 42

Witt, H. J. & Mao, S. 1994, ApJ, 430, 505

Wolszczan, A., & Frail, D. A. 1992, Nature, 355, 145

Woźniak, P.R. 2000, preprint (astro-ph/0012143)

Woźniak, P. R. & Paczyński, B. 1997, ApJ, 487, 55

Woźniak, P. R. & Stanek, K. Z. 1996, ApJ, 464, 233

Yanagisawa, T. 2000, Experimental Astronomy, 10, 519

Yokoyama, J. 1997, A&A, 318, 673

Zaritsky, D. & Lin, D. N. C. 1997, AJ, 114, 2545

Zhao, H. S. 1998, MNRAS, 294, 139

Zhao, H. & Mao, S. 1996, MNRAS, 283, 1197

Zhao, H., Spergel, D. N. & Rich, R. 1995, ApJ, 440, L13

Zwicky, F. 1937, Phys. Rev., 51, 290

Appendix A

Photon-statistic error estimates in microlensing light curve fitting and the criterion for the detection of the parallax effect

The detectable number of parallax-measurable microlensing events depends on the photometric error which affects the measurement of t_0 and β. If we used the real-time alert system with DIA which has been adopted, for example, by the MOA collaboration, the photometric accuracy would be able to reach very close to the photon shot noise expectation (Alard & Lupton 1998; Alard 2000; Alcock et al. 1999b, 2000a; Woźniak 2000; Bond et al. 2001). Here we show the criterion necessary to determine $\tilde{v}$ within assumed relative error tolerance $\varepsilon_{\tilde{v}}$ from the measurement of t_0 and β for a microlensing event with given magnitude of a source star, V, a given set of the parameters of the lens object, t_E and $\tilde{v}$ ($\tilde{R}_{\rm E} = \tilde{v}t_E$), and assumed observational parameters, D, $V_{\rm th}$, and $V_{\rm obs}$. Here we assume that the photometric errors at both observational sites are equal.

We calculate the expected uncertainty $\Delta\tilde{v}$ in the measurement of $\tilde{v}$ by estimating Δt_0 and $\Delta\beta$ which are the errors in t_0 and β, respectively. The general discussion to estimate the error or the variance of a set of parameters a_i in fitting a distribution $F(t, a_i)$ is presented by, e.g., Gould (1995a) and Gould (1998) using the minimum variance bound given from a well-known theorem in statistics. The covariance matrix c_{ij} with respect to a_i for a series of measurements $F(t_k)$ at time t_k with error σ_k is given by

$$c_{ij} = b_{ij}^{-1}, \quad b_{ij} = \sum_k \Delta F(t_k)^{-2} \frac{\partial F(t_k)}{\partial a_i} \frac{\partial F(t_k)}{\partial a_j}. \tag{A.1}$$

The variance of a_i is just the diagonal elements c_{ii}.

We take $F(t)$ as the number of the detected photo-electrons at time t, which is the signal from the source star. During a short time interval T, we get $F(t) = (f_0(V)A(t;\beta,t_0) + f_b)T$ photo-electrons, where f_0 denotes the average photo-electron flux from the unamplified source star and $f_b = f_{blend} + f_{sky}$ denotes the background flux in the PSF aperture which

consists of the flux from the unlensed blending stars (f_{blend}) and the night sky (f_{sky}). Most of microlensed source stars are blotted out by the unlensed background stars, because microlensing surveys should be carried out towards very dense star fields. $A(t;\beta,t_0)$ is the amplification produced by microlensing given by equations (2.12) and (2.13). Because $\Delta F(t) = \sqrt{F(t)}$, using equation (A.1) and taking the limit $T \to 0$, the uncertainty in t_0 and β is, to order of magnitude, given by

$$(\Delta t_0)^{-2} \simeq \sum_k \Delta F(t_k)^{-2} \left[\frac{\partial F(t_k)}{\partial t_0}\right]^2 \tag{A.2}$$
$$\to f_0(V)^2 \int_{t_{\rm begin}}^{t_{\rm end}} \frac{1}{f_0(V)A + f_b} \left[\frac{\partial A}{\partial t_0}\right]^2 dt,$$

$$(\Delta \beta)^{-2} \simeq \sum_k \Delta F(t_k)^{-2} \left[\frac{\partial F(t_k)}{\partial \beta}\right]^2 \tag{A.3}$$
$$\to f_0(V)^2 \int_{t_{\rm begin}}^{t_{\rm end}} \frac{1}{f_0(V)A + f_b} \left[\frac{\partial A}{\partial \beta}\right]^2 dt,$$

where we assumed that the observation of the light curve begins at the time $t_{\rm begin}$ and ends at $t_{\rm end}$. Actually the parameter β correlates with f_0. Assuming the f_0 could be measured accurately by follow-up observations, this formula is valid. From these we obtain the formula for the expected error $\Delta\tilde{v}$ as follows:

$$\Delta\tilde{v} \simeq \left\{ \left[\frac{\partial \tilde{v}}{\partial(\delta t_0)} \Delta(\delta t_0)\right]^2 + \left[\frac{\partial \tilde{v}}{\partial(\delta\beta)} \Delta(\delta\beta)\right]^2 \right\}^{\frac{1}{2}}, \tag{A.4}$$

where $\Delta(\delta t_0) = \sqrt{2}\Delta t_0$ and $\Delta(\delta\beta) = \sqrt{2}\Delta\beta$ are the expected errors of δt_0 and $\delta\beta$. We apply this formula to a normal and an EAGLE event.

For the beginning of an EAGLE event, we assume that we start observing the event at time $t_{\rm begin} = t_0 - t_{\rm th}$, where $t_{\rm th}$ is the time interval between the time when the source with magnitude V is just magnified to the EAGLE detection threshold $V_{\rm th}$. $t_{\rm th}$ is expressed as

$$t_{\rm th} = t_{\rm mag}(V, t_E, \beta; V_{\rm th}) \equiv \frac{\sqrt{(u_{\rm T}(V)R_{\rm E})^2 - (\beta R_{\rm E})^2}}{v_{\rm t}} \tag{A.5}$$
$$= t_E \beta \sqrt{\left(\frac{u_{\rm T}(V)}{\beta}\right)^2 - 1},$$

where $u_{\rm T}(V)$ is given in equation (2.27).

We should take $t_{\rm end}$ at the time when the magnitude of the amplified source star declined to the observation limiting magnitude of the alert telescope $V_{\rm obs}$ and set $t_{\rm end} = t_0 + t_{\rm obs}$, where $t_{\rm obs}$ is the time interval between t_0 and the time when the source magnitude reached $V_{\rm obs}$. Using $t_{\rm mag}$ defined in equation (A.6), $t_{\rm obs} = t_{\rm mag}(V, t_E, \beta; V_{\rm obs})$.

Transforming the argument t to ϕ as $\tan\phi = (t - t_0)/(t_E\beta)$, equations (A.2) and (A.3) can be rewritten as

$$(\Delta t_0)^{-2} = f_0(V)^2 \int_{-\phi_{\rm th}}^{\phi_{\rm obs}} \frac{\sin^2\phi\cos^2\phi}{t_E\beta^3(f_0(V)\frac{\cos\phi}{\beta} + f_b)} d\phi \tag{A.6}$$

$$
\begin{aligned}
&= \frac{f_0(V)}{t_E\beta^2} g_1(\phi_{\rm th}, \phi_{\rm obs}), \\
(\Delta\beta)^{-2} &= f_0(V)^2 \int_{-\phi_{\rm th}}^{\phi_{\rm obs}} \frac{t_E \cos^4\phi}{\beta^3 (f_0(V)\frac{\cos\phi}{\beta} + f_b)} d\phi \qquad \text{(A.7)} \\
&= \frac{f_0(V) t_E}{\beta^2} g_2(\phi_{\rm th}, \phi_{\rm obs}),
\end{aligned}
$$

where

$$
g_1(\phi_{\rm th}, \phi_{\rm obs}) \equiv \int_{-\phi_{\rm th}}^{\phi_{\rm obs}} \frac{\sin^2\phi\cos^2\phi}{\cos\phi + \frac{f_b}{f_0(V)} \frac{u_T}{(\tan^2\phi_{th}+1)^{\frac{1}{2}}}} d\phi, \qquad \text{(A.8)}
$$

$$
g_2(\phi_{\rm th}, \phi_{\rm obs}) \equiv \int_{-\phi_{\rm th}}^{\phi_{\rm obs}} \frac{\cos^4\phi}{\cos\phi + \frac{f_b}{f_0(V)} \frac{u_T}{(\tan^2\phi_{th}+1)^{\frac{1}{2}}}} d\phi, \qquad \text{(A.9)}
$$

$$
\tan\phi_{\rm th}(V,\beta) \equiv \frac{t_{\rm th}}{t_E\beta}, \qquad \text{(A.10)}
$$

$$
\tan\phi_{\rm obs}(V,\beta) \equiv \frac{t_{\rm obs}}{t_E\beta}. \qquad \text{(A.11)}
$$

From equations (3.31)–(3.33) and (A.4)–(A.11) we obtain the the relative error of $\tilde{v}$ as

$$
\frac{\Delta\tilde{v}}{\tilde{v}} \simeq \frac{\tilde{v} u_{\rm T}(V)}{D} \sqrt{\frac{t_E}{f_0(V)}} S_\theta(\phi_{\rm th}, \phi_{\rm obs}), \qquad \text{(A.12)}
$$

where $S_\theta(\phi_{\rm th}, \phi_{\rm obs})$ is written as

$$
S_\theta(\phi_{\rm th}, \phi_{\rm obs}) = \left\{ \frac{2}{1+\tan^2\phi_{\rm th}} \left[\frac{\cos^2\theta}{g_1(\phi_{\rm th}, \phi_{\rm obs})} + \frac{\sin^2\theta}{g_2(\phi_{\rm th}, \phi_{\rm obs})} \right] \right\}^{\frac{1}{2}}. \qquad \text{(A.13)}
$$

θ can be considered to be a random variable so we take the mean value; $S_\theta(\phi_{\rm th}, \phi_{\rm obs})$ in equation (A.12) is to be replaced by $S(\phi_{\rm th}, \phi_{\rm obs})$. Fortunately, $S(\phi_{\rm th}, \phi_{\rm obs})$ is independent of source brightness, using the relation $\beta = u_T/(\tan^2\phi_{th}+1)^{1/2}$ and $f_0(V)/u_T = f_0(V = 20) = const.$ and only depends on $\phi_{\rm th}$ and $\phi_{\rm obs}$. This is very convenient for the following calculation. We obtain the necessary criterion to detect an EAGLE event with parallax effect as $\Delta\tilde{v}/\tilde{v} < \varepsilon_{\tilde{v}}$, i.e., from equations (2.8), (3.29), and (A.12)

$$
\begin{aligned}
& u_{\rm T}(V) S(\phi_{\rm th}, \phi_{\rm obs}) \sqrt{\frac{\tilde{v}}{f_0(V)}} \left(\frac{Mx}{1-x}\right)^{\frac{1}{4}} \\
&= u_{\rm T}(V) S(\phi_{\rm th}, \phi_{\rm obs}) \sqrt{\frac{v_{\rm t}}{f_0(V)}} \left(\frac{Mx}{(1-x)^3}\right)^{\frac{1}{4}} \qquad \text{(A.14)} \\
&< D\varepsilon_{\tilde{v}} \left(\frac{c^2}{4GD_{\rm S}}\right)^{\frac{1}{4}} = \text{const.}
\end{aligned}
$$

From equation (A.14) we see that an EAGLE event tends to be detected with parallax effect when the source star is bright (large f_0), when the source star is largely amplified

(small u_T), when the tangential velocity is slow (small v_t), or when the lens object is near and light (small x and M), althogh the dependence on x and M is not so strong. For the function S, we show $S(\phi_{th}, \phi_{obs}(\phi_{th}))$ as a function of ϕ_{th} in Figure A.1 (solid line), under the assumption that $V_{obs} = V_{th} + 1$ i.e. the relationship $\tan\phi_{obs} = \sqrt{2.5^2(\tan^2\phi_{th} + 1) - 1}$ holds. In this figure we also plot the curve for $S(\phi_{th}, \phi_{th})$ and $S(\phi_{obs}(\phi_{th}), \phi_{obs}(\phi_{th}))$ for comparison. From Figure A.1 we see that S does not change its order of magnitude so strongly as long as the observation is continued to $V > V_{th}$ in the declining phase of the amplification. However, if the observation ends too early ($V \simeq V_{th}$), shown in the broken line of Figure A.1, S diverges and the parallax effect is hard to detect for the events with $\phi_{th} \ll 1$. That $\phi_{th} \ll 1$ means that $u_T \simeq \beta$ (equations (A.6) and (A.10)) i.e. the peak magnitude of the event is close to the EAGLE detection threshold V_{th}. Since whether we can detect a parallax effect in this type of events affects the relative parallax-measurable event rate discussed in the section 3.2.3, the follow-up chasing of the event dimming below V_{th} with larger telescopes than the alert telescope is of great importance.

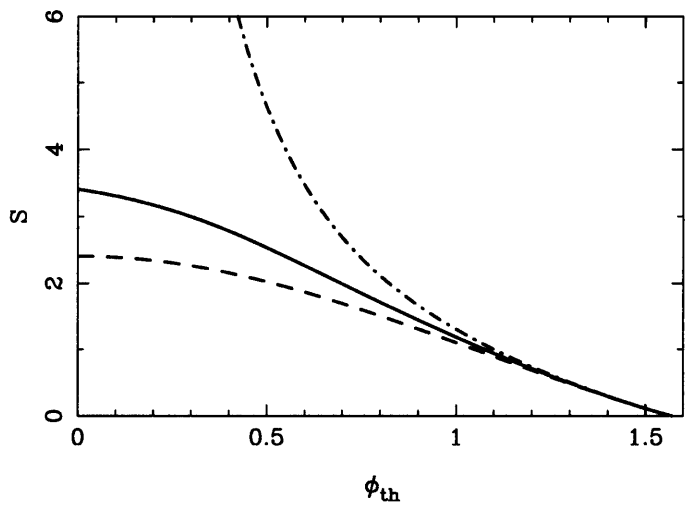

Figure A.1: The function S, which is S_θ in equation (A.13) averaged over θ, under the assumption $V_{obs} = V_{th}+1$. The solid, dot-dashed and dashed lines indicate $S(\phi_{th}, \phi_{obs}(\phi_{th}))$, $S(\phi_{th}, \phi_{th})$ and $S(\phi_{obs}(\phi_{th}), \phi_{obs}(\phi_{th}))$, respectively.

For EAGLE events we can rewrite the criterion (A.14) more conveniently. If we specify the magnitude of the source star, V ($> V_{obs}$), lens geometry, M and x, lens transverse velocity, v_t, and observational parameters with the assumption $V_{obs} = V_{th} + 1$, then $t_E = R_E(M, x)/v_t(z(x))$ is determined and we can solve the detection criterion (A.14) with respect to ϕ_{th}. If the solution $\phi_{th,crit}(V, M, x, v_t)$ exists, it is the unique solution because of the monotonity of S seen in Figure A.1. The existence of the solution implies that we can observe microlensing events with a parallax effect when the impact parameter β is less than the critical impact parameter. That is,

$$\beta < \beta_{crit}(V, M, x, v_t) \equiv \frac{u_T(V)}{\sqrt{\tan^2\phi_{th,crit}(V, M, x, v_t) + 1}}, \tag{A.15}$$

from equations (A.6) and (A.10). This is another expression for the detection criterion (A.14).

For a normal event one can take $t_{\rm begin} = t_{\rm end} \to \infty$ (i.e. $\phi_{th} = \phi_{obs} \to \pi/2$), since we can observe the event continually during the period in which the source is magnified. So if we specify lensing parameters $(V, M, x, v_{\rm t})$, we can derive $\beta_{\rm crit}$ from an equation corresponding to equation (A.15) with $\phi_{th} = \phi_{obs} \to \pi/2$. However we applied equation (A.14) with the relation of equation (A.15) for normal events to ease the following calculation, because $S(\phi_{\rm th}, \phi_{\rm obs}(\phi_{\rm th}))$ is independent of other parameters except ϕ_{th}. Using this formula, the duration of the observation is related to equation (A.6) instead of infinity. However, this observing period is long enough, because the width of the integrand of equations (A.2) and (A.3) is of order $\hat{t}/A(t_0)$, and $\beta_{\rm crit}$ is sufficiently small for normal events.

Actually, we confirmed that difference of $\beta_{\rm crit}$ from these formulas is less than 0.2% for $V < 21$. The equations (A.6) and (A.7) which are valid only for high magnification events are applicable because we are concerned with only high magnification events, even for normal events.

Appendix B

Model and Assumptions for Parallax

B.1 Model Kinematics

For disk events the typical transverse velocity of a lens object v_t is estimated as follows. First we assume that the thin and thick disks have the same rotation velocity and the relative velocity between the mean flow of the lens objects and the local standard of rest (LSR) is zero. In fact the effect of the drift velocity of the thick disk relative to the thin disk due to the large velocity dispersion of the thick disk is negligible compared to other effects. v_t is the composition of the tangential component of the mean velocity of the Earth relative to the LSR $v_\oplus$ and the velocity dispersion of the disk σ, which is assumed to be isotropic for both disks, as

$$v_t^2(z) = 2\sigma^2(z) + v_\oplus^2. \tag{B.1}$$

We take $v_\oplus = 30$ km s^{-1}, which includes the orbital velocity of Earth around the Sun of 30 km s^{-1} and a velocity of the Sun relative to LSR of 20km s^{-1} (Miyamoto & Zhu 1998). $\sigma^2(z)$ and v_t^2 are assumed to be a function of z only (see the discussion on equation (3.28)). The density profile of the disk is same as in section 3.2.1, i.e., the exponential disk density distributions in equation (3.28) for thin ($h_{\rm thin} = 350$ pc) and thick ($h_{\rm thick} = 1400$ pc) disks with variable values of the local disk column density as $\Sigma_{\rm thin}(\Sigma_{\rm thick}) = 30(70), 50(50), 70(30) M_\odot {\rm pc}^{-2}$. Solving the Poisson equation for the density profile composed of the thin and the thick disks the $\sigma^2(z)$ is obtained from the z-component of the Jeans equation (e.g. Binney & Tremaine 1987) as

$$\sigma^2(z) = \frac{\pi G}{2} \frac{\left[\Sigma_{\rm thin} \exp\left(-\frac{z}{h_{\rm thin}}\right) + \Sigma_{\rm thick} \exp\left(-\frac{z}{h_{\rm thick}}\right)\right]^2}{\rho_{\rm thin}(z) + \rho_{\rm thick}(z)}. \tag{B.2}$$

For halo events we adopt the same model as section 3.2.1 and we assume $v_t = 190$ km s^{-1} or 220 km s^{-1}. $v_t = 190$ km s^{-1} is more plausible because of the slight contribution from the disk gravity to the rotation curve, which is assumed to be flat and to be with $v_{\rm rot} = 220$ km s^{-1}.

B.2 Assumptions about Observational Parameters

We assume that two 2.5-m class follow-up telescopes are used on different continents. So $D = 6000$ km is a reasonable value. We also assume $V_{\rm th} = 20$ and $V_{\rm obs} = 21$, which are realistic for a 1-m class alert telescope. As noted in section 2.4, the events with the source star having $V < 21$ are normal microlensing events, while ones with $V > 21$ are EAGLE events. The photo-electron flux $f_0(V = 20) \simeq 500$ electrons s^{-1} when we use two thin CCD cameras with a dichroic mirror to split the light to two band filters near the V band with not so broad a bandwidth (~ 100 nm). The very broad-band filter is not advisable because that might not be able to eliminate the effect of differential refraction or differential extinction of the atmosphere (Gould 1998). We adopted the background flux $f_b = 600$ electrons s^{-1} corresponding to $V = 19.8$ mag, which is estimated as follows: The mean V-band surface brightness of the inner 10 deg^2 of the LMC is $V = 22.01$ mag/arcsec^2, and the sky value is $V = 21.6$ mag/arcsec^2 (de Vaucouleurs 1957). We assume the aperture of the PSF is π arcsec^2 at a good site, which corresponds to $\sim 1''$ seeing. The total brightness in the aperture is 19.8 mag. We adopted this value for f_b. The relative error tolerance $\varepsilon_{\tilde{v}}$ is assumed to be 50%. For the source stars, we assume the same luminosity function as in section 3.2.1.

To make the estimation realistic, we reduced the accuracy of the measurements discussed in Appendix A. Assuming that we observe 8 hours a day, we reduced $f_0(V)$ by a factor of 3. We applied the photometric error as 17% larger than the photon noise, which is estimated for the DIA method (Woźniak 2000). To check the validity of equation (A.12), Holz & Wald (1996) have done a Monte Carlo simulation and found that the agreement between the numerical and analytic estimates was fairly good within a factor of two in all cases. So we doubled the relative error in the right-hand side of equation (A.12).